



**HAL**  
open science

# Application of ultrafast optical interferometry for opto-acousto-optical depth-profiling of materials

Artem Husiev

► **To cite this version:**

Artem Husiev. Application of ultrafast optical interferometry for opto-acousto-optical depth-profiling of materials. Acoustics [physics.class-ph]. Le Mans Université, 2022. English. NNT : 2022LEMA1040 . tel-04060998

**HAL Id: tel-04060998**

**<https://theses.hal.science/tel-04060998>**

Submitted on 6 Apr 2023

**HAL** is a multi-disciplinary open access archive for the deposit and dissemination of scientific research documents, whether they are published or not. The documents may come from teaching and research institutions in France or abroad, or from public or private research centers.

L'archive ouverte pluridisciplinaire **HAL**, est destinée au dépôt et à la diffusion de documents scientifiques de niveau recherche, publiés ou non, émanant des établissements d'enseignement et de recherche français ou étrangers, des laboratoires publics ou privés.

# THÈSE DE DOCTORAT DE

LE MANS UNIVERSITÉ

ÉCOLE DOCTORALE N° 602  
*Sciences pour l'Ingénieur*  
Spécialité : *Acoustique*

Par

**Artem HUSIEV**

**Application of ultrafast optical interferometry for opto-acousto-optical depth-profiling of materials**

Thèse présentée et soutenue à Le Mans Université, le 14 décembre 2022

Unité de recherche : Laboratoire d'Acoustique de l'Université du Mans (LAUM), UMR CNRS 6613

Thèse N° : 2022LEMA1040

## Rapporteurs avant soutenance :

Arnaud DEVOS Directeur de recherche CNRS, Institut d'Electronique, de Microélectronique et de Nanotechnologie  
David H. HURLEY Directeur de recherche, Idaho National Laboratory

## Composition du Jury :

Examineurs :	Bertrand AUDOIN	Professeur des Universités, Université de Bordeaux
	Agnès HUYNH	Maître de Conférences, Sorbonne Université
Dir. de thèse :	Vitali GOUSSEV (Vitaliy E. GUSEV)	Professeur des Universités, Le Mans Université
Co-dir. de thèse :	Samuel RAETZ	Maître de Conférences, Le Mans Université
	Nikolay CHIGAREV	Ingénieur de Recherche, Le Mans Université



*« In science, every failure advances the boundary of knowledge, as well as every success. »*

Alexander Graham Bell



# TABLE OF CONTENTS

---

<b>General introduction</b>	<b>1</b>
<b>1 Background</b>	<b>7</b>
1.1 History, basic principles and first applications of the optoacoustic and acousto-optic effects . . . . .	8
1.1.1 On the discovery, study and first applications of the optoacoustic and acousto-optic effects . . . . .	9
1.1.2 Optical generation and detection of the acoustic waves . . . . .	14
1.1.3 First experiments in laser ultrasonics . . . . .	17
1.2 Picosecond laser ultrasonics . . . . .	21
1.2.1 Genesis of picosecond laser ultrasonics . . . . .	21
1.2.2 Application examples of picosecond laser ultrasonics . . . . .	23
1.3 Subsurface imaging and depth profiling by Brillouin scattering . . . . .	26
1.3.1 Classical methods of subsurface imaging at the micro- and nanoscale	26
1.3.2 Depth profiling by Brillouin scattering . . . . .	27
1.4 Optical interferometry . . . . .	33
1.4.1 Inadequacy of several interferometric schemes to our objective . . .	35
1.4.2 Sagnac interferometer in picosecond laser ultrasonics . . . . .	36
1.4.3 On the interference of orthogonally polarized light waves . . . . .	39
1.5 Chapter summary and thesis outlook . . . . .	40
<b>2 Easily angle-adjustable fiber ultrafast Sagnac scheme for ultrafast optical interferometry</b>	<b>43</b>
2.1 Presentation of the chosen configuration of the experimental setup . . . . .	44
2.2 Mechanical solution for the probe incidence angle variation . . . . .	49
2.3 System for the pump beam on-sample positioning . . . . .	50
2.4 Installation, alignment and fine adjustments . . . . .	51
2.4.1 Optical fiber alignment . . . . .	54
2.4.2 Polarization optics installation . . . . .	57
2.5 Detection . . . . .	59
2.6 First test of the experimental setup in the transient reflectivity configuration	60
2.7 Chapter summary . . . . .	62

<b>3</b>	<b>Ultrafast interferometry for depth-profiling by TDBS</b>	<b>63</b>
3.1	Theoretical expectations on axial resolution . . . . .	64
3.2	Choice of the incidence angle range for good sensitivity . . . . .	65
3.3	Light intensity reaching the photodetector in ultrafast optical interferometry	66
3.4	Illustration of the theoretical expectations and of few factors influencing the actual performances . . . . .	70
3.4.1	Ideal cases . . . . .	71
3.4.2	Effect of misbalancing the reference and probing electric field am- plitudes . . . . .	72
3.4.3	Effect of thermal background . . . . .	73
3.4.4	Effect of sample properties variations between both measurements .	74
3.4.5	Effect of measurement noises . . . . .	75
3.4.6	Effect of the deviation from the expected $0^\circ$ and $90^\circ$ orientations of QWP . . . . .	78
3.5	Summary of the listed factors influencing the results and few solutions to limit them . . . . .	80
3.6	Signal processing method to reduce the influence of other-than-acoustic contributions . . . . .	83
3.7	TDBS measurements on a homogeneous GaAs wafer via ultrafast optical interferometry . . . . .	86
3.7.1	Configuration of the experimental setup and presentation of the sample . . . . .	86
3.7.2	Results . . . . .	88
3.7.3	Discussion . . . . .	91
3.8	Chapter summary . . . . .	93
<b>4</b>	<b>Future plans and perspectives applications</b>	<b>95</b>
4.1	Possible improvements and modifications of the experimental setup . . . .	95
4.1.1	Equipment replacement for the better precision and the space min- imization . . . . .	95
4.1.2	Optimization and automatization of the setup . . . . .	96
4.1.3	Use of the setup at different wavelengths . . . . .	97
4.1.4	Possibility to perform experiments with small incidence angles of the probe laser . . . . .	97
4.1.5	Optical differentiation . . . . .	98
4.2	Two other possible configurations of the experimental setup . . . . .	99
4.3	Surface acoustic wave detection . . . . .	100
4.4	Chapter summary . . . . .	102
	<b>General conclusion</b>	<b>103</b>

<b>Appendices</b>	<b>107</b>
<b>A Brillouin frequency</b>	<b>108</b>
A.1 Momentum conservation . . . . .	108
A.2 Bragg's condition . . . . .	110
<b>B Jones calculus of the light intensity reaching the photodetector</b>	<b>112</b>
<b>C Light insertion into the single-mode polarization-maintaining optical fiber</b>	<b>118</b>
<b>D Depth-profiling with two incidence angles</b>	<b>121</b>
<b>Bibliography</b>	<b>123</b>
<b>Bibliography</b>	<b>123</b>



# GENERAL INTRODUCTION

---

The importance of the non-destructive evaluation (NDE) is hard to overestimate. These are diverse methods, based on acoustics, thermal emission, electromagnetism, and various methods for specific applications, such as used in industry bubble leak testing, well known by the cyclist who can easily find the hole in a punctured wheel by immersing a pre-inflated wheel in a container filled with water. These methods allow the control of various products and processes at different scales and during different stages of the production process without causing damage. The outcome will result in superior quality, higher safety, better economy. Ultrasonic testing is one of the well-established methods of NDE that use acoustic waves to extract information about various on-top or in-depth defects. Higher acoustic frequencies allow to localize and identify smaller flaws. Regular contact transducers for the sound generation have macroscopic dimensions, which means that these are unable to work with microscopic samples, as well study of complex surfaces may be unachievable. The introduction of the sound generation methods based on the photoacoustic effect made it possible to overcome these limitations by introducing a pulsed laser, which can be directed on the desired surface from any distance and focused in a spot of micrometer dimensions. If a laser pulse falls on an absorbing material, locally introduced heat will result in the almost instantaneous temperature rise, which in turn will result in thermoelastic stresses initiating material expansion (or contraction). This process will launch an acoustic wave. Sound propagation in some medium is simply a local perturbation of material properties. Hence, if the light wave, which propagates through the same volume, encounters the acoustic wave, it will be partially reflected at this local perturbation of material properties. The acousto-optic effect is a generalized name for processes when light is affected by an acoustic wave. It means that the laser beam potentially could be used for the detection of acoustic waves. The technique with coherent electromagnetic radiation emitted by the laser used for the generation and detection of acoustic waves is called laser ultrasonics.

For the sound generation the parameters of the laser radiation and the physical properties of the material play an important role leading to various possible mechanisms of the sound generation: the electrostriction (contraction or expansion of a dielectric under the influence of an electric field, scaling proportionally to the square of the electric field), the deformation potential mechanism (externally induced modification of the electronic distribution resulting in the subsequent material deformation), the inverse piezoelectric effect (contraction or expansion of certain materials under the influence of the applied

electric field, scaling linearly with the electric field), and the thermoelasticity [1]. The latter can be characterized at the low laser power as a sound excitation regime that does not induce any damage relying on the thermal expansion of the sample with the subsequent heat dissipation and return to the initial state (thermoelasticity regime). The high-power laser applied to the material will turn into plasma some local volume (ablation regime). Despite this, the ablation regime is very valuable for the sound generation and detection of macroscale objects, in a hostile environment or in other cases where strong signals are necessary despite slight damage. These regimes have found multiple applications and proved their capability to conduct experiments in all states of matter. The thermoelastic sound generation regime, used in combination with one of the various optical detection methods of the acoustic waves on the surface or within the volume, reveals the possibility of non-contact and non-destructive material testing by laser ultrasonics.

An example of the acousto-optic effect manifestation in laser ultrasonics is the Brillouin scattering of laser light, where the photons (quanta of the optical wave) of a detection beam inelastically scatter as they cross the volume with the refractive index of the transparent or translucent material perturbed by the laser-generated coherent phonons (quanta of the collective lattice vibrations). Inelastic scattering means that the scattered optical wave will have a different energy from the energy of the incident optical wave. The resulting outcome of such energy transfer is the annihilation or creation of phonon. From the Planck-Einstein relation, the frequency is simply the wave energy divided by a Planck constant. The frequency shift is usually called Brillouin frequency shift or simply Brillouin frequency. The observation of this shift was one of the first experiments conducted in picosecond laser ultrasonics, a sub-field of laser ultrasonics where ultrashort laser pulses are applied for the generation and detection of the coherent acoustic pulses of the picosecond duration, i.e., in the GHz frequency range. In the Fabry-Perot interferometer, this frequency shift is determined from the experimentally registered spectrum of scattered light. In time-resolved technique, oscillations arise in time-domain signals from the interference between the inelastically scattered, Doppler-frequency-shifted, detecting optical wave and the part of the detecting optical wave reflected at the sample surface. Such time-resolved experiments allow revealing the material elastic properties and monitoring the acoustic wave propagation inside the volume. For the determination of the sample thickness, the measurement has to be long enough for the coherent phonons to be transmitted or reflected by a pair of opposite sample interfaces. Sample thickness is equal to the time it takes for the acoustic wave to travel between two interfaces multiplied by the acoustic velocity.

The formation of the theoretical base for laser ultrasonics has started with the photoacoustic (optoacoustic) effect discovery by Bell at the end of the 19<sup>th</sup> century, who gave a detailed description of his observations of the sound generated by the modulated light

[2, 3]. But the *laser* ultrasonics technique could be only created after the invention of a laser in 1960 by Maiman [4]. The development of the methods and techniques that allow the generation of laser pulses with the extremely high peak power (*Q-switching*) and ultrashort duration (*mode-locking*) paved the way to the creation of the *picosecond laser ultrasonics*. This technique is capable of conducting studies of the phenomena in the picosecond and sub-picosecond time scales. The application of the lasers with ultrashort pulse duration ( $\sim 10^{-12} - 10^{-15}$  s) to the materials with short penetration depth at the central wavelength of the laser emission spectrum is a requirement for the efficient generation of acoustic waves in GHz-THz frequency range.

Successfully generated with a short laser pulse, GHz frequency acoustic wave should be detected to extract useful information. One either needs to use a detector operating in the desired frequency range, or to apply more advanced detection techniques compared to the ones usually used in conventional ultrasonics (in the kHz-MHz frequency range). In this work, a pump-probe approach serves for the conduction of time-resolved experiments. A short and sufficiently powerful laser pulse (*pump*) is absorbed by the sample, generating the acoustic pulse. A second laser pulse (*probe*) serves to monitor the pump-induced reflectivity changes. In practice, the pump and probe pulses usually have different wavelengths. The simplest way of doing this is by splitting the laser beam into two parts, with one beam being directed to a second harmonic generator to get the electromagnetic (EM) wave with doubled frequency. For the conduction of precise time-resolved measurements, the time delay between the pump and probe pulses arrival times should gradually increase with constant time increment. In the configuration where a mechanical delay line serves for the time delay introduction, before reaching the sample surface, one of the pulses runs through a retroreflector, placed on the carriage of a mechanical delay line. Linear movement of the carriage results in a gradual increase of the delay between the pump pulse arrival time and the probe pulse arrival time. Another way is to use two synchronized laser sources with a slight offset in the repetition rate, allowing to perform asynchronous optical sampling, ASOPS in short. Combined with a pump-probe technique for the conduction of time-resolved measurements, the methods of optical detection are represented by transient transmissivity or reflectivity detection [5, 6], laser beam deflection [7, 8] or distorsion [9, 10] and optical interferometry [11–13].

One of the directions of the development of the picosecond (laser) ultrasonics was dictated by the need for a reliable technique that could reveal the in-depth profiles of material properties. For example, the inhomogeneous gradient of in-depth characteristics may appear during the process of material curing, which is required for the amelioration of the mechanical strength, with EM radiation (for example ultraviolet, UV) that is non-uniformly absorbed in the volume, thus introducing continuous variations in material properties. The appearance of such kind of inhomogeneity appears in porous low-k ma-

terials when UV radiation is applied to remove the porogen and to augment the rigidity of fragile material. These materials are of great importance for the further development of electronic devices [14]. It was demonstrated experimentally that measurement of the local Brillouin frequency allows the in-depth profiles of the inhomogeneously cured low-k material to be revealed with tens of nanometers spatial resolution [15, 16]. Note, that in Ref. [16], the experiments conducted at several incidence angles of probe allowed to determine separately inhomogeneity of the refractive index and of the sound velocity. In theory, it is possible to ameliorate the depth-profiling technique if amplitude and phase of the acoustic wave are measured separately [17]. Optical interferometry is the method that serves in multiple domains of science and technology, including picosecond laser ultrasonics, where it is successfully applied for the separation of phase and amplitude of the acoustically-induced transient optical reflectivity [12, 13].

The PhD project is devoted to the design and construction of the ultrafast optical interferometer to precisely study the acoustic wave propagation in the volume of solid materials. One of the reason for the widespread use of optical interferometry in multiple domains is that it allows conducting measurements of the mechanical displacements with nanometric precision without physical contact. Our motivation is to separate the phase and amplitude information from our signal thanks to optical interferometry, which was demonstrated experimentally with different types of interferometers. The main application of our interferometer is the study of the depth profiles of materials for the revelation of possible depth inhomogeneities that do not have a particular location but are continuously distributed inside the bulk. With echo-detection-based picosecond laser ultrasonics, localization of such defects, done by monitoring the coherent acoustic pulses reflected by the defects, is currently possible only if the inhomogeneity is strong and abrupt. The aim is to detect slow variations of the physical (elastic, optical, photo-elastic) properties that could appear in materials, cured with EM radiation that is non-uniformly absorbed in the volume. Potentially, the studies could be performed in multiple transparent or translucent samples, as biological tissues or ion-implanted samples. The experimental setup, a fiber-based Sagnac interferometer, was designed. The required components were ordered and purchased. Then the interferometer was assembled and tested. While working on the experimental setup design, the idea was to make it useful not only for the conduction of the depth-profiling experiments but also for creating a more universal tool with other functionalities.

The manuscript is divided into four chapters. The first chapter is devoted to the main phenomena, methods, and techniques on which this work is based. Following an historical perspective, it starts by introducing the concepts of optoacoustic and acousto-optic effects and their use in the frame of the first laser ultrasonics experiments. Then a presentation of the picosecond laser ultrasonics technique is proposed before discussing

general applications and focusing on subsurface imaging and depth profiling of materials. Finally, a review on the optical interferometry and the types of interferometers with the examples of the applications in laser ultrasonics and picosecond laser ultrasonics is presented before proceeding to the goals of this PhD at the end of the chapter.

The second chapter gives a detailed description of the here-constructed ultrafast Sagnac interferometer. The specific solution that was found, a single-mode polarization-maintaining fiber combined with a custom rotation mechanism for precise probe incidence angle control without the perturbations of the optical path, will be described. First tests of the experimental setup are finally presented.

The third chapter proposes first a discussion, from a theoretical point of view, of the expected performance such an interferometric-based setup for time-domain Brillouin scattering measurements should be able to provide. The limitations are discussed, especially with regards to the fact that the detected signal will never be coming only from acoustic contributions. A signal processing procedure allowing to extract the acoustic contributions from the experimental signals is presented. Then, experiments on a homogeneous sample made of GaAs are performed to demonstrate experimentally the possibilities and the limitations of the constructed interferometer. A discussion summarizing the results and the important conclusions that can be drawn from them closes the chapter.

The fourth chapter is intended to give a view of the prospective applications and the conceptual solutions designed during the work with the actual configuration of the experimental setup. The chapter begins with some improvement ideas being born while working with the setup. It is followed by experimental configurations that have not been tested during this PhD work but that could be of interest and hence are mentioned not to forget them. The chapter ends with a discussion on the experiments that are of certain general interest and that should be possible to conduct with the help of the here-proposed interferometric setup.

A general conclusion, summarizing the main discussions and achievements, concludes this manuscript.



# BACKGROUND

---

This chapter will first describe the basic knowledge of the fundamental optical phenomena emerging when a plane wave falls on the interface between two media. Two general effects are of particular interest for this PhD. The first one is the light action on the matter, with the outcome of such interaction being the generation of an acoustic wave (optoacoustic or photoacoustic effect). Another important phenomenon, that is of greatest significance in this study, occurs when the electromagnetic (EM) radiation is scattered/diffracted by the acoustic waves (acousto-optic effect).

Laser ultrasonics is a non-contact and non-destructive method of material characterization, and the method plays a main role in this study. This method is based on optoacoustic and acousto-optic effects, of which a short historical review of the main discoveries that made this study possible will be given in Section 1.1. First publications on laser ultrasonics applications in various studies are briefly reviewed in Subsection 1.1.3 before proceeding to the deeper analysis of opto-acousto-optical techniques. Special attention is given to picosecond ultrasonics in Section 1.2 as an advanced method of time-resolved acoustical spectroscopy that allows the study of the GHz frequency range phenomena.

A quick overview on subsurface imaging and a specific focus on depth profiling by Brillouin scattering are then presented in Section 1.3. The next Section 1.4 discusses the optical interferometry principles and techniques, as well as a review of various applications of the interferometry and how it serves in the here-developed and later-discussed (see Chapter 2) experimental setup, which was designed as an interferometer in a common-path configuration. Concluding remarks summarizing the chapter and discussing the thesis outlook finishes this introductory chapter in Section 1.5.

## 1.1 History, basic principles and first applications of the optoacoustic and acousto-optic effects

In the current work, our interest is towards the testing/evaluation of the acoustic pulses propagating inside the material by optic (laser) means. Therefore, the material should be transparent for probe laser radiation. A first glance at a typical experimental set-up in picosecond acoustics is here proposed (Fig. 1.1) in order to introduce the pump-probe concept and the two effects mainly discussed in this section : the acousto-optic and the optoacoustic effects.

A pulsed titanium-sapphire laser ( $\text{Ti:Al}_2\text{O}_3$ ) serves as a source of the coherent radiation, with the output beam being split into two parts. One part of the radiation (the probe) is routed directly to the experimental setup, and the rest of the radiation (the pump) is routed to and focused on a nonlinear crystal (BBO) for second harmonic generation. Afterwards, the doubled-in-frequency pump beam is directed to the sample, passing through a mechanical delay line before. The movement of the delay line shortens the arrival time of the pump pulse, which can be viewed as probe pulse arrival being delayed. In this work, pump and probe wavelengths are different, the sample is opaque at the wavelength of the pump and, at the same time, it is transparent at that of the probe.

The beams are focused and overlapped on the surface of a sample (see inset in Fig. 1.1). At the time of the arrival of the pump pulses, some fraction of the energy initially contained in the incident pump pulse is **absorbed**, with the generation of the acoustic wave as a result of this absorption, the so-called *optoacoustic effect*; the rest of the energy is reflected/scattered. In linear regimes of the sound generation with ultrashort laser pulses, the amplitude of the photo-generated acoustic wave is proportional to the energy per unit area (fluence) of the absorbed light [18]. In turn, the energy of the incident probe is split into **refracted(transmitted)** and **reflected** waves. The refracted light wave travels inside the volume, where it is inelastically scattered by the acoustic wave, the so-called *acousto-optic effect*.

Before diving into picosecond laser ultrasonics, the purpose of this section is to introduce the basic concepts and to present some first/historical applications of the optoacoustic and acousto-optic effects. First, the (hi)story of their discovery will be told. Second, basic theoretical explanation of the thermoelastic generation of ultrasound and few experimental considerations on how to detect ultrasound with lasers will be given. Third, the examples of first laser ultrasonics experiments will be presented.

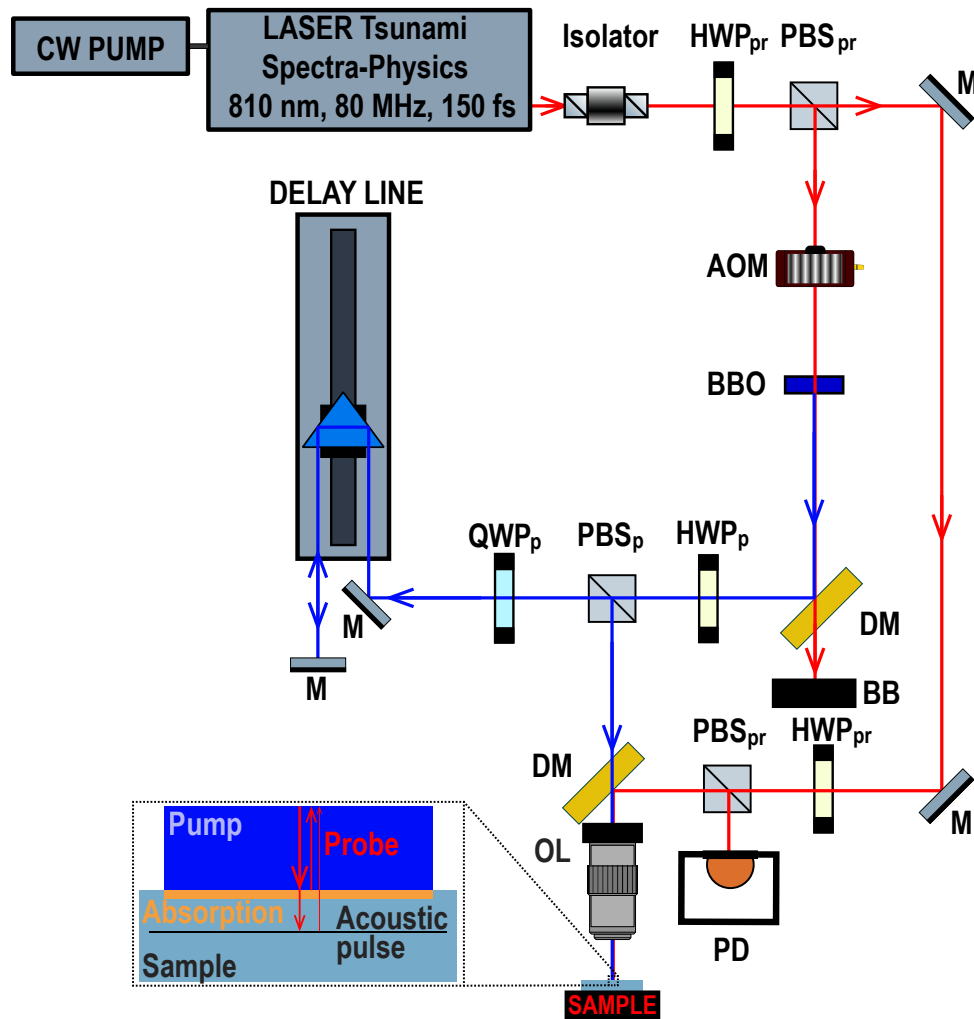


Figure 1.1 – Presentation of a typical experimental set-up in picosecond acoustics. The inset depicts the pump light pulse absorption, which leads to the generation of a propagating acoustic pulse that inelastically back-scatters the probe light pulse.

### 1.1.1 On the discovery, study and first applications of the optoacoustic and acousto-optic effects

As said previously, the photoacoustic (optoacoustic) effect is the generation of the acoustic waves initiated by the light absorption in the volume of the studied material [19, 20]. The incoming laser pulse (or the modulated laser beam) will cause the material surface to rapidly expand due to the introduced energy with the subsequent slow contraction and return to the equilibrium state. This process will result in the generation of the acoustic pulses, propagating away (in depth) and towards the surface of the studied material. The propagation of the acoustic waves can be monitored in time with optical methods, allowing the local study of the material properties. Alternatively, more classical methods such as microphones or piezoelectric transducers could be applied for the detection of the sound waves.

In 1818, Berzelius discovered a new chemical element - Selenium [21]. The following

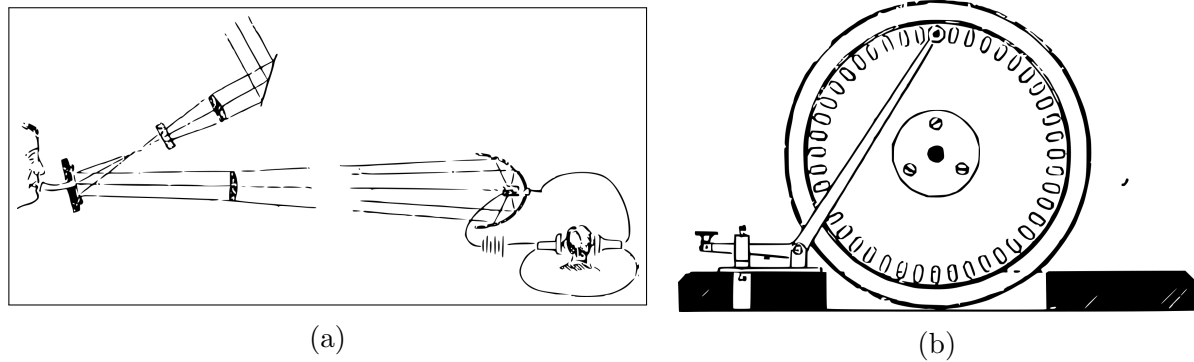


Figure 1.2 – First steps towards the wireless communication, made by Sumner Tainter and Alexander Graham Bell: (a) the principle of the first version of the photophone demonstrated in 1880; (b) a screen-modulator controlled by a Morse telegraph key allowed Morse communication with a remote receiver (reprinted from Ref. [2]).

studies revealed the fact that the electrical resistance of Selenium was decreasing if it is exposed to light [22]. This effect inspired Alexander Graham Bell for the creation of a wireless method for the sound transmission called "photophone" (Fig. 1.2a), reported in 1880 [2], in which the Selenium electrical resistance is modulated by absorbing the sunlight of which intensity was initially modulated by his assistant speech thanks to a pair of fixed and movable perforated plates. The modulated light, collected at a distance from the speaker by a parabolic mirror, was focused onto the Selenium cell. Dependence of the Selenium electrical resistance on the intensity of the incident light led to the possibility of hearing his assistant speech encoded in the electrical resistance modulation made audible thanks to an adapted electrical telephone circuit.

From the time of invention till the next publication, Bell has updated the quality of his photophone. The updated version (see Fig. 1.3) made it possible to hear speaker's voice, but transmission was limited to 40 meters only, due to the instability of the optical elements held in hands.

While conducting his research for the photophone, Bell observed another effect: sound waves were produced directly from a solid sample when exposed to a beam of sunlight rapidly modulated in intensity. This phenomenon occurred when the light was focused on the selenium cell while being modulated by a rotating disk with holes (see disc in Fig. 1.2b). Rapid modulation resulted in more loud sound effect. « A silent motion thus produces a sound » [2]. Bell described in details the investigations of this effect.

He continued to conduct the experiments on solids and noticed the fact that the effect that he had discovered was dependent on how strongly the material absorbed the incident modulated light. The presence of the effect in gases and liquids was demonstrated by Tyndall [23], Röntgen [24] and Bell [3] in 1881.

The experiments with the optoacoustic effect were not giving sufficient reliability and repeatability of the results since the light of the sun was used as a source and the re-

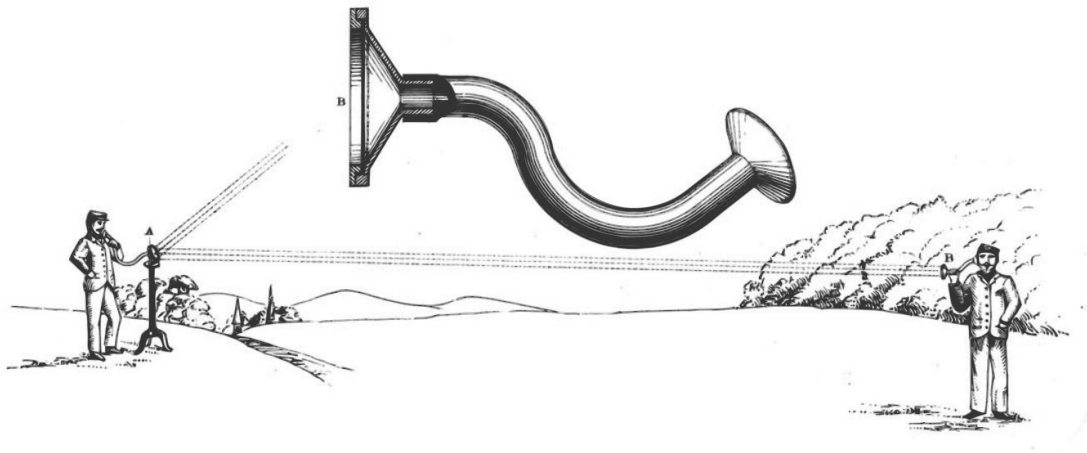


Figure 1.3 – Being a brilliant inventor, Bell kept improving his photophone and proposed more convenient version in 1881 (reprinted from Ref. [3]).

searcher's ear served as a method of sound detection. In addition to this, it became evident that the range of transmission of the photophone was limited by topographical relief and meteorological conditions, which lead to a loss of interest for improving more the photophone and, as a side effect, stopped also the digging on optoacoustic effect.

While the publications on the optoacoustic effect were waiting for the technological advancements, the acousto-optical effect was discovered.

In 1922, Leon Brillouin published a revolutionary paper where he theoretically suggested, that the density fluctuations (continuous vibrations) of the homogeneous body, caused by the thermal agitation, could be studied with the light that travels through this body. The EM wave will be weakly scattered as a result of these fluctuations at normal temperature and pressure conditions. When the body approaches the critical point, the resulting strong density fluctuations will lead to an intense light scattering [25]. As a departure point in the development of his theory, he suggested the decomposition of these density fluctuations into simple elastic waves. Thus the homogeneous body was observed as traversed by the elastic waves of all possible frequencies traveling in all possible directions. Based on this assumption and the previous works of Rayleigh, Einstein, Debye, and Bragg, he has developed a theory of the inelastic light scattering by the elastic wave. This theory is of great interest for the purpose of laser ultrasonics, as it suggests possible the study of transparent and translucent samples. The phenomenon of the light scattering by the ultrasonics waves is referred to as the acousto-optic effect.

To honor the discoverer of the new effect, it was named Brillouin scattering. The inelastic nature of this phenomenon can also be explained as when the traveling acoustic wave introduces a Doppler shift to the light wave that travels in the same propagation medium as the elastic wave. For the consideration of energy, it is better to refer to this phenomenon in quanta terms: a photon (quantum of the EM field) is inelastically scattered

by a phonon (quantum of the collective lattice vibrations). Depending on the coherent phonon propagation direction, the scattered photon will gain or lose a small portion of energy equal to the energy of the phonon involved in this interaction, in other words: the scattered photon will be of higher or lower frequency in comparison with the incident photon.

Independently of Brillouin, a soviet researcher, Leonid Mandelstam, has published a paper devoted to this effect in 1926 [26].

First experimental results, confirming Brillouin's theory, were obtained unintentionally by Gross [27]. The experiments he conducted were concentrated on the Raman scattering in liquids. He observed up to 3 equally spaced diffraction orders from each side of the undisplaced component, the results that he could not explain since they were not consistent with the theory of Raman scattering. A year after the conducted experiments, he suggested that his observations could be related to the light diffraction on the acoustic oscillations, used by Debye in 1912 for the explanation of the varying specific heat in solids. He checked his results using the equation given by Brillouin for the shifted frequency of the light wave inelastically scattered by the sound wave [25]. Since results were in good agreement with the proposed models, he deduced that what he had measured was the spectrum of the oscillations described by Brillouin [27]. In conclusion, Gross proposed a modification to the equation of the Brillouin frequency shift for the higher diffraction orders by introducing an integer multiplier corresponding to the order of diffraction.

In 1932, Debye [28] verified experimentally the possibility of the light scattering following the suggestions of Brillouin [25]. He has observed the light diffraction pattern of high quality and visibility produced when following the recommended experimental configuration (Fig. 1.4): the light was passing through liquid toluene in which an acoustic field at frequency of 5.7 MHz generated by the quartz crystal (immersed in the toluene) was present. The resulting pattern is presented in Fig. 1.5. In addition, he has applied the equation of simple diffraction grating (Bragg's law [29]) to derive the value of the speed of sound, which gave precise values if the angles separating the diffracted beam from the zero-order beam were measured precisely.

Optoacoustic and acousto-optic effects being discovered, one last historical scientific leap was still to be made for the research field of laser ultrasonics to start. In 1917, this last step was provided by Einstein when he predicted the source of the coherent electromagnetic waves [30]. The construction of the first MASER by Townes et al. in 1953 [31] was a significant step forward in science. Shortly after, in 1960, the first laser was built by Maiman [4]. Note that in some early publications, **maser**, or better **optical maser**, are used instead of **laser**, which is the result of the experimentation at the beginning of the laser era when the word was not yet spread and the laser itself was not of such colossal importance as it is for the modern world. Since multiple light detection techniques were already invented, the development of laser revealed the path towards the entirely

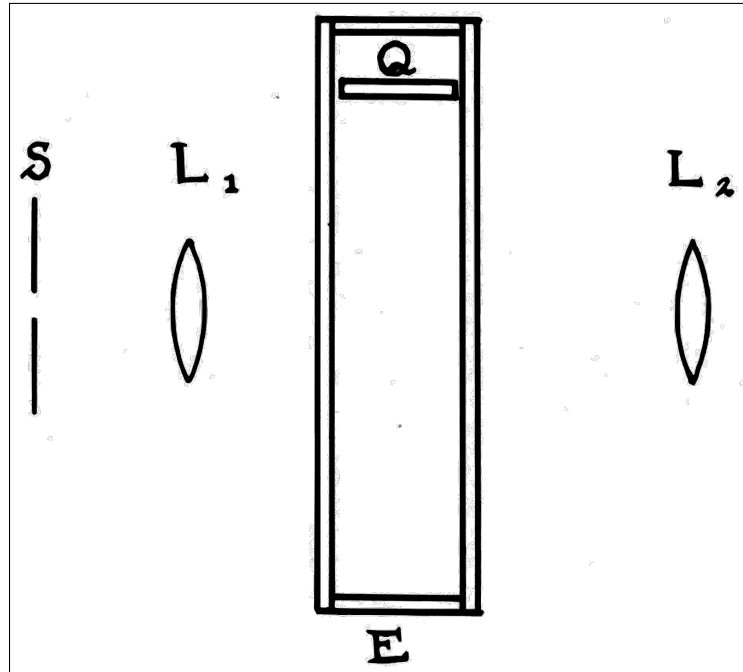


Figure 1.4 – Experimental configuration of Debye for the observation of Brillouin scattering on the acoustic waves. In this figure, a beam of light passes through a slit  $S$  and a first lens  $L_1$  after which it is collimated. The collimated beam of light then enters a trough containing a liquid where it interacts with an acoustic field. The transmitted and scattered light beams are then focused by a second lens  $L_2$  after the trough onto a screen for visualization. The sound is generated by a quartz crystal  $Q$  towards direction  $E$  (downwards) (reprinted from Ref. [28]).

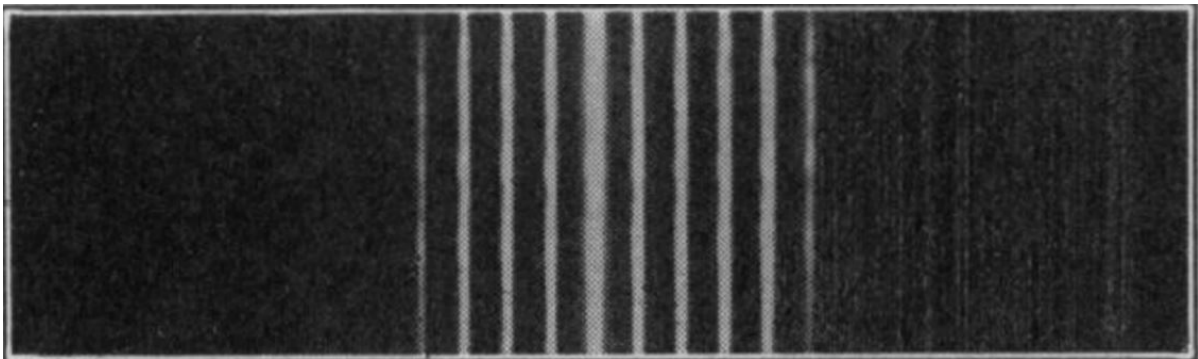


Figure 1.5 – Brillouin scattering observed and photographed by Debye as a result of the implementation of the experimental configuration suggested by Brillouin[25] (reprinted from Ref. [28]).

non-contact method of non-destructive testing known as laser ultrasonics.

Following this historical timeline of the needed effects and tools used in laser ultrasonics, it is now proposed to present basic theoretical explanation of the thermoelastic generation of ultrasound by laser and the experimental schemes allowing their detection using laser as well.

### 1.1.2 Optical generation and detection of the acoustic waves

Different variants of the generation and detection processes have been published and confirmed experimentally, among them theoretical publications, books and reviews [1, 19, 32–38], as well as the articles with theory and experimental demonstrations [5, 39–46]. Deeper study of these processes is proposed in the books by Gusev and Karabutov [18] and by Scruby and Drain [47].

The generation of the acoustic waves in our work results from laser radiation focused on an absorptive body. Depending on the power of the laser source and the physical properties of the studied material, the sound can be generated due to the electrostriction, the deformation potential mechanism, the inverse piezoelectric effect, or else the ablation/plasma mechanism, the latter being destructive for the absorbing material. Another option is the thermoelastic mechanism of sound generation, which does not produce any damage and is now proposed to be described as an example.

Consider an ultrashort laser pulse with duration  $\tau$ , generated by the laser with average power  $P$  and repetition rate  $f_{rep}$ . The energy per pulse is given by the relation  $\mathcal{E}_p = P/f_{rep}$ , the peak power is  $P_{peak} = \mathcal{E}_p/\tau$ . As depicted in Fig. 1.6a, the laser beam irradiates a metallic isotropic film free surface with a cross-section  $s = \pi d_{sp}^2/4$ , where  $d_{sp}$  is the laser beam diameter. The absorption length  $\xi$  of a laser radiation in metals is typically of 10 – 20 nm, while  $d_{sp}$  is two to three orders of magnitude larger. The problem can hence be considered as a one dimensional problem and, assuming an instantaneous absorption, no thermal diffusion and an homogeneous distribution of the laser intensity on the surface, the temperature rise at times  $t \geq \tau$  is time-independent and depend only on  $z$ , the distance from the surface of the metallic film [5, 40, 41, 43]:

$$\Delta T(z) = \frac{(1-R)\mathcal{E}_p}{Cs\xi} e^{-z/\xi}, \quad (1.1)$$

where  $\mathcal{E}_p$ ,  $s$ , and  $\xi$  have been defined above,  $R$  is the optical reflectivity and  $C$  the heat capacity per unit volume of the metal.

As a result of the introduced temperature increase, the isotropic thermoelastic stress instantaneously appears, given by the following expression:

$$\sigma_{th} = -3B\alpha\Delta T(z), \quad (1.2)$$

where  $\alpha$  is the linear expansion coefficient, and  $B$  is the bulk modulus. The gradient of the one-dimensional thermoelastic stress given in Eq. (1.2) is acting as the source of the acoustic wave traveling along the  $z$ -axis.

When the light is absorbed near the surface, the total (elastic plus thermoelastic) stress profile splits in two equivalent counter-propagating parts with respect to the  $z$ -axis. The one that goes to the free surface of the metal will switch the sign after being reflected

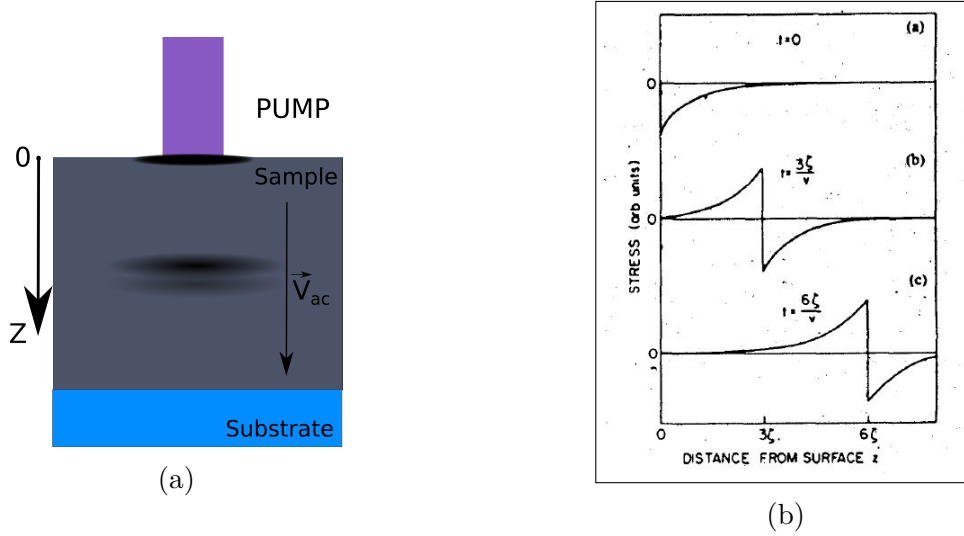


Figure 1.6 – Generation of the acoustic wave in a metallic film. (a) Illustration of the laser beam absorption in the metal film with the visible result of the previous pulse arrival: an acoustic pulse that propagates along the  $z$ -axis direction at the velocity  $\vec{v}_{ac}$ . (b) Total (elastic plus thermoelastic) stress distribution at different instants of time with the generation at  $t = 0$  (reprinted from Ref. [41]). Note that the amplitude of the total stress at  $t = 0$  in (b) has been reduced as it should be twice larger.

by the surface. Fig. 1.6b shows the result of this process [41] by depicting the stress field  $\sigma_{zz}$  in the solid as a function of  $z$  at three different times. The form of the stress pulse launched inside the sample (see Fig. 1.6b, lower panel) is given by the equation [48]:

$$\sigma_{zz}(z, t) = -\frac{3\mathcal{E}_p B \alpha (1 - R)}{2C_s \xi} \left[ \exp\left(-\frac{z + v_{act} t}{\xi}\right) + \exp\left(-\frac{|z - v_{act} t|}{\xi}\right) \text{sgn}(z - v_{act} t) \right], \quad (1.3)$$

where  $\rho$  and  $v_{ac}$  stand for the density and the acoustic wave velocity of the longitudinal mode of the material, respectively. When the acoustic stress travels a distance that is much larger than the optical absorption length  $\xi$ , it takes a bipolar form that can be seen in Fig 1.6b, Eq. (1.3).

The elastic stress is associated with an acoustic strain which locally changes the material density. The detection of the generated acoustic strain pulse allows to study the medium in which it propagates. There are a variety of ways of detecting ultrasound, which can generally be divided into interferometric and non-interferometric methods. There are three basic interferometric techniques, in each case the probe laser beam being split in two parts.

1. Optical heterodyning: the probe beam is split in a probing beam and a reference beam before interaction with the sample. The probing beam is reflected by the surface under study, while an etalon surface reflects the reference beam (see the two wavefronts in Fig. 1.7a). Subsequently, two parts interfere with each other after reflection.

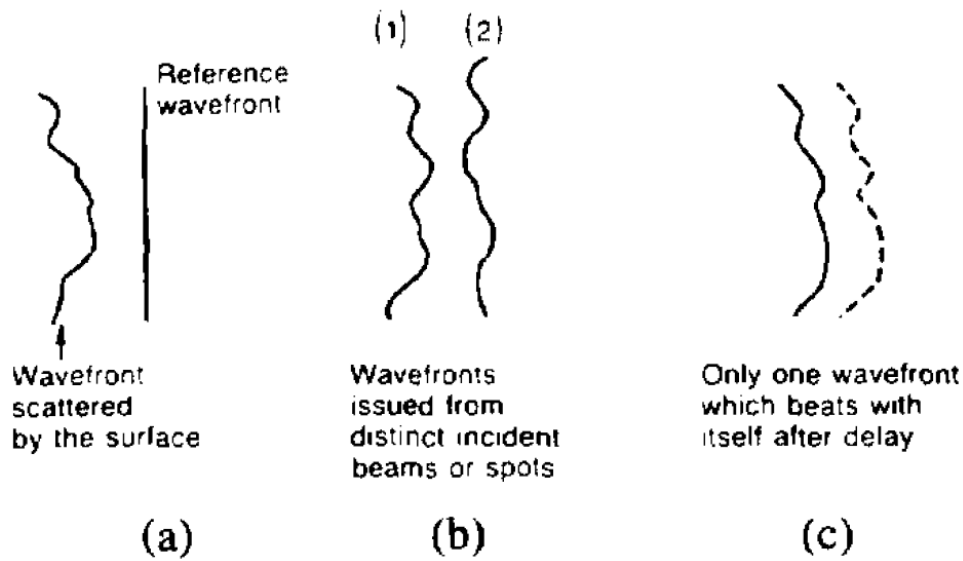


Figure 1.7 – Schematics of the interfering wavefronts representing the main principle of the (a) optical heterodyning, (b) differential interferometry and (c) time-delay interferometry techniques (reprinted from Ref. [49]).

2. Differential interferometry: the probe beam is here also split in a probing beam and a reference beam before interaction with the sample. Both interfering wavefronts are produced as a result of the scattering from the surface of the sample (see two wavefronts in Fig. 1.7b). This technique has two possible configurations: (i) the probing and reference beams are reflected by different points of the sample surface or (ii) light of both beams is scattered from the same point on the sample but the beams hit the surface at different angles.
3. Time-delay interferometry: in that case, the probe, reflected by the surface, is divided in two parts after reflection that are combined again afterwards, but with one of them being delayed in time (see two wavefronts in Fig. 1.7c).

The listed-above techniques are described in details in Ref. [49]. Further details on interferometric techniques used in the frame of picosecond laser ultrasonics, and hence of interest for this work, will be presented in Sec. 1.4.

Non-interferometric techniques are also well developed to detect acoustic waves, since they are designed for the limited applications and in some cases there is no alternative solutions that could offer comparable elementary configuration or lower cost of constructions. Hence, these techniques are widely applied in practice. In particular, the following three techniques have to be noted.

1. The optical beam deflection technique is intended to detect the acoustic wave that propagates on the surface of the sample. The optical beam, obliquely incident on the surface, is reflected towards the photodetector. Between the sample and the photodetector, a convex lens is installed with a knife-edge in the focus cutting 50% of the laser beam and a second lens is used to collimate the beam before it reaches

the photodetector. The acoustic wave propagating on the surface will deflect the laser beam, which will result in the deviation from the 50% of the energy that falls onto the photodetector (see Fig. 1.8). Same scheme may be realized with a position-sensitive photodetector or with normal beam incidence providing the use of a polarizing beam splitter.

2. The optical beam deflection technique is a modification of the optical beam deflection technique for the detection of the surface displacement (and not of its directional derivative) with the normal incidence of the probe beam [9]. The principle of this technique is demonstrated in Fig. 1.9.
3. The reflectivity technique is based on the measurements of the changes of the sample reflectivity, induced by the propagation of the acoustic wave as the acoustic strain is locally changing the optical property of the medium (acousto-optic or photoelastic effect).

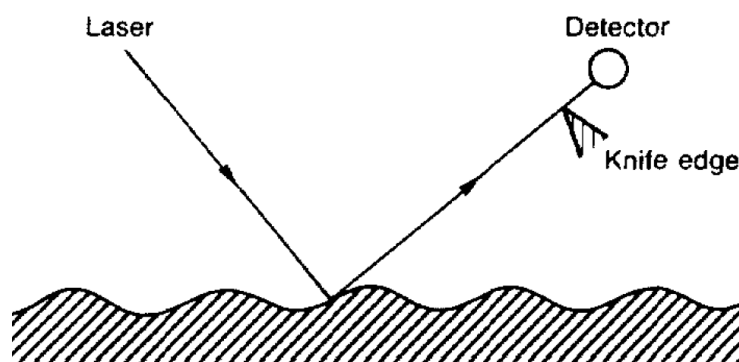


Figure 1.8 – The principle of the optical beam deflection technique (reprinted from Ref. [49]).

Now that the optical generation and detection of acoustic waves have been shortly explained with basic equations and examples, the first implementations of laser ultrasonics experiments paving the way to their use for industrial nondestructive evaluation are presented.

### 1.1.3 First experiments in laser ultrasonics

The first implementations of laser for the photothermal effect excitation appeared shortly after the laser creation [4]. Among the first works one can cite a paper by Brech and Cross [50], and a following patent by Schuch and Brech [51], who have used ruby laser in ablation regime for the local heating of a sample to obtain plasma with subsequent measurement of the spectrum by optical emission spectroscopy. First non-destructive experiments in solids (*i.e.*, in the thermoelastic regime) were conducted by White, who was measuring sound transmission through the elastic body for the determination of the peak-power density of the pulses of EM radiation and related the elastic wave amplitude with

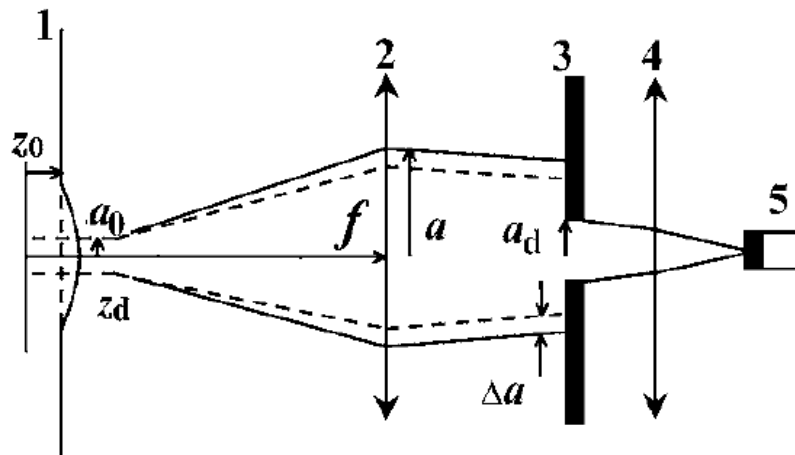


Figure 1.9 – Schematics of the optical beam distortion technique. In this figure: 1 - sample, 2 - objective, 3 - iris diaphragm, 4 - lens, 5 - photodetector;  $a_0$ ,  $a$ , and  $a_d$  represent the radii of the deformation area, probe beam and diaphragm, respectively,  $\Delta a$  shows the change of the probe beam radius,  $f$  is the focal length of the objective,  $z_0$  is the position of the sample surface and  $z_d$  depicts the diffraction length (reprinted from Ref. [9]).

the characteristics of the incident radiation and thermoelastic properties of the elastic body. The EM energy from various sources were used for the excitation of elastic waves (microwave pulses, laser pulses, stroboscopic lamp and a pulsed beam of electrons) with the detection configuration composed of a piezoelectric crystal connected to an oscilloscope. Fig. 1.10 schematically shows the experimental setup used by White [52].

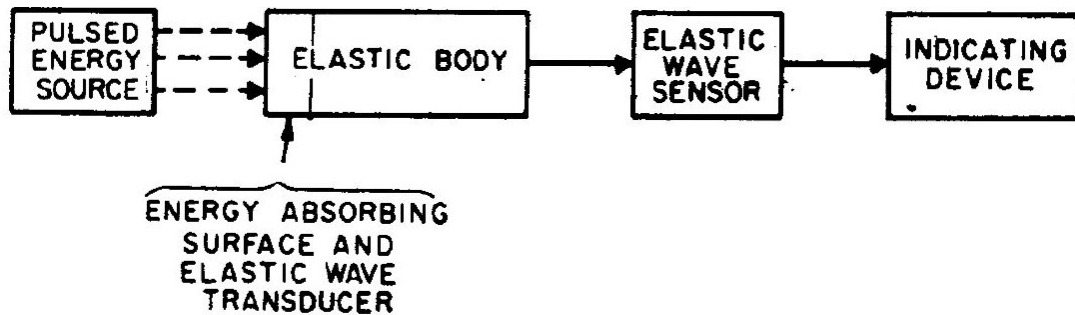


Figure 1.10 – The principle of the experimental setup used by White (reprinted from Ref. [52]).

In 1963, White experimentally proved the domination of the optoacoustic effect over the radiation pressure as a mechanism for the elastic wave generation. A duraluminium tip of an acoustic probe was subjected to the illumination from a pulsed ruby laser with a detected signal being well detailed and with the duration close to the one of the laser pulse. If the radiation pressure had been the dominant factor in the generation of sound, then, in the case of absorbing sample, the signal would have fallen. But when the blackened target was installed on the probe tip, the amplitude turned out to be higher than that observed on duraluminium [53].

More in-depth theoretical analysis of the sound generation by transient surface heating,

complemented by the computations and experiments on several solid and liquid samples, allowed to discover the stress wave amplitude dependence on the type of constraint applied at the heated surface, the relation between the wavelength of elastic waves and the spatial size of the heated zone, and the relation between the frequency content of elastic waves and the time distribution of the source of transient heat [54]. In addition to this, the efficiency of the absorbed EM energy conversion into the elastic wave was calculated for the various tested sources: microwave pulses, laser pulses, stroboscopic lamp and a pulsed beam of electrons [54].

As a side note, but describing close enough effects studied during the same period as White's studies, *i.e.*, in 1963, a soviet physicist Alexander Prokhorov, known for his multiple contributions to the creation of a MASER and LASER (for his fundamental work, he was awarded a Nobel Prize in 1964, that he shared with Nikolay Basov and Charles H. Townes), conducted a series of experiments in liquids with the co-authors [55]. As a first experiment, they observed the formation of bubbles (effervescence) in tap water when an intense beam of the pulsed ruby laser was focused, while high intensity was not essential for the excitation of the phenomena in aerated water. Continuation of the study was the experiment with light scattering on laser-induced bubbles. The explosive boiling (photohydraulic effect) was initiated when a ruby laser beam was focused on the surface of the bouy, immersed in glass cuvette, containing water coloured with copper sulphate for the better light absorption. The photohydraulic effect is analogous to the electrohydraulic effect, where the electric arc discharge vaporizes surrounding liquid with a shock wave being generated as a result. This effect of electrical to mechanical energy conversion is used in industry for the deformation of metallic workpieces.

Although high energy laser pulses were used in the earliest laser ultrasonics experiments leading to damage tested specimens, reducing the laser energy below the damage threshold held ultrasound generation without sample damage, which has hence conforted the burgeoning interest in this technique for non-destructive and non-contact testing applications, further demonstrated by the rapid development and spreading of the laser ultrasonics technique. This led to numerous applications of the technique in the modern industry, for example in the aeroplane construction (see Fig. 1.11), where safety and reliability should not be doubted, discussed or questioned, but has to be monitored continuously. Another industrial field making use of a more advanced laser ultrasonics technique, named picosecond laser ultrasonics, is the semi-conductor industry for which it could provide metrology and defect inspection tools, like those provided by companies such as [Onto Innovation](#) or [Neta](#). In that case, the inspection of transparent materials could take advantage of the Brillouin scattering for detecting propagating acoustic waves. After this section on basic principles/tools related to this PhD work and their first applications, it is now proposed to present, in more details, the picosecond laser ultrasonics technique and the Brillouin scattering phenomenon, the latter being the key ingredient of detection in

this work.



Figure 1.11 – LUCIE - a flexible system for the laser ultrasonic testing of large-scale parts of planes (reprinted from Ref. [56]).

## 1.2 Picosecond laser ultrasonics

The study of the material parameters and the control during the production processes is of great importance for the fundamental science, microelectronics, medicine, et cetera. The group of techniques, that perform this control is called non-destructive testing and evaluation (NDT&E). The main request is that these methods must be non-destructive and, in the cases of fragile materials, for the applications in the production process, or under extreme conditions (high temperatures and/or pressures, ionizing radiations), it is preferable for the method to be non-contact as well.

Picosecond laser ultrasonics, of which an introduction to fundamentals is available in Ref. [48], is such a non-destructive and non-contact technique that can conduct fast measurements in micrometers and sub-micrometers scale samples and structures. It is an experimental technique based on ultrafast high repetition rate lasers applied for the generation and detection of short coherent acoustic pulses (typical duration in a range of picoseconds). In optically transparent materials, these acoustic pulses can be detected along their complete propagation path inside a sample, revealing information on the material elastic, optical, and photoelastic properties in their current spatial position, hence allowing depth profiling of materials. This technique is commonly called either picosecond acoustic interferometry [41], or time-domain Brillouin scattering (TDBS) [57], and the improvement of this technique is under the scope of this PhD thesis. Before focusing on TDBS in Sec. 1.3, it is here proposed to introduce the genesis of picosecond laser ultrasonics and to give a glance of applications of this technique as illustration.

### 1.2.1 Genesis of picosecond laser ultrasonics

To generate and afterwards to study the phenomena in picosecond time scales, the application of the lasers with short (typically less or up to 1-2 ps) pulse duration to the materials with small penetration depth (typically about 10-50 nm) at the laser central wavelength is required. The frequencies of the generated phonons are usually in GHz range.

Study of the phenomena in GHz frequency range requires detectors with capability to detect such frequencies or the techniques that can allow the respective studies without such detectors. The main principle of a widely spread pump-probe technique is presented in Fig. 1.12. In this technique, a short pulse of laser radiation called pump is absorbed by the material volume resulting in acoustic wave being generated, while a second time-delayed short laser pulse called probe is used for the monitoring of the pump-induced changes of the sample (for example in the reflectivity). The example in Fig. 1.12 represents the case where the probe pulse arrival is delayed relative to the pump pulse arrival thanks to a longer optical path elongated at every measurement point (using a delay line), what makes probe pulses to arrive with larger delay each time, hence point-after-point revealing

the information on the whole process.

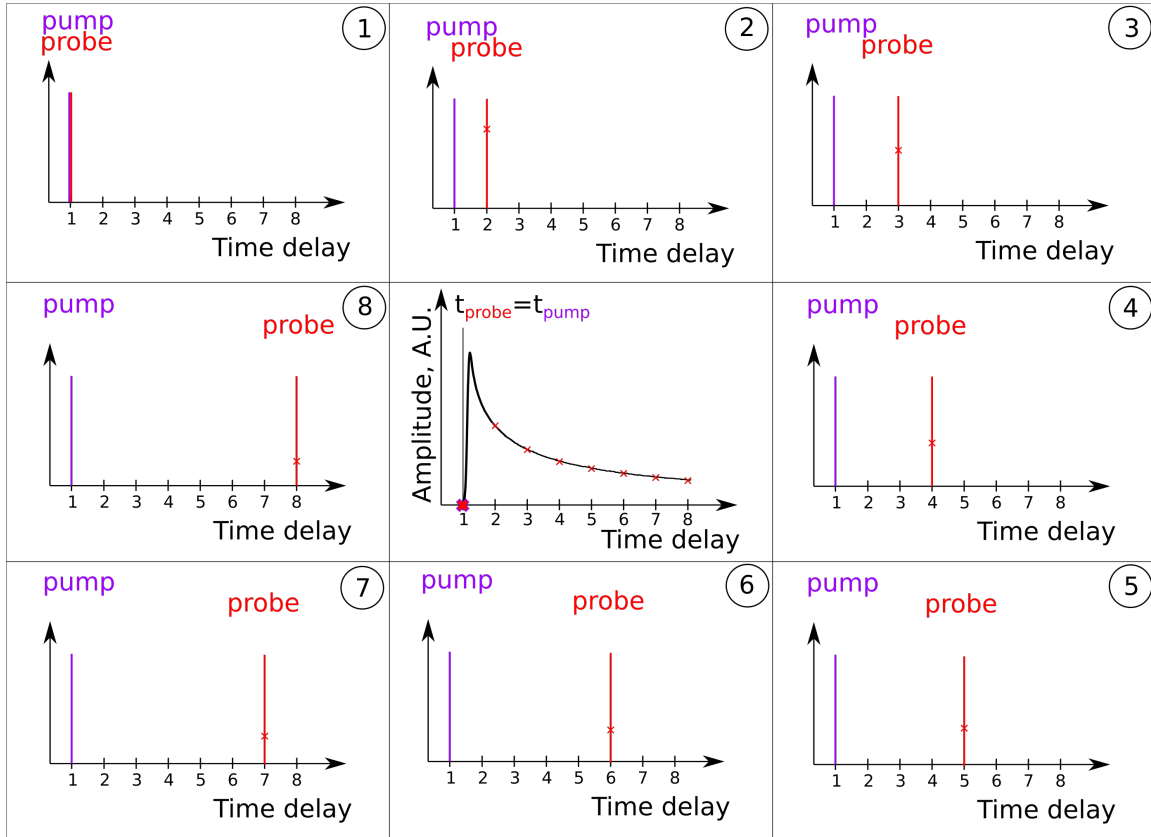


Figure 1.12 – Starting from the top left and going clockwise, the figures represent the delayed arrival times of the probe pulses (delay is introduced by the enlargement of the probe optical path length) relatively to the arrivals of the pump pulses. The probe pulse reflectivity variations introduced by the pump pulse are measured at different time delays after the pump-induced perturbation, as depicted by the 8 red crosses in the central Figure on top of the black solid line standing for another measurement of the same sample response, but with a larger amount of points ( $\approx 4000$ ). To reduce the noises in signal, the averaging is applied to the set of signals, obtained by repeating the entire measurement tens or hundreds of times.

For the evolution from the first laser ultrasonics experiments to the more advanced picosecond laser ultrasonics ones, the main requirement was the sufficiently powerful laser source that could produce ultrashort pulses. In the early 1960s, theoretical work [58] was followed by the experimental confirmation [59] demonstrating the possibility to generate laser pulses with high peak power. The typical laser pulse duration then was in the range of tens to hundreds of nanoseconds. Shortly after the theory of the mode-locking had been proposed by Lamb [60], its experimental implementation was performed by Hargrove et al. [61], who achieved in 1964 the pulse duration of 2.5 ns. Application of passive mode-locking by Ippen et al. [62] allowed to reach the 1.5 ps pulse duration with stable output 8 years later. Further development of this method resulted in the first demonstration of the femtosecond pulses when Shank and Ippen have demonstrated the laser pulses with

700 fs in 1974 [63]. Following the way of improvements of the passive mode-locking, Fork et al. have experimentally demonstrated the generation of the laser pulses as short as 90 fs [64]. A great contribution to the laser ultrasonics was introduced by Moulton, who has constructed the first titanium-sapphire laser in 1982 [65, 66]. The following widespread acceptance in scientific applications was due to the high level of the laser tunability which was expressed in the ability to choose wavelength and pulse duration in a wide range (600-1300 nm and 5 fs respectively was achieved by the authors in Ref. [67]).

The intense development of the classical theory of the generation of the ultrashort acoustic pulses by lasers with the picosecond and subpicosecond pulse duration started in the middle of 1980s. Experimentally, the first acoustic waves with GHz frequencies induced by the laser radiation with picosecond pulse duration were experimentally observed in 1980 by Nelson and Fayer [68], who have observed the Bragg diffraction of the laser light on the acoustic wave in solid. In their experiment, the authors used the delay-line to get the time-resolved signal (see Fig. 1.13a). The sound was generated as a result of the interference of two laser beams inside the sample volume (see Fig. 1.13b and Ref. [69] for the detailed explanation of this sound generation method). The resulting signal, shown in Fig. 1.13c, was observed with clearly visible oscillations.

Although using ps laser pulses which could allow the generation of shorter acoustic pulses than subnanosecond ones observed in Ref. [68], the period of the transient laser grating cannot be shorter than half of optical wavelength, which prevents this technique to generate acoustic waves with picosecond durations. The first report on the generation and detection of acoustic waves with a period of few tens of picoseconds is published by Thomsen et al. in 1984 [5]. As with any experimental method, the result is highly dependent on the equipment used to obtain it. Laser ultrasonics is no exception: as the name suggests, the most important element in the experimental setup is the laser. In their work, Thomsen et al. used passively mode-locked dye laser which produced 1-ps pulses. Yet, this type of dye lasers are often dangerous to health. Therefore, it is worth mentioning the additional impetus given by the invention of solid-state lasers, which also includes the titanium sapphire laser used in our experimental setup. As noted a few paragraphs earlier, it had many advantages over its predecessors, and it was also safe, as the design was free of dyes. With this in mind, lasers began to be used in more laboratories, giving a huge boost to picosecond ultrasonics in particular.

After this quick overview of the origins and development of picosecond ultrasonics, the section continues with a discussion of some examples of applications of this technique.

## 1.2.2 Application examples of picosecond laser ultrasonics

Depending on the application type, the picosecond ultrasonics gives an opportunity whether to improve the detection capabilities of other techniques, by benefiting from mul-

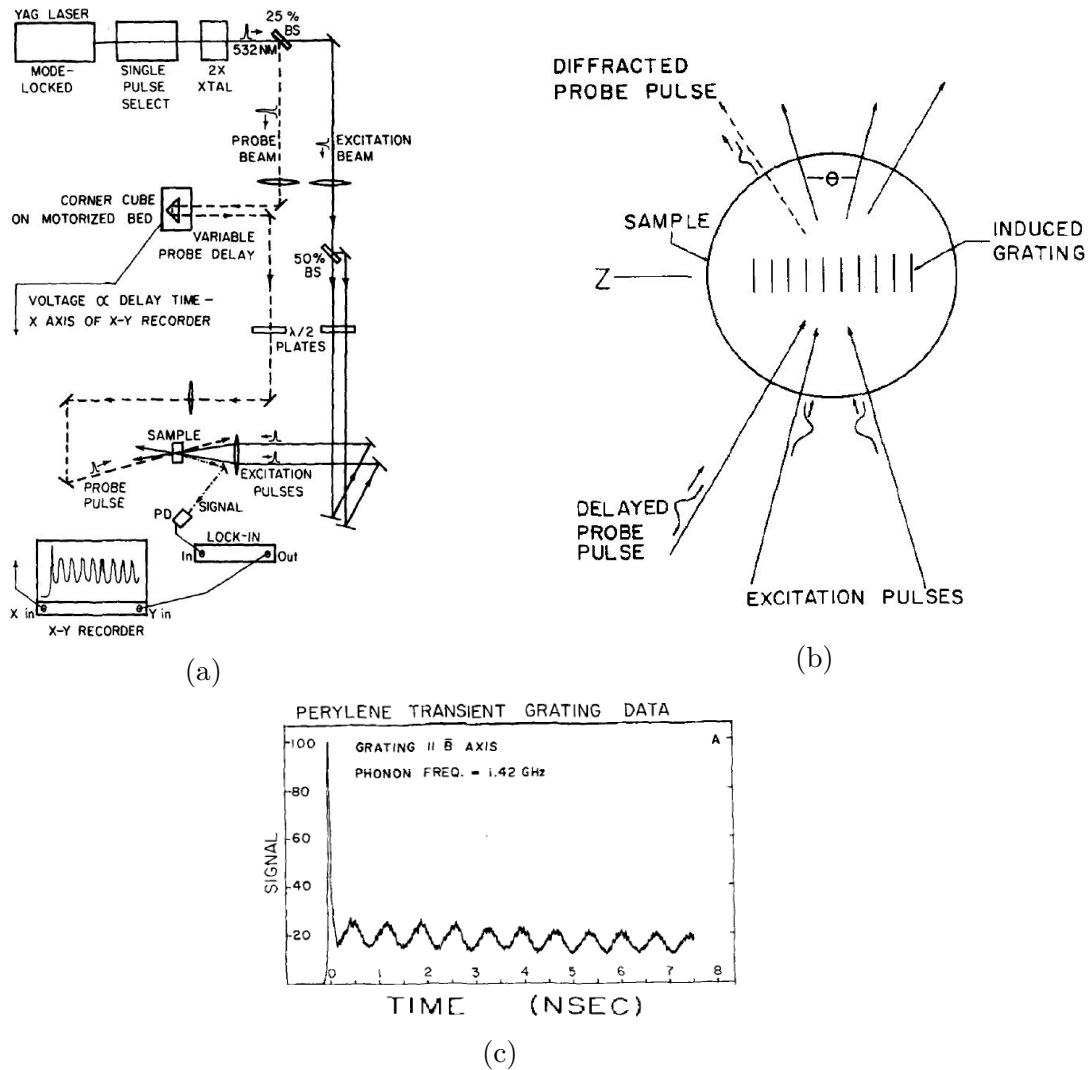


Figure 1.13 – Time-resolved study of the phonon dynamics conducted by Nelson and Fayer in 1980. (a) Experimental setup with the frequency-doubled Nd:YAG laser producing ps-long laser pulses. (b) Interfering pump pulses induce spatial density perturbations. (c) Resulting signal in time domain, showing acoustic signal with 700 ps period (reprinted from Ref. [68]).

multiple and complementary types of contrast properties (elastic, photo-elastic, optoacoustic, electronic, acoustic/optical absorption, ...), or to advance in the studies of the quantum phenomena by introducing and studying the behaviour of, or the interaction of phonons with, the micro- and nanoscale structures, resonators or particles [70].

Lying on the richness of contrast properties and on the ability of generation and detection of coherent acoustic phonons, picosecond ultrasonics spread among, and have been applied in, many scientific fields such as applied physics, materials science and engineering, nanoscience and nanotechnology, chemistry, computer science, energy, earth and planetary sciences, and biology.

Starting from the pioneer application reported in 1984 by Thomsen et al. [5], where they measured clamped-free resonances of thin films to measure velocity and attenuation

of phonons, picosecond ultrasonics have been widely used for layered structures characterization, from single and multi-layered thin films to homo/heterostructures of van der Waals materials [71–73]. Micro- and nanoscale resonators have also been investigated, such as gold nano-dots [74], gold nano-bells [75, 76], gold nano-rods [77], metallic nanoparticles [78] and free-standing [79] or deposited-on-free-surface nanowires [80]. The superlattice structure has been used for the possibility it offers to generate and detect acoustic waves with the frequencies from hundreds of GHz up to the record 1.4 THz [81–83]. This structure is also a playground for the study and use of interactions between phonons and other quantum particles or quasi-particles, such as photons [84], magnons [85] or electrons [86].

Picosecond ultrasonics have also been recently introduced as an investigation tool for the fundamental research in the fields of geosciences and astrophysics in order to study materials compressed to Mbar pressure in a diamond anvil cell. For example, it has been used to determine the elastic properties of opaque materials [87–89] and to measure thermodynamic properties of materials [90], in both cases from time-of-flight measurements of skimming acoustic modes, bulk acoustic modes and/or head waves.

Picosecond ultrasonics has also been widely used for imaging and characterization of biological cells [91]. For example, images of the stiffness and adhesion to a metallic substrate of single migrating stem cells have been obtained based on the reflection of laser-generated GHz acoustic waves at a cell-metal interface [92]. Using time-of-flight measurement, picosecond ultrasonics has also been recently used for thickness mapping of a single cell [93]. Many works on cells face the same issue of low-damaging threshold due to laser actions hence forcing the researchers in developing specific solutions, such as in Refs. [92, 93], for protecting the cells and/or improving the ultrasound generation and/or the detection sensitivity.

Although pulse-echo or time-of-flight measurements are interesting solutions for the study of biological cells and of materials under high pressure, the constituent of biological cells and some materials can be transparent to visible light. This makes them suitable for time-domain Brillouin scattering experiments, in order not only to characterize mechanical contacts or height for cells, or else averaged mechanical or thermodynamic properties for high-pressurized polycrystalline transparent materials, but also in order to perform 3D characterization and imaging with optic-related lateral and/or acoustic-related axial resolution.

Far from being a complete overview of the applications one could find in the literature related to picosecond ultrasonics, this glance of possibilities illustrates how rich is the variety of its applications. It is clear that picosecond ultrasonics is an interesting tool to perform subsurface imaging and depth profiling at the nanoscale. The next section, after a quick overview on subsurface imaging, is focusing on depth profiling by Brillouin scattering, especially on the specific field of picosecond ultrasonics known as time-domain (or time-resolved) Brillouin scattering.

## 1.3 Subsurface imaging and depth profiling by Brillouin scattering

Subsurface imaging and depth profiling aim to study the material beneath the surface, along depth. The difference between the two categories of methods is that subsurface imaging is used to obtain images of what is below the surface of the sample by using any kind of contrast in material properties to which the technique is sensitive to, while depth profiling aims at characterizing the sample, *i.e.*, at evaluating local properties of the material as a function of depth, such as the chemical composition or the elastic properties [94, 95].

### 1.3.1 Classical methods of subsurface imaging at the micro- and nanoscale

There are many subsurface imaging techniques allowing the visualization of the objects within the volume of solid, liquid and gas media. It has been seen in section 1.2 that picosecond ultrasonics is one of such subsurface imaging techniques, allowing echography-like imaging of multilayered structures, to remind only one. Despite being out of the scope of our research, it is worth mentioning few other approaches restricted to the case of micro/nanoscale without going into details, nor being exhaustive, before proceeding to the more detailed presentation of the depth-profiling, with a focus on the use of TDBS.

Besides x-ray-based techniques needing synchrotron radiation to reach nanometer resolution [96], the most successful approaches to date to reach such resolution with table-top equipments are electron microscopy (EM) or scanning probe microscopy (SPM) [97]. The drawbacks of EM techniques are usually the required vacuum condition to operate and the needed extensive sample preparation [98], with the extra need of tedious sectioning in the case of transmission EM. Furthermore, the contrast property in EM essentially imposes the presence of conductive material to allow imaging. On the other hand, SPM has been attractive for its ability to perform subsurface imaging of non-conductive materials [97].

Atomic force microscope (AFM) is, together with scanning tunneling microscope, a basis of design for probe-based microscopy techniques (see Ref. [98], especially section 23, for further details). In short, an AFM makes use of a cantilever with a sharp tip at the end and can be applied for the topography characterization, surely the most known AFM application, but also for much more. For example, the possibility to detect sample mechanical vibrations [99] combined with whether classical AFM [100] (ultrasonic force microscopy (UFM)) or with dynamic force microscopy [101–103] (mode-synthesizing atomic force microscopy (MSAFM)) allows to see the subsurface features of biological and synthetic materials with nanometer resolution. Another example is the scanning near-field ultrasound holography method [104, 105] that have improved spatial resolution and depth

information compared to UFM and have been proved to allow imaging not only of semiconductor structures but of biological samples as well. Using optical contrast, methods such as probe-assisted scattering-type scanning near-field optical microscopy (s-SNOM) [106] or probe-free microsphere-assisted phase shifting profilometry [107] are also used for nanoscale subsurface imaging. The typical depth of imaging in AFM-based SPM is in the range of tens, rarely up to hundreds, of nanometers (see tables in Ref. [97]), yielding the necessary use of tedious sectioning, hence destroying the sample, to reach few micrometers depth of imaging, which is not suitable or possible in all cases.

Using different operating modes, designs or probe types/materials of AFM-based SPM, it is also possible to perform functional imaging (*i.e.*, to probe in-depth physical and/or chemical properties) [97] which, combined with sectioning, can lead to depth profiling of some material properties, yet destructively. In the case of transparent materials, the use of the inelastic Brillouin scattering interaction between phonons and photons might be used for nondestructive depth profiling at the micro- and nanoscale, which is now presented.

### 1.3.2 Depth profiling by Brillouin scattering

Brillouin scattering is an inelastic interaction between an electromagnetic wave and a medium motion, meaning that, if restricting the medium motion to acoustic modes, the photon scattered by a phonon will gain or lose the energy equal to the energy of the phonon that was annihilated or created as a result of this interaction. This is illustrated in Fig. 1.14. If the incident photon (represented by its wave vector  $\vec{k}_{op}^i$  in Fig. 1.14) gains

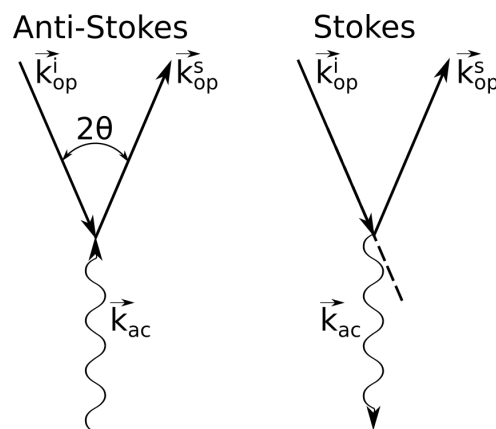


Figure 1.14 – Inelastic scattering of a photon with creation (Stokes) or annihilation (anti-Stokes) of a phonon.

energy, this is due to the phonon ( $\vec{k}_{ac}$ ) being annihilated with the scattered photon ( $\vec{k}_{op}^s$ ) carrying more energy than the incident one: this is called Anti-Stokes scattering (left in Fig. 1.14). The opposite process, Stokes scattering (right in Fig. 1.14), corresponds to the case where the scattered photon carries less energy than the incident one, and hence the phonon was created. The frequency shift of the scattered photon, the so-called Brillouin

frequency shift  $f_B$ , is related to the refractive index  $n$  and the acoustic mode velocity  $v_{ac}$  by the following equation [57]:

$$f_B = \frac{2nv_{ac}}{\lambda_0} \cos \theta, \quad (1.4)$$

where  $\theta$  is the angle between the incident photon and the interacting phonon and  $\lambda_0$  stands for the wavelength (in vacuum) of the incident light. To obtain Eq. (1.4), the momentum conservation law should be applied, as detailed in Appendix A. Note that, as explained also in Appendix A, the definition of  $f_B$  that could be found in the literature may vary depending on the chosen definition for the angle of interaction.

The key point conveyed by the expression of  $f_B$  [Eq. (1.4)] is the linear proportionality of its value with the product  $nv_{ac}$ . The knowledge of one of this parameter or the measurement at two different angle  $\theta$  hence provide the opportunity to measure the other property or both. Finally, using a microscopy technique to select the volume within the sample where the interaction occurs provides a way to perform depth-profiling of transparent materials. Of course, using  $f_B$  as a contrast properties allows using Brillouin-scattering-based methods as an imaging technique.

Brillouin-scattering-based methods could be divided into two main categories, depending on the way  $f_B$  is measured. One can distinguish between, on the one hand, frequency-domain Brillouin scattering (FDBS) and, on the other hand, time-domain Brillouin scattering (TDBS). In the case of FDBS, the detection of the Brillouin shift is achieved by using a spectrometer, for instance based on a Fabry-Perot interferometer. In the case of TDBS, photons scattered by the propagating coherent acoustic phonons are heterodyned with reflected photons on a stationary surface and fed to a photodetector delivering a signal with an oscillating component at the Brillouin frequency. The frequency-shifted light scattered by phonons is mixed on the photodetector with reference (un-shifted) reflected light, revealing low difference frequency (the frequency of the phonon which scattered the light).

Since « TDBS can be viewed as a replacement for [frequency-domain] Brillouin scattering and [frequency-domain] Brillouin microscopy [108, 109] where nanoscale spatial resolution in materials characterization is either required or advantageous » [57], the imaging and characterization application fields are similar [57]: thin films; ion-implantation and damage by radiation; polycrystalline aggregates and textures; residual stress, temperature gradient; sound absorption; biological and animal cells. Some illustrations are now proposed.

### **Depth profiling by frequency-domain Brillouin scattering**

Using confocal microscopy configuration to accurately select the Brillouin scattering volume, works by Kosky and Yarger [108] and by Scarcelli et al. [109, 110] opened an avenue for the use of Brillouin microscopy in biomedical and biomaterial sciences [111–115],

as well as in material science, to help investigating novel materials, nanostructures and devices [116, 117]. Note that in confocal microscopy, the depth profiling can be performed when the position of the laser focus is changed along the depth direction inside the sample.

Up to now, to our knowledge, the smallest scattering volume in FDBS has been reported in the case of confocal Brillouin microscopy [109, 110] to be of  $0.5 \times 0.5 \times 2 \mu\text{m}^3$  with dry objectives, and down to  $0.3 \times 0.3 \times 1.1 \mu\text{m}^3$  using an oil-immersion objective [118]. Although Brillouin scattering is also widely used for probing, in geosciences, elastic properties of material compressed to high pressure in a diamond anvil cell, as reported for instance in the review article by Speziale et al. [119] that contains numerous examples, the confocal configuration used in Brillouin microscopy is not yet available with the long-working distance objective needed to reach pressurized sample within a diamond anvil cell. For such applications, turning from FDBS techniques to TDBS ones is currently the only option allowing to assess elastic properties of material under high-pressure with micro- to nanoscale axial resolution.

### Depth profiling by time-domain Brillouin scattering

The use of TDBS to perform depth profiling of water ice compressed up to 84 GPa has been reported in 2015 by the group in which this PhD work is conducted [120]. Combined with a one-dimensional lateral scanning of the pressurized sample, it allowed to study the texture/structure of polycrystalline materials [120, 121]. Further uses of the same approach have then allowed to measure the elastic properties of water ice [122] and argon ice [123] as a function of pressure, to follow phase transition [124], or else to perform 3D characterization of individual grains of coexisting high-pressure  $\text{H}_2\text{O}$  ice phases [125]. The latter benefited from the developing use of TDBS for three-dimensional imaging of polycrystalline materials at ambient pressure [126–129]. The application of TDBS for subcellular imaging inside plant and animal cells [91, 130–132] has also started in 2015, benefiting from numerous past demonstrations and realizations of the ability of TDBS to image/characterize inhomogeneous solid and liquid media along depth. As a timely and documented review paper [57] on that topic is available, only few relevant publications are chosen to be detailed in the following. Note that, compared to FDBS by confocal microscopy technique, the depth profiling by TDBS can be performed without any need of changing the position of the laser focus inside the sample.

Among the publications of depth profiling by TDBS of importance for this PhD thesis, the work of Coté and Devos comes first, since they proposed a method for extracting the refractive index and the sound velocity by means of an experimental setup (Fig. 1.15a) in which, by turning the sample, the incidence angle of the probing beam was changed. According to the law of conservation of momentum, this made possible to detect other acoustic frequencies (Fig. 1.15b) and hence, by measuring the Brillouin frequency at two fixed incident angles, to determine the refractive index and the speed of sound in the

material under study separately, *i.e.*, not only their product.

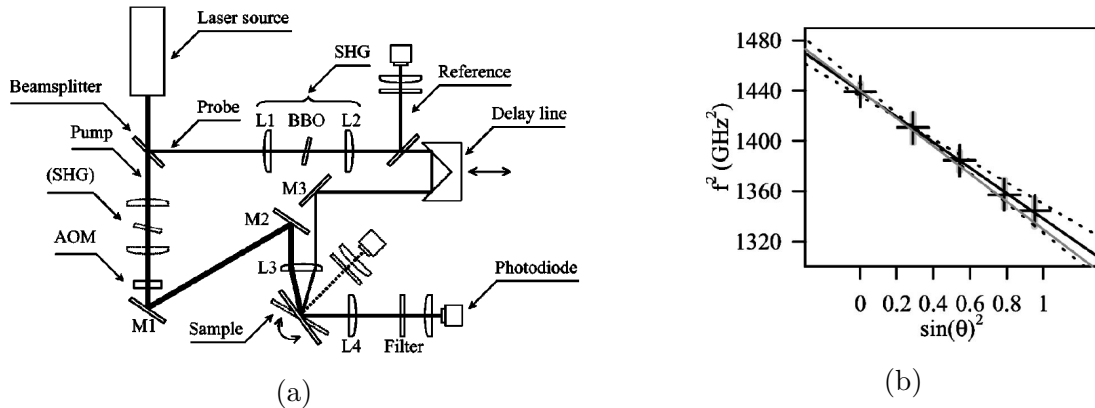


Figure 1.15 – Study of the Brillouin frequency dependence on the angle of the probe incidence: (a) experimental setup, (b) Brillouin frequency variation as a function of probe incidence angle (reprinted from Ref. [133]).

The next important step in the development of depth profiling by TDBS was the work of Steigenwald et al. [134, 135] who, using the classical layout of a picosecond laser ultrasonics setup (Fig. 1.16, part (a) in the left part), measured the Brillouin frequency in gallium arsenide and then repeated the experiment, pre-damaging the same sample with ion bombardment. The difference in amplitude of the detected oscillations between the two measurements (Fig. 1.16, part (c) in the left part) made possible to localize and determine the size of the damaged area, which agreed very well with the simulation results (Fig. 1.16, right part).

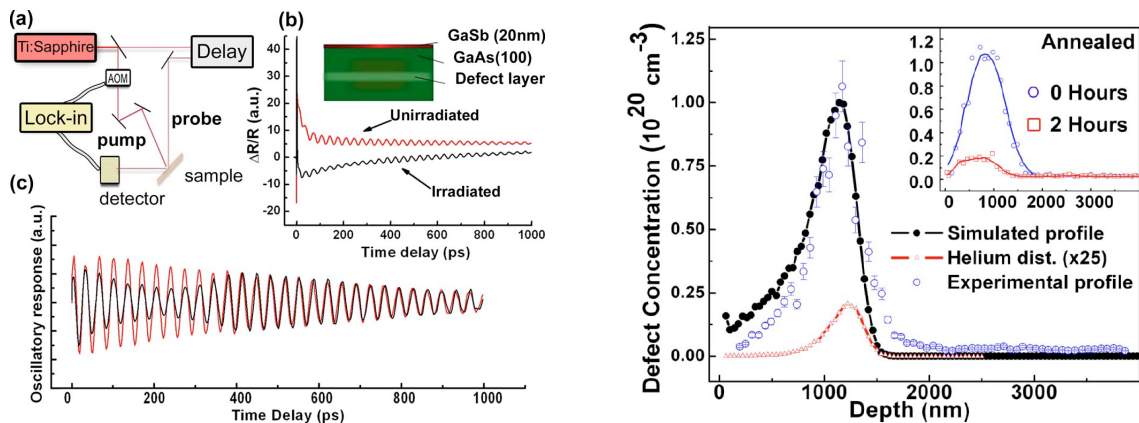


Figure 1.16 – (left) Experimental setup (a) used in Refs. [134, 135], examples of raw transient reflectivity signals (b) and of their background-free oscillating parts (c) in irradiated and unirradiated GaAs samples. (right) Profile of the damaged sample, with the damage being induced by the ion bombardment, obtained from the difference between the amplitudes of the Brillouin oscillations measured in the sample before the damage was introduced and after the ion bombardment (reprinted from Ref. [134]).

A nonlinear evolution in sound velocity and elastic modulus of an inhomogeneously cured low- $k$  material has been measured by Mechri et al. [15], who used curve fitting to

estimate how strongly the Brillouin frequency changed as a function of distance from the free surface (Fig. 1.17). Few years later, Lomonosov et al. [16] carried out an experiment

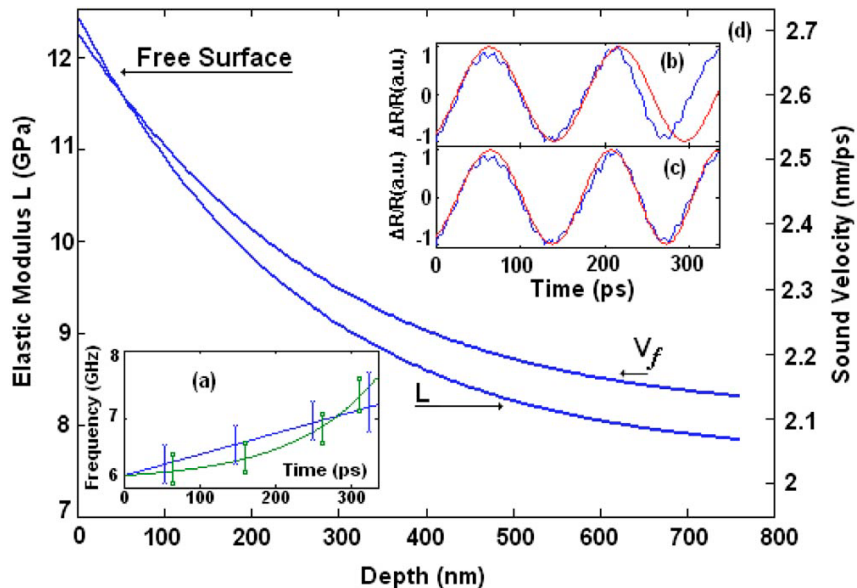


Figure 1.17 – A nonlinear evolution in material elastic properties as a function of depth, caused by the UV curing, can be seen as a decrease of sound velocity and longitudinal modulus starting from the free surface side, from which sample was UV irradiated. Insert (a) shows linear and exponential variations in the instantaneous frequency with time deduced by fitting the data. Inserts (b) and (c) depict the comparison between the experimental background-free oscillating signal and the fit with constant and exponentially-varying frequency with time, respectively, the later law being proved to provide the best fit (reprinted from Ref. [15]).

measuring the Brillouin frequency at several angles of incidence of the probing beam, which allowed to profile how the speed of sound and the refractive index change with distance from the free surface. The in-depth characterization is based on the extraction of the *local Brillouin frequency* from the experimental data, with the spatial resolution limited by the half-period of the oscillation ( $\Lambda_{ac}/2$ ). These half-periods are defined by the time between two subsequent local extrema or two subsequent zeros of the sine function that represents the Brillouin oscillations in a measured signal.

The methods proposed by Coté and Devos, Steigenwald et al., Mechri et al., and Lomonosov et al. are of great importance for the material studies [15, 16, 133–135]. Yet, to date, all TDBS depth-profiling and imaging are based on the transient intensity reflectivity measurements,  $dR/R$ , which give the access only to the amplitude and not to the phase of the transient electromagnetic field reflectivity  $dr/r$ , since  $R = rr^* = |r|^2$ . Because of that, the time-varying Brillouin frequency shows up as the time-dependent frequency of the oscillation in time-domain signals and should be extracted locally by signal processing, which commonly limits the time resolution in determining the Brillouin frequency to a part (fraction) of the Brillouin oscillation period.

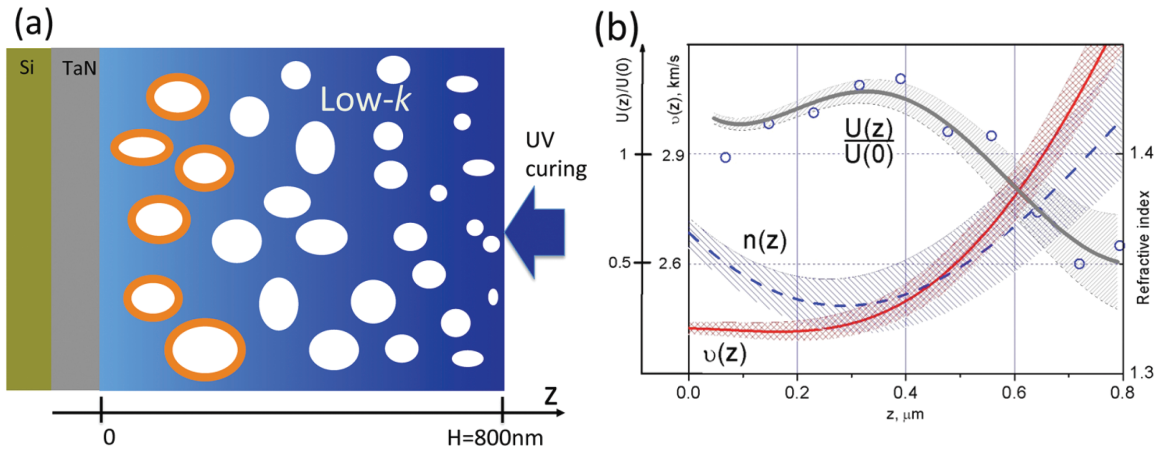


Figure 1.18 – (a) Sample of low- $k$  material studied by Lomonosov et al. and (b) the obtained results showing the profile of sound speed and refractive index as a function of depth, caused by the UV curing (reprinted from Ref. [16]).

Theoretically, the information on the local refractive index  $n(t)$  and acoustic velocity  $v_{ac}(t)$  is « hidden » inside the change of the phase shift between the acoustically-scattered light and the reflected light, used for heterodyning, i.e., in variations of the phase of  $dr/r$  [17, 57]. This phase is proportional to the optical thickness of the media, separating the coherent acoustic pulse and the stationary surfaces/interfaces reflecting the probe light. Thus, the phase shift variation during the small time interval  $dt$  depends on the local refractive index in the position of the coherent acoustic pulse,  $n(t)$ , and the CAP displacement,  $v_{ac}(t)dt$ , which controls the change of the geometrical thickness of the media separating the coherent acoustic pulse and the stationary surface/interfaces reflecting probe light. Therefore, the information on  $n(t)$  and  $v_{ac}(t)$  is contained in the time derivative,  $\frac{\partial \varphi_r}{\partial t}(t)$ , of the transient optical field reflectivity phase,  $\varphi_r(t)$ . In the most common situation for applications, there are a single optical path for the probe light scattered by the acoustic pulse and a single optical path for the reflected probe light. For example, this situation is encountered where the coherent acoustic pulse is launched from the surface of the semi-infinite sample, with material inhomogeneity only in the direction normal to its surface. In this case, the probe light is scattered once by the acoustic pulse and reflected once at the surface, and the time derivative of the transient optical field reflectivity phase reads:

$$\frac{\partial \varphi_r}{\partial t}(t) = 2n(t)v_{ac}(t) \cos \theta(t), \quad (1.5)$$

where  $\theta(t)$  is the local angle between the propagation direction of the coherent acoustic pulse and that of the probe light inside the medium. Therefore, in general, there is even no need in the discussion/definition of the Brillouin oscillation and of the Brillouin frequency for the determination of the local product  $n(t)v_{ac}(t)$  of the medium inhomogeneous along depth. This product is determined by the time-derivative of the transient optical field reflectivity phase  $\varphi_r(t)$ , which should be either measured and then differentiated or the

experiment should be organized in order to measure directly this derivative [136]. As theoretically the time derivative can be evaluated between the two neighbors-in-time measurements of the signal, it is expected that the experimental measurements of  $\varphi_r(t)$  would allow studying the ultimate axial resolution of the TDBS imaging, which is currently precluded by the necessity of the use of signal processing methods.

It is well established that both the real and imaginary parts of  $dr/r$  can be measured separately using optical interferometry, and, thus, the amplitude and the phase of  $dr/r$  could be determined separately.

Next section is devoted to the optical interferometry. Since this detection technique is the core of the experimental development and main achievements of this PhD research, an introductory part to optical interferometry, followed by a brief motivation of its use for TDBS, is exposed, before proceeding to the applications of different interferometers in order to find the scheme suitable for the construction of our experimental setup allowing an easy variation/adjustment of the probe incidence angle.

## 1.4 Optical interferometry

Optical interferometry is a technique, that uses the phenomenon of the interference for the applications in various domains such as chemistry, biology, medicine, seismology, physics, engineering, holography, velocimetry, the most significant being, according to the author, the applications in astronomy (the first direct detection of the gravitational waves [137]) and the important proof against the theory of « luminiferous ether » (ether in short) while trying to detect the ether during the experiment conducted by Michelson and Morley in 1887 [138].

The phenomenon of interference is based on the superposition principle. In the most simple case, it is the interaction of two coherent or quasi-coherent waves when they are superposed with a resulting amplitude being redistributed in space. If two monochromatic waves are in phase, the result of this energy redistribution will be the wave with the sum of their amplitudes (constructive interference), while, if they are  $180^\circ$  out of phase, the resulting amplitude will be equal to the difference of the amplitudes (destructive interference).

An example of an optical interferometer application is its use for quality control of optical surfaces. For such application, a Michelson interferometer is often used (shown in Fig. 1.19). The interferometer operation is based on two beams obtained by splitting, with a beam splitter (BS), the beam from a light source into two parts, that are reflected from the reference surface (reference beam) and the sample (probing beam). After being reflected from the respective surfaces, both beams interfere at the BS with the resulting interference pattern being detected with the photodetector.

In the case of TDBS, it has been theoretically predicted that the use of an interferom-

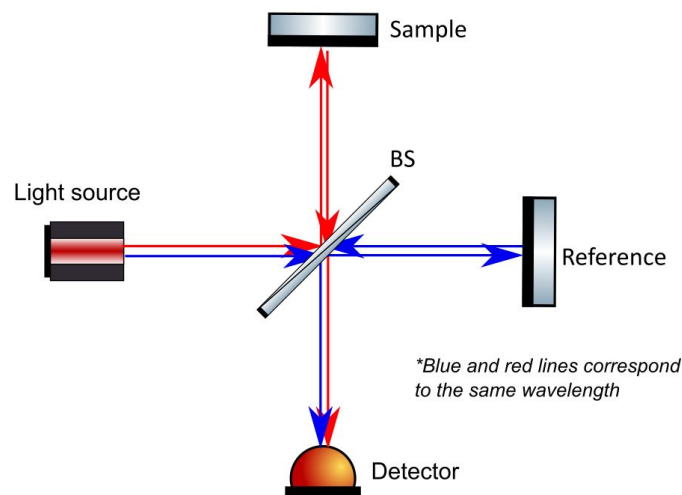


Figure 1.19 – The principle of the Michelson interferometer.

eter can give an advantage over the more conventional method of reflectometry detection [17]. The theory indeed indicates that the ability offered by an interferometric technique to measure the temporal evolution of the complex transient optical field reflectivity provides multiple possibilities for depth profiling of inhomogeneous distributions of elastic, optical, and acousto-optical properties of the tested transparent material. In order to get rid of the effects of « poisoning » slowly time-varying contributions to reflectivity, it is also proposed, in Ref. [17], to work with different polarizations and/or incidence angles of the probe light. In short, being able to measure real and imaginary part of the transient optical reflectivity time variation associated to the coherent acoustic pulse propagation should allow to have access to the best axial resolution the TDBS technique can offer: the characteristic length of the acoustic pulse. That way, the axial resolution should not be limited anymore by the signal processing that is usually used to extract local frequency and amplitude from the real part of the signal only, with axial resolution limited to a part of the acoustic wavelength in the best case.

The above-discussed theoretical expectations are the ground basis of the motivations behind the work reported in this PhD thesis and make clear the reason why we are interested in implementing an interferometric technique to use for the study of the acoustic wave propagation, since it allows to measure both the phase and the amplitude of the transient optical field reflectivity, while the conventional techniques allow only the measurement of its real part. After a short section discussing different types of interferometer, a focus on the Sagnac interferometer will be proposed, discussing its use in picosecond laser ultrasonics and short theoretical considerations.

### 1.4.1 Inadequacy of several interferometric schemes to our objective

The demonstration of the optical interferometry for the sensing of the phase shift in ultrafast process was first conducted in Ref. [139], where the modified Michelson interferometer was used to show the effect of the induced phase modulation in absorptive materials. The Michelson interferometer in multiple configurations was used for the studies of the laser induced plasma [140], and in communication technologies [141]. It has also been used in picosecond acoustics experiments, although it was not the very first configuration to be implemented. Using a stabilization, detections of sub-GHz surface acoustic waves [142] or of bulk longitudinal and shear acoustic wave echoes of high-frequency content ( $\geq 1$  GHz) [143] have been realized. Using a rotated-cube Michelson interferometer which is self-stabilized, bulk longitudinal high-frequency acoustic echoes have been detected [144, 145]. Despite the recent advances in the active stabilization of the Michelson interferometer [146], it is sensitive to the low-frequency noises and vibrations. The stabilized systems and the self-stabilized configurations of the Michelson interferometer are not suitable for the use in our experiments due to the difficulties with the desired design of the interferometer that should easily allow the probe incidence angle variation.

The Fabry-Pérot interferometer [147] is usually made of two parallel surfaces to form an optical cavity that allows the passage of the optical radiation only if it is resonating within the cavity. This interferometer is often used in spectroscopy: it serves for the sensing of the gases [148, 149] and it was used as a primary tool in its simplest implementation in the early studies of the Brillouin scattering phenomenon [150, 151], while it is still largely nowadays used in Brillouin scattering experiments as said in Sec. 1.3.2, also in the case of surface phonons [152]. The Fabry-Pérot interferometer used as optical cavity has also been used later in picosecond laser ultrasonics experiments [131, 153–155]. However, this interferometer type cannot serve as a base for our experimental setup due to the high complexity of the design it would require to allow good sensitivity in a wide range of frequency together with the need of varying the angle of incidence.

Another interferometric scheme, the Fizeau interferometer, which often serves for the quality control of the optical surfaces, was demonstrated to be able to measure the low-frequency acoustic waves [156], although it needs to be at normal incidence to the tested surface. Hence, for obvious reasons (low-frequency and normal incidence), it cannot also serve as a basic setup for our purposes.

Following the use of a birefringent fiber for ultrafast signal processing (demultiplexing) in an interferometric all-optical switch [157], a common-path interferometer using a pair of calcite (birefringent) crystals has been implemented and succeeded in measuring single gold nanoparticles oscillation with a period on the order of 20 ps [158, 159]. Few years later, another group went further with this idea by proposing a common-path interferometer

allowing measurement to be done in a reflection configuration (important for opaque samples) and using a single calcite crystal [136, 160]. Although this type of interferometer does not need stabilization, as the reference and probe beams follow the same path, and has shown close to shot-noise limit [159], it does not also suit our requirements because of the difficulty to vary the angle of incidence, especially for large incidence angle.

Another type of interferometer, the Mach-Zehnder interferometer, has first been applied for the detection of the bulk and surface acoustic waves in the MHz range [161] and has been used in association with a scanning Michelson interferometer to perform phase-sensitive time-resolved interferometry with ultrashort optical pulses [162]. The first ever reported use of an interferometer for detection of bulk longitudinal acoustic echoes of high-frequency content ( $\gg 1$  GHz) made use of a Mach-Zehnder interferometer and has been proposed by Perrin et al. in 1996 [11], while investigating wave propagation in a multilayered structure made of 12 Cu/W bilayers with a period of 7.5 nm. Later, still using a stabilized Mach-Zehnder configuration, they achieved the comparison between signals obtained with reflectometric and interferometric measurements in various systems: thin films, multilayers, and particles in colloids [12]. It was also used for nondestructive testing of multilayered structures [163] and has also been proved to be able to perform in configuration with the probe incidence angle variation [164]. Consequently, this could be one of the possible options for the base of our experimental setup, yet requiring stabilization. It was therefore decided to implement a Sagnac interferometer, more suitable thanks to the common-path configuration that offers high stability and which is in general easy to use. It is now proposed to learn more about the Sagnac interferometer.

### 1.4.2 Sagnac interferometer in picosecond laser ultrasonics

As said previously, the main feature of the Sagnac interferometer is that it is a common-path interferometer. So, both reference and probing beams follow the same optical trajectory with the initial zero phase shift between two beams. For the same reason, it is self-stabilizing because the sample surface itself is used for the reference in this scheme, while, in the Michelson and Mach-Zehnder interferometers, a mirror is used for the reference (Fig. 1.19), which should hence be precisely positioned or actively stabilized for the correct functioning.

In 1999, Hurley and Wright, inspired by the use in 1991 of a modified Sagnac interferometer to measure ultrafast optical nonlinearities [165], proposed and used, for the first time, a modified Sagnac interferometer in picosecond laser ultrasonics [13]. Working at normal incidence to the sample surface, their interferometer was tested by examining the short-time thermoelastic response of a gold film in which they were able to obtain separately the relative change in reflectance amplitude and in phase induced by a fs pump pulse (Fig. 1.20). Few months later in 2000, a similar interferometer design for picosec-

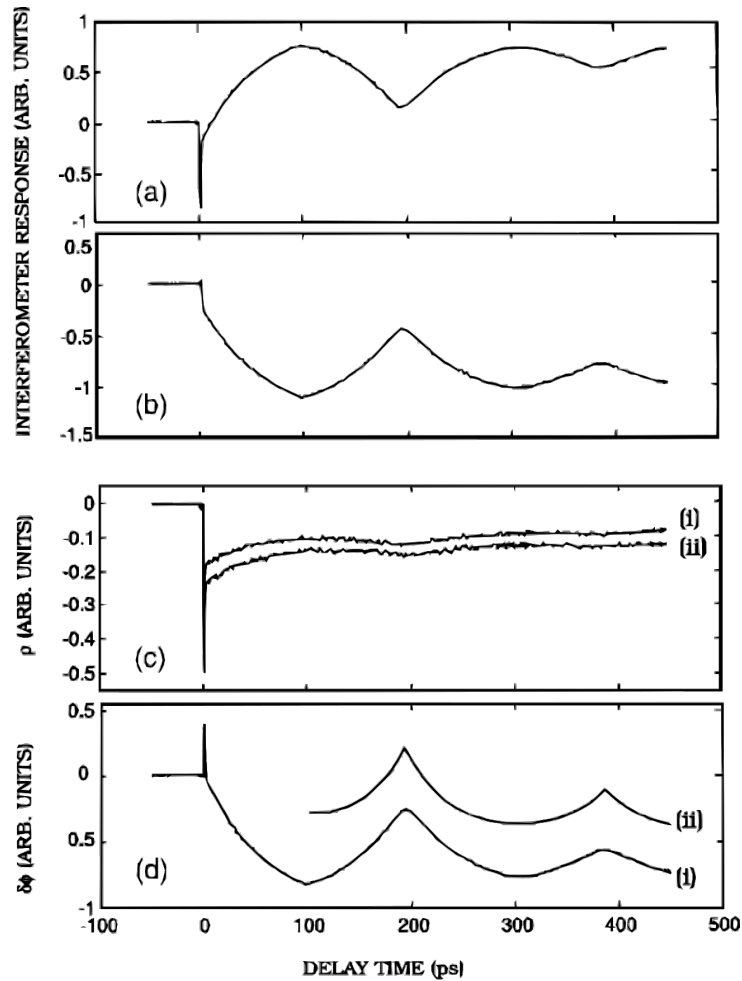


Figure 1.20 – Demonstration of the first use of the Sagnac interferometer in picosecond acoustics by Hurley et al. [13]. (a)-(b) Interferometric responses obtained with the two positions of the quarter-wave plate allowing the easiest half sum and half difference to extract the relative change in reflectance  $\rho$  and the change in phase  $\delta\phi$ : (a)  $0^\circ$  and (b)  $90^\circ$ . (c) Reflectance  $\rho$  derived from (i) the interferometric response and (ii) direct measurement. (d) Phase  $\delta\phi$  derived from (i) the interferometric response and (ii) the theoretical fit to the acoustic echoes. (reprinted from Ref. [13]).

ond ultrasonics has been proposed by Nikoonahad et al., who reported acoustic echoes detection in tungsten, aluminum and copper films [166]. The detection not only of longitudinal but of shear bulk acoustic echoes generated by mode conversion at the interface between an isotropic film and an anisotropic substrate have also been reported the same year by Hurley et al. [167], which led the same group to observe surface acoustic waves on anisotropic crystals a couple of years later [168], using a scanned objective [169] and later a 4f-system to change the pump-probe distance [170].

The use of a Sagnac interferometer, obviously not restricted to picosecond laser ultrasonics but also applied to kHz-MHz ultrasound detection such as in Refs. [171–174] to name but a few, has been widely used in different types of experiments involving GHz acoustic waves. Besides its use in the measurement of the resonances of radio-frequency

bulk or surface acoustic wave resonators [175, 176], it has also been applied for, but not restricted to, the detection of: acoustic solitons [177], acoustic attenuation in quasicrystals [178] and in vitreous silica [179], acoustic phonons of several hundreds of GHz in GaAs/AlAs superlattices [81, 180], high-frequency surface acoustic waves (up to 20 GHz) [181], scattering of 30-200 GHz acoustic phonons in strained SiGe/Si heterostructures with  $\sim 10$  nm-thick SiGe layers [182], and 5-100 GHz acoustic resonances in multilayered nanoacoustic resonators based on mesoporous SiO<sub>2</sub> thin-films [183]. Note that the previous list of applications is not meant to be complete but to demonstrate the wide use of this interferometer type in the picosecond laser ultrasonics community.

In the previously-enumerated works, although the first designs were adapted to work at normal incidence [13, 166], the configuration where the probe beams are obliquely incident to the sample surface have also been applied, either with very small value [170, 182] or with no definite value [81, 177, 178, 180, 181, 183]. Yet, this configuration has been theoretically proved to increase the information that can be obtained about the sample compared to the case of normal incidence [184]. For instance, it has been used by Matsuda et al. to measure the strain pulse shape of coherent longitudinal acoustic phonons [185, 186] (see Fig. 1.21 for the schematic of the used configuration). Note that the configuration reported in Ref. [186] has served as a basis for the Sagnac interferometer proposed in this PhD thesis and detailed in Chap. 2.

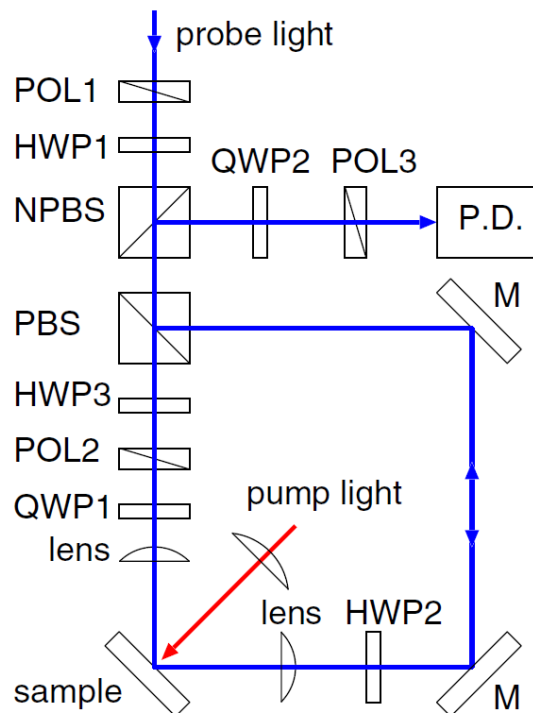


Figure 1.21 – Schematic of the Sagnac interferometer used by Matsuda et al. in Ref. [186]. In this figure: POL - polarizer, HWP - half-wave plate, NPBS - non-polarizing beam splitter, PBS - polarizing beam splitter, QWP - quarter-wave plate, M - mirror and P.D. - photodetector. (reprinted from Ref. [186]).

In all of the previously-cited works using any modified Sagnac interferometer configuration, the probing and the reference beams have opposite polarizations when recombined, such as in the path between the non-polarizing beam splitter (NPBS) and the photodetector (P.D.) in Fig. 1.21. To make them interfere, a quarter wave plate (QWP2) in combination with a polarizer (POL3) with the transmission axis aligned at  $45^\circ$  are used. The next section is devoted to explain this use, as it will also be important for the here-developped Sagnac interferometer.

### 1.4.3 On the interference of orthogonally polarized light waves

In the Sagnac interferometer of Matsuda et al. [186] (Fig. 1.21), the probe light (blue solid lines) is split by the polarizing beam splitter (PBS) into a probing path and a reference path that correspond to the clockwise and counterclockwise paths, respectively. After traveling along the path of the interferometer, they recombine on the same PBS with subsequent reflection on the non-polarizing beam splitter (NPBS) that directs a portion of the radiation to the photodetector (P.D.). Since the lights along the probing and the reference paths are orthogonally polarized waves (horizontally for the probing path and vertically for the reference one), the interference phenomena will not take place due to the first Fresnel–Arago law [187] (translated in English in Ref. [188]), except if the wave polarization planes are combined to the same state as follows from the fourth Fresnel–Arago law. In Refs. [188, 189], the four laws are stated in the exact following way (with *simplified version* in italic) and declare that:

1. « Two rays polarized in opposite planes have no appreciable action on each other, in the very same circumstances where rays of natural light would interfere so as to destroy each other (*two waves, linearly polarized with perpendicular polarizations, cannot interfere*); »
2. « Two rays polarized in one and the same plane act on or interfere with each other just as natural rays, so that the phenomena of interference in the two species of light are absolutely the same (*two waves, linearly polarized in the same plane, can interfere*); »
3. « Two rays polarized in opposite planes may be afterwards combined to the same plane of polarization, without acquiring the ability to influence on one another (*two waves, linearly polarized with perpendicular polarizations, if derived from perpendicular components of unpolarized light and subsequently brought into the same plane, cannot interfere*); »
4. « Two rays polarized in opposite planes and then combined to the similar state of polarization, interfere like natural rays, if both originate from the wave primitively polarized in the same plane (*two waves, linearly polarized with perpendicular polarizations, if derived from the same linearly polarized wave and subsequently brought*

*into the same plane, can interfere).* »

To make the reference and probe light interfere on the photodetector, it is usual to use a combination of a quarter-wave plate (QWP2 in Fig. 1.21) and a polarizer (POL3 in Fig. 1.21) just before the photodetector (P.D. in Fig. 1.21). Consider the probing  $E_{1r}$  and the reference  $E_{2r}$  electric fields, horizontally and vertically polarized, respectively. The total electric field after reflection on the NPBS and before the QWP2 can therefore be written in a vector form as:

$$\vec{E}_{tot} = \begin{pmatrix} -E_{1r} \\ E_{2r} \end{pmatrix}. \quad (1.6)$$

Using Jones matrix formalism and assuming negative sign convention, *i.e.*,  $\exp(-i\omega t)$ , it can be shown (see text and/or appendix in Refs. [13, 186]) that both probing  $E_{1r}$  and reference  $E_{2r}$  electric fields will have linearly polarized components in the same plane after the quarter-wave plate QWP2 set at  $+45^\circ$ :

$$\vec{E}_{tot}^{\text{QWP},45^\circ} = \frac{1}{\sqrt{2}} \begin{pmatrix} E_{1r} - iE_{2r} \\ -iE_{1r} + E_{2r} \end{pmatrix}, \quad (1.7)$$

where  $\vec{E}_{tot}^{\text{QWP},45^\circ}$  is the total electric field between QWP2 and POL3. Hence, the polarizer POL3 orientation allows to analyze the interference between the probing and reference lights. For example, after setting POL3 at  $0^\circ$ , the part of the field reaching the photodetector is proportional to  $(E_{1r} - iE_{2r})$ , while when POL3 is set at  $90^\circ$ , the part of the field reaching the photodetector is proportional to  $(-iE_{1r} + E_{2r})$ . The use of the two intensities measured with these two settings allows to split amplitude and phase information, as it will be discussed in more details and demonstrated in the following of the thesis manuscript, although when using another combination of orientations.

Coming to the end of the first chapter, the next and last section is dedicated to, on the one hand, summarizing the main points discussed so far, in particular the current state-of-the-art interferometric methods for picosecond laser ultrasonics and their limitations, and, on the other hand, briefly explaining what is proposed in the current work and why it will improve the state-of-the-art methods.

## 1.5 Chapter summary and thesis outlook

After a historical introduction on the discovery and first applications of the opto-acoustic and acousto-optic effects that opened the field of research nowadays known as laser ultrasonics, the basis of the field dedicated to the study and the use of picosecond acoustics have been introduced. A discussion on the subsurface imaging and depth profiling has then followed with a particular emphasis on the use of the frequency-domain and

time-domain Brillouin scattering techniques to probe transparent materials. Although the use of optical interferometry, as reviewed, has become more widespread over the years in the field of picosecond laser ultrasonics, its application to TDBS depth profiling remains untouched, despite the promising theoretical expectations available.

The basic idea behind this PhD thesis is to build an experimental setup, in order to apply for the first time ultrafast optical interferometry for the depth-profiling of materials. The main motivation of this experiment is the main advantage of the optical interferometric detection over the classical reflectometric one: the opportunity to separate the phase signal from the amplitude signal, which is impossible if the latter method is used. The foundation of this work consists of the experimental and theoretical advances of the depth-profiling and optical interferometry, discussed previously in the corresponding sections. At the stage of the initial bibliographic study, the decision was taken to base the future experimental setup on the interferometer configuration proposed by Matsuda et al. in Ref. [186]. The development of such interferometer setup was initially proposed in Ref. [13] for picosecond ultrasonics experiments. More than two decades after this initial proposition to use Sagnac-based interferometric technique in picosecond ultrasonics, we propose a new possible application: to construct an interferometer allowing precise variations of the probe incidence angle together with keeping the optical path always constant, while the sample remains motionless relatively to the pump beam. This interferometer will be used to study homogeneous samples that are transparent at the probe laser wavelength, which will demonstrate the possibility of its future use for inhomogeneous materials. The main purpose is to study, using optoacoustic techniques, how the physical properties of such materials change with respect to depth. The main advantage over previously proposed reflectometric methods of depth profiling is that the use of optical interferometry will make possible to split the changes in amplitude and in phase of the transient optical field reflectivity. This possibility should allow to reveal the best axial resolution the TDBS technique can offer, which should not be limited by the probed wavelength set by the Brillouin scattering interaction, but by the characteristic length of the acoustic pulse. There should be no limitation from the signal processing either, since the instantaneous frequency should be (theoretically) directly derivable from the measured instantaneous phase.

To achieve this exciting goal, an experimental setup based on Sagnac interferometer has been designed and constructed during this PhD thesis. As it was noted before, to get the in-depth profile of material properties, TDBS signal has to be measured at two different probe incidence angles. The solution for the precise variation of the probe incidence angle was found by combining precise rotational stages with optical fibers. The here-proposed experimental setup is now described in details in the next Chapter 2. Note that the proposed solution provides the possibility (not used in this work) to conduct the experiments in configurations with probe transmission or the experiments where pump

and probe beams are incident from opposite sides of the sample.

# EASILY ANGLE-ADJUSTABLE FIBER ULTRAFAST SAGNAC SCHEME FOR ULTRAFAST OPTICAL INTERFEROMETRY

---

The direction for the efficient Brillouin scattering of the incident light with the wavevector  $\vec{k}_i$  by the acoustic wave with the wave vector  $\vec{q}$  is defined by the momentum conservation law (see Appendix A). The magnitude of a measured signal from an acoustic wave will vary as a function of the incidence angle of the monochromatic probed light. One can see that the variation of the probe beam incidence angle gives an opportunity to study the behavior of the acoustic wave of a particular frequency in the bulk of the tested sample. In the experimental conditions, it takes a lot of time to realign all the elements in order to change the probe incidence angle, which is one of the interest in making an experimental setup that would allow varying the probe incidence angle easily.

For the adjustment of the angle of incidence of the probing light, we have decided to use the rotation mechanism (described later in Fig. 2.3) that allows changing the probe incidence angle in a very short time. Changing the angle of incidence allows adjusting the projection of the incident light wave vector when there is no possibility to vary the laser wavelength over a large range. However, the variation of the light wavelength leads to the different response of the material (caused by the dispersion in optical properties). Hence, the variation of the wavelength is not a solution for the experiments in the volume without additional experiments and treatment complications.

The methods of the depth-profiling of materials, discussed in Sec. 1.3.2, have another limitation to overcome that has not yet been mentioned but still is of great importance. This limitation is the low- and high-frequency non-oscillating components of the measured reflectivity signal. Suppressing of these two components will give the possibility to access the slowly-varying amplitude and frequency of the Brillouin oscillations, that contain the information on the material spatial inhomogeneities [17]. From the theoretical advances in Ref. [17], we can conclude that, for the separate measurement of the slowly-varying amplitude and phase of the Brillouin oscillations, we need to introduce the ultrafast optical interferometry, but for the additional suppression of the unwanted components we need to have the possibility to vary the angle of incidence and polarization of the probe beam.

The configuration proposed by the authors of Ref. [170] is an example of the Sagnac

interferometer applications, where the interferometric methods have been successfully applied for the detection of the surface and bulk acoustic waves.

## 2.1 Presentation of the chosen configuration of the experimental setup

Among 8 possible configurations of the experimental setup that have been designed, the most suitable configuration (C7, Figs. 2.1 and 2.2) has been chosen after discussions. The special feature of the constructed Sagnac interferometer is the use of the optical fibers which grants the possibility to vary the probe incidence angle  $\theta_i$  with optical path always remaining constant. Combination of two precise mechanical rotation stages grants the change of the probe incidence angle without changing the position and orientation of the sample and the optical elements of the pump path, while 2 linear translation stages underneath the rotation mechanism allow the coarse displacement of both sample and probe line relative to the pump beam. The scheme of the developed experimental setup, shown in Fig. 2.1, represents the version of the experimental setup before the first installation, while Fig. 2.2 shows the latest configuration which was built to correct the inconveniences and drawbacks discovered during the exploitation of the setup. The explanation of the experimental setup is given below.

In the experimental setup (Fig. 2.2), a laser with 810 nm output wavelength is used, with the repetition rate of 80 MHz and 150 fs pulse duration. The pump beam with 405 nm wavelength, obtained with the frequency doubling BBO crystal, is modulated by the acousto-optical modulator (AOM) for the synchronous detection with the lock-in amplifier SR844. After the AOM, the beam passes the delay line (see Fig. 2.2) and is sent to the sample through a 4f system, which allows the pump spot position to be moved on the sample surface.

The probe beam comes to the polarizer POL1. Further, this beam goes to the half-wave plate HWP1, the role of which is to control the power distribution by the polarizing beam-splitter (PBS). Note that for a transient reflectivity measurement, it is necessary to supply all the probe power to the clockwise direction, while for an interferometric configuration, it should be divided into two equal parts. We are using differential photodetector to reduce the influence of noises accumulated by the probe such as laser power fluctuations and vibrations of the mechanical components of the setup. A part of the light is reflected by the non-polarizing beam-splitter (NPBS) and directed onto one of the sensitive areas of the photodetector (–) for the suppression of the noises influencing all the system equally while the second sensitive area (+) serves for the detection of the signal containing the useful information.

Using Fig. 2.1, let us first talk about the setup configuration for transient reflectivity

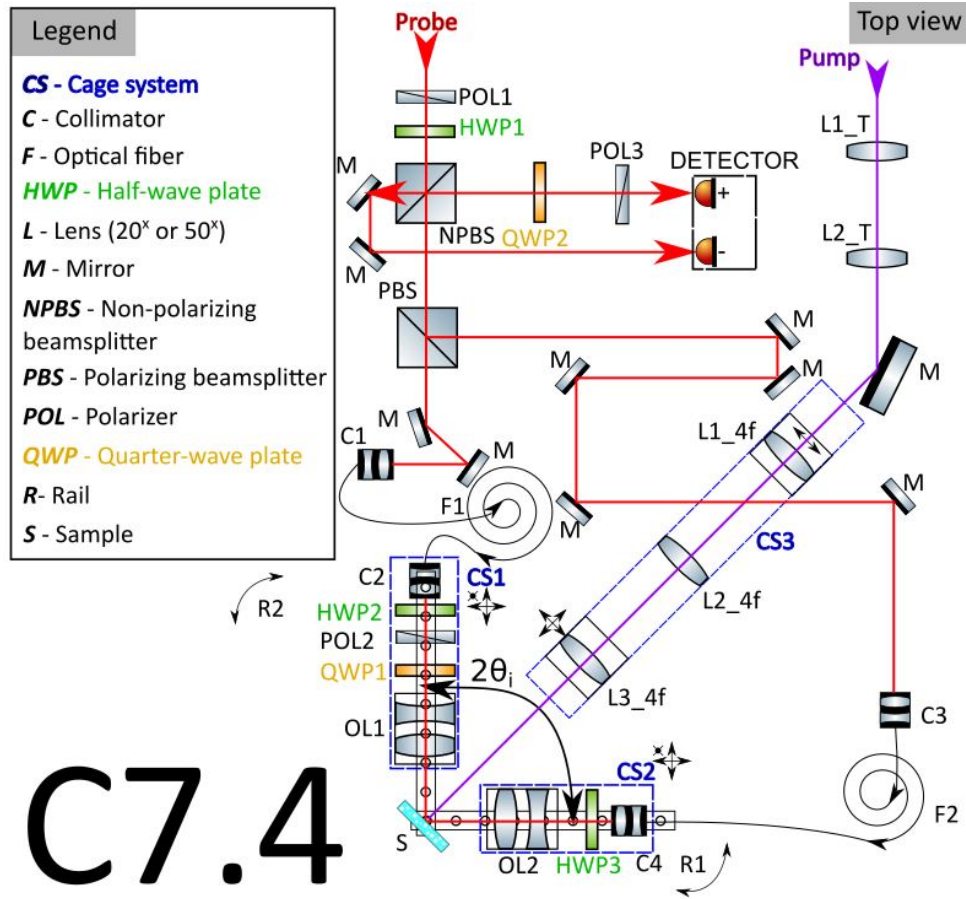


Figure 2.1 – Configuration 7 (version 4) of the experimental setup, the design of which became the end of the designing stage and marked the beginning of the way to the complete construction, preceded by the choice and comparison of the components for the construction. Centers of rotation of both interferometer arms coincide thanks to the special construction of the mechanism. Good alignment of each element of the on-rail parts of the optical common path for the probing and reference parts of the probe beam allows to make both probing and reference focal spots to remain in the same position after the change of the incidence angle, where both arms turn the same angle but in the opposite directions (clockwise and counterclockwise or vice versa).

measurements, where the first and second quarter-wave plates (QWP1 and QWP2), and POL2 are excluded due to their affiliation to the interferometer configuration. After the passage of the PBS in the clockwise direction, the light is directed by the mirrors into the fiber collimator C3 that introduces the light into the single-mode polarization-maintaining optical fiber F2 (see Appendix C for details about this alignment). The light beam coming out of the fiber F2 is collimated by C4 and focused with the objective lens OL2 onto the sample surface.

HWP2 and HWP3 allow free choice of the light polarization incident on a sample, the possibility to add QWPs reveals additional possibilities, as discussed in Ref. [186]. For the sake of the discussion, it is assumed now that HWP2 and HWP3 are set so that they rotate the horizontal polarization to vertical one, and vice versa.

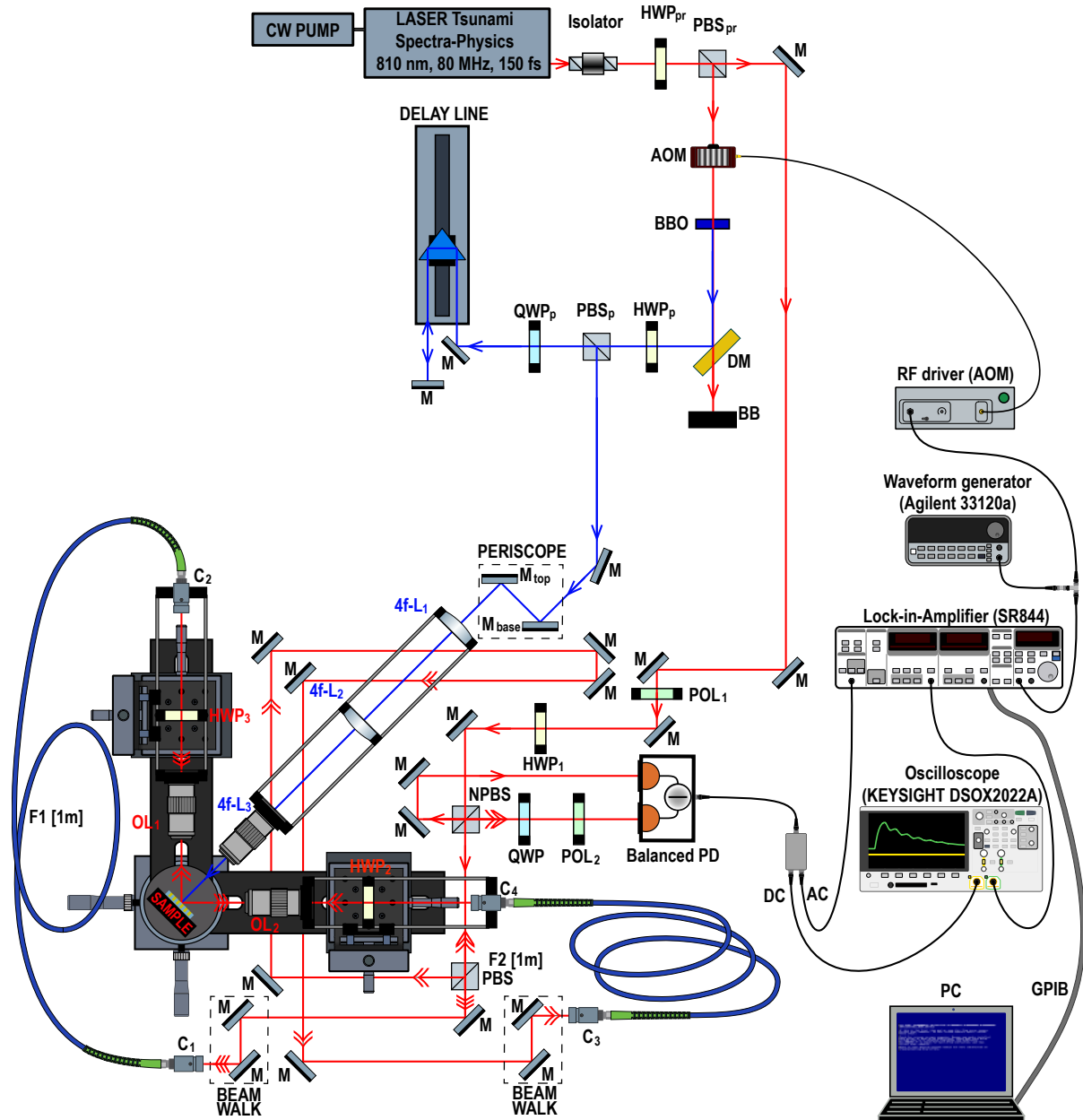


Figure 2.2 – The configuration C7.5 of the experimental setup, that includes all the components arranged in the latest configuration minimizing the inconveniences and drawbacks discovered during the exploitation of the setup.

The beam, transmitted through the fiber F1 and collimated by the fiber collimator C1, goes after through the PBS and then supplied to the sensitive area (+) of the photodetector. Here (in the reflectometric regime without the QWPs and POL2), POL3 is set for passing of the horizontally polarized light but since it comes already in this state after PBS, it could have been also removed. Yet, we keep it to be sure that no light going in the counterclockwise direction, as well as the light reflected from the PBS backwards before entering the circular part of the system, will reach the photodetector. The result of this measurement is the transient reflectivity signal. We can also vary the probe incidence angle by the rotation mechanism (described later in Fig. 2.3).

For this setup to operate in the interferometric regime, we need two coherent waves, one of which is reflected from the reference surface and another reflected from the surface of the interest (as it is demonstrated in Chapter 1 with an example of the Michelson interferometer, Fig. 1.19). Both waves, after the reflection from two surfaces, interfere and produce the interference pattern that reveals the information on the difference of the sample surface from the etalon (reference) surface. As was noted before, in this experimental setup, sample surface serves also as a reference. Electric fields for both reflected waves,  $E_{1r}$  (probing light) and  $E_{2r}$  (reference light) are:

$$E_{1r}(t, z) = E_1 r_0 e^{i\varphi_0} \left(1 + \rho(t) e^{i\delta\phi(t)}\right) e^{i(k_{op}z - \omega t)}, \quad (2.1)$$

$$E_{2r}(t, z) = E_2 r_0 e^{i\varphi_0} e^{i(k_{op}z - \omega t)}, \quad (2.2)$$

where  $E_1$  and  $E_2$  stand for the electric field amplitudes,  $k_{op}$  and  $\omega$  are the optical wavenumber and angular frequency, respectively, and  $z$  the propagation direction of each electromagnetic plane wave in its own frame, which collapse to the same one after the last reflection on NPBS.  $r_0 e^{i\varphi_0}$  stands for the complex optical electric field reflection on the unperturbed sample and  $\rho(t)$  and  $\delta\phi(t)$  are the relative changes, as a function of the pump-probe time delay  $t$ , in amplitude and phase of the reflected electric field introduced by the pump pulse. It has to be noted that we assume  $\rho(t) \ll 1 \forall t$ , while  $\delta\phi(t)$  in the case of opaque material is also  $\ll 1$  but not in the case of transparent material.

In the very beginning of the experiment, we need to set the HWP1 so that the laser beam coming to the PBS is split into 2 equal parts:  $E_1 = E_2$ . The beam that goes in the clockwise direction (probing light) has 1.2 m of additional optical path in comparison with the beam propagating in the counterclockwise direction (reference light). This results in 4 ns delayed arrival of the probing beam relative to the arrival of the reference beam at the detector channel +.

For our measurements we are using the pulsed laser with 80 MHz repetition rate, so the interval between the arrival of the laser pulses is 12.5 ns between each excitation of the sample. The reference pulse (counterclockwise) arrives to the sample surface 4 ns before the arrival of the probing pulse. Reflected by the non-excited sample surface, this pulse then follows to the photodetector. As was noted before, in order to reach it, HWP3 (or HWP2) is set to turn its polarization to the vertical polarization so it could pass through the optical system C4-F2-C3 and reflect on the PBS. The probing pulse, that reaches the sample surface with 4 ns delay (relative to the reference pulse) due to the 1.2 m longer optical path created by the additional mirrors, follows the same optical path as the reference, but in the opposite direction. We use HWP3 (or HWP2) for the orientation of the polarization plane for this second beam to go through the optical system C2-F1-C1 and PBS (all of them require horizontal orientation of the polarization plane for the efficient transmission). To be able to see the moment of the sample excitation by the

pump pulse, the probing pulse can arrive for the first time to the sample surface several tens of picoseconds before the arrival of the pump pulse, allowing thus the study of the whole process of excitation when its arrival is continuously delayed. This measurement of the signal several picoseconds before the pump pulse arrival also allows to have a measure of the possible balance mismatch between the + and – channel of the balanced photodetector.

Thanks to the delay line we make both, reference and probing, pulses to come with the temporal shift relatively to the arrival of the pump. The sample reflectivity is measured for each position of the delay line. Basically, we have the pump beam that excites the acoustic wave which is detected by the probe beam, each pulse of which comes to the sample surface with the temporal increment defined by the speed of the delay line. Each time of this delay line scan, the probe beam is reflected by the acoustic pulse propagating either in the bulk or along the surface of the sample.

If the experiment is conducted as described in the paragraph above, orienting the POL3 horizontally for the transmission of the probing beam only will result in the measurement of the transient reflectivity signal due to the fact that the reference light will not be transmitted by the polarizer. To make them interfere and to get desirable interferometric signal, we need to install QWP2. In that case, the choice is made to set the orientation of POL3 to  $45^\circ$  and QWP2 orientation is whether horizontal ( $0^\circ$ ) or vertical ( $90^\circ$ ). In the former case, a  $\frac{\pi}{2}$  retardation is introduced to the vertical component of the electromagnetic field, while in the latter case a  $\frac{\pi}{2}$  retardation is introduced to the horizontal one. In both cases, the two components in phase quadrature are then set to interfere thanks to the  $45^\circ$  orientation of POL3, since both components of the total electric field after the polarizer are equal to the half-sum of the horizontal and vertical components before it (see Appendix B for the Jones calculus and Chap. 3 for theoretical analyses of the interferometric signals).

After the choice of the most suitable configuration of the experimental setup, I have started the search of necessary equipment for the construction of the setup. The most challenging part was the design of the rotational mechanism, that allows turning the interferometer arms precisely around the sample that should not move. In cooperation with the engineers from Newport custom solutions for motion control department, we have developed such a mechanism (Fig. 2.3). The rest of the equipment was bought mostly at Newport, Thorlabs, Edmund Optics, some parts were bought at WATEC and Miss Numerique.

The chosen solution to perform the specific feature of the developed interferometer, *i.e.*, the possibility to easily vary the probe incidence angle, is now presented.

## 2.2 Mechanical solution for the probe incidence angle variation

The key feature of this experimental setup is the ability to vary the probe beam incidence angle. For the interferometer to work correctly, two important issues have been solved during the conception and alignment stages:

1. The optical path during the rotation should not be changed. In order to solve this problem, the choice was made to use optical fibers fixed on rails with other optics that stand between the optical fiber outputs and the sample (see the cage systems CS1 and CS2 in Fig 2.1).
2. The rotation of arms should not displace the laser beams, meaning that the focusing of both laser beams has to be precisely aligned to coincide with the center of the rotation of the rotating mechanism.

Resolving these two problems allowed to construct the experimental setup with manual rotation that ensures the possibility to change the probe incidence angle within minutes. It could be possible to make the experimental setup with motorized rotating stages allowing to make the angular scanning process fully automatical, but the cost of this solution exceeded the budget.

The solution for the rotation mechanism was neither easy nor straightforward. For the manual solution, the decision was taken to combine two similar rotating stages in on-top configuration. The required rotating stage needed to fulfill the following parameters:

- angular step of  $0.1^\circ$ ;
- the possibilities of fine and coarse adjustments of the angle as well as the ability to lock the chosen angle from the unintended rotation;
- two independent rotating stages, centered with the  $0.1 \mu\text{m}$  precision;
- high off-axial load capability for each stage to hold the interferometer arms opto-mechanical sub-systems;
- high on-axial load capability for the sample with its holder and a multiaxis (X-Y-Z-tilt-yaw) stage that allows fine adjustments of the sample position.

The catalogues of the available products allowed to find such stages with reasonable price (M-UTR120A, Newport). For their precise ( $0.1 \mu\text{m}$  precision) centering, a custom solution was needed. The idea to use a rod for the centering of both rotation stages was proposed by Newport Custom Solutions department and I have proposed to extend this rod so that the sample position does not depend on the rotation of any of the stages. The final configuration of the rotation mechanism is presented in Fig. 2.3. The cut view (up left) allows seeing the mechanical piece (in grey) ensuring the precise alignment of the center of rotation of the two rotation stages. In the 3D view of the assembly (right), the top surface of the alignment mechanism, labeled by 7, is used for fixing the sample

holder.

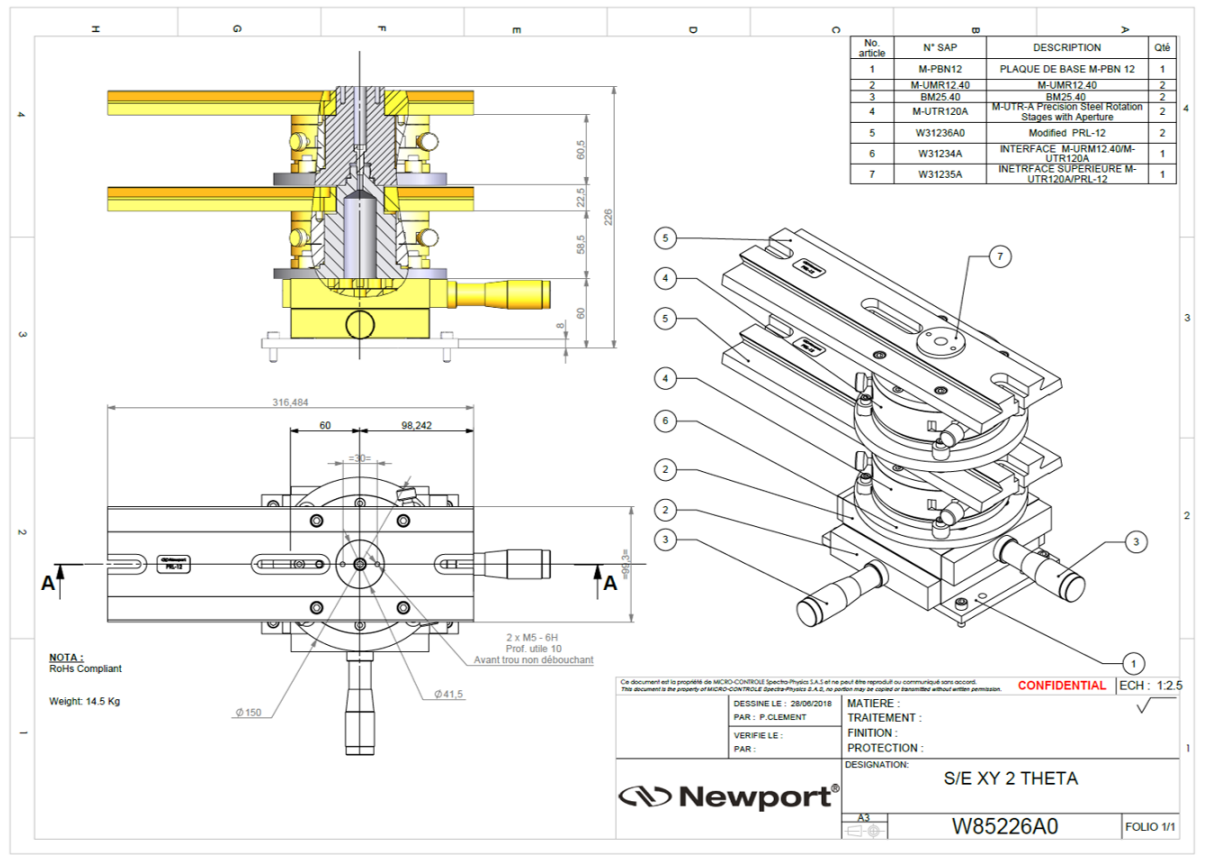


Figure 2.3 – Rotation mechanism for the precise and fast control of the probe incidence angle.

Note that other solutions proposed by different opto-mechanical vendors did not fulfill the demands and were rejected at the end.

In each of the rotation stages, the 100 mm dovetail optical rails (5 in Fig. 2.3 were installed for the further mounting of the opto-mechanical sub-systems. The thick rails were chosen for the higher stability of the experimental setup, since the rotation stage allowed high off-axial load.

## 2.3 System for the pump beam on-sample positioning

To allow 2D imaging of the sample surface, which could also provide 3D imaging in transparent material thanks to the TDBS technique, a scanning system allowing the relative movement of the generation and detection positions on the sample surface is needed. The priority at the moment is the development of depth-profiling methods using interferometry, while the scanning system is envisaged as a later up-grade of this experimental setup.

In the case of our experimental setup, three options are possible to move the generation relatively to the detection. The easiest way is to perform a 1D scanning of the pump beam horizontally over the sample surface, which is achieved in our case thanks to a translation movement of the complete rotation mechanism that contains, at its base, two linear translation stages (see Fig. 2.3) meant to move it, and hence move the sample, with fixed detection position on its surface, relatively to the pump. This pump beam on-sample displacement is realized without the unnecessary perturbations of the optical paths of both pump and probe. Since these translation stages are not equipped for the fine adjustment and limit the displacement only in the horizontal plane, two more solutions were thought. A method using a 4-f system allowing to move the pump spot position in two dimensions covering the sample surface is currently used in the experimental setup, because of its simplicity and flexibility, and is shortly described below. Another method, combining this 4-f system with a two-dimensional scanning system moving the sample itself, could allow, with a precise calibration of the 4-f system, to maintain the pump spot position on the sample surface while moving the probe position away, without any movement of the (heavy) interferometer arms. Although doable, this last option requires very careful alignment and calibration steps and would be better to handle in use with motorized stages. The easiest options where the pump spot position only is moving have been preferred in this work, and should be preferred as long as the elastodynamic reciprocity principle applies to the tested sample.

In more details, a 4-f system is an optical system that consists of 2 identical lenses (L1 and L2) and a microscope objective (L3). The lenses L1 and L3 are spaced from the L2 lens by the  $2f$  distance as it can be seen in Fig. 2.4. In order to shift the laser beam on the sample surface, the first lens in the system has to be moved along the axis perpendicular to the optical axis. The displacement of the lens L1 for a known distance  $\Delta y_{L_1}$  will make the focused by the last lens laser beam to move for some distance  $\Delta y_s$ , which can be measured experimentally and hence calibrated. Precise displacement of the pump beam is crucial for the studies of the SAW propagation. In this work, decision was taken to use a lens mount for L1 which is not precise enough for conducting such calibration, yet allowing to achieve pump and probe superposition accurately enough for depth-profiling experiments.

## 2.4 Installation, alignment and fine adjustments

One of the ideas of this setup was to make it transportable and compact, so almost all the elements are installed on the  $600 \times 600 \times 12.5 \text{ mm}^3$  breadboard. The process of installation and alignment took some time but the most challenging parts were fine adjustments where the precision plays a dramatic role. Three problems have been met and subsequently overcome.

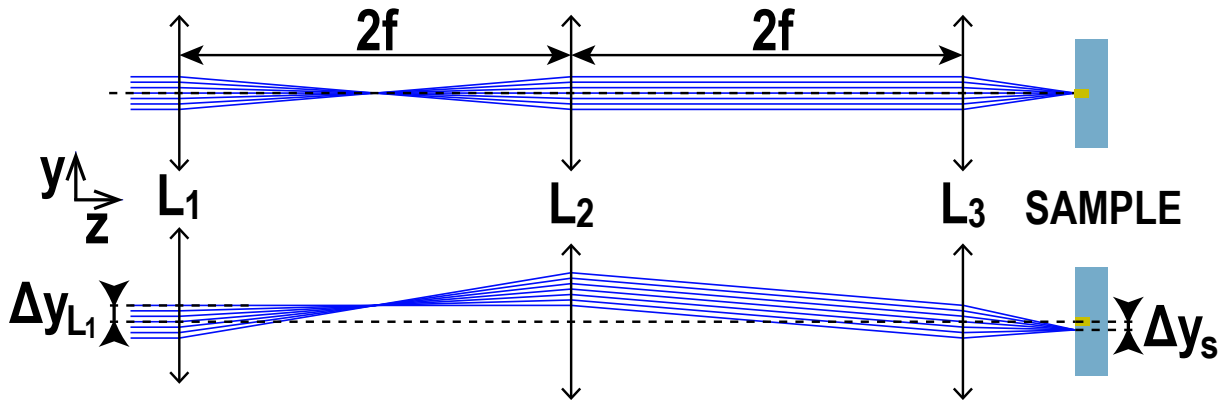


Figure 2.4 – An opto-mechanical system that moves the pump beam over the sample surface.

The first issue concerned the light insertion into the polarization-maintaining single-mode optical fiber. After testing two more or less efficient methods, I have decided to buy a 4-axis (x, y, tilt, yaw) stage (see the right bottom corner of Fig. 2.5). The easiest solution was indeed to put the fiber with the connected collimator (important to pay attention to the connectors type and to the possibility to vary the collimator focal distance) onto this type of stage and to use beam walk method (the beam position is adjusted sequence by sequence along all the axis in order to get the highest possible transmission).

The second issue was that it was important for both beams to be aligned in such a way that their focal spots will not be shifted during the change of the probe incidence angle. The solution was to lock all the elements from C2 to OL1 (Fig. 2.1) in the cage system (CS, in this particular case - CS1) and put them onto the XYZ stage (see the three mounted linear translation stages in the middle of Fig. 2.5), which is situated on the top of the rail that is connected to the rotational mechanism (same for elements from C4 to OL2 in CS2). The micrometer-precise displacement of the CS along the axis perpendicular to the probe beam and parallel to the optical table allows aligning these stages in the desired way, in our case to direct the laser beams into the center of rotation.

Last but not least, the sample position along the axis parallel to the table surface and perpendicular to the pump beam is less important in one-point measurements, but in future, we would like to apply 2D surface imaging. For that purpose, a multi-axis stage (x, y, tilt, yaw) have been installed to fix the sample holder (see the sample at the top of the optical post in front of the objectives and the multi-axis stage just below it in the left of Fig. 2.5).

Of course, it is also clear that the accuracy of installation and alignment of wave plates, polarizers and polarizing beam splitters plays the key role in the functioning of the interferometer. Hence, it should be given the highest priority.

It is important and useful to present in more details the optical fiber alignment and the installation of the polarization optics for the sake of an easy reproduction of this

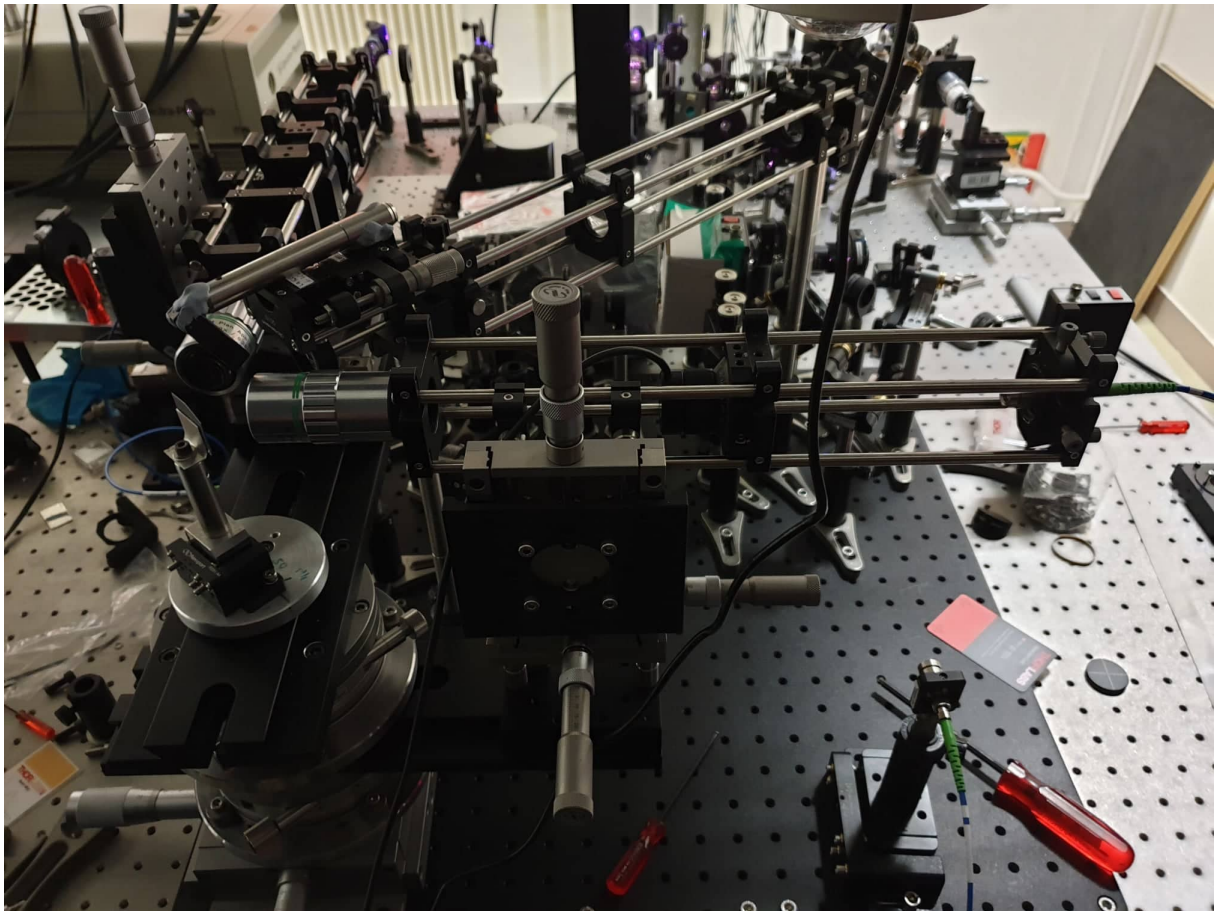


Figure 2.5 – The experimental setup in the ready-to-work state. In the left part, two objectives focus the light on the sample surface and, after the reflection, collimate it for the further transmission to the detector. The collimator with the connected optical fiber on the top of the multi-axis stage is in the right bottom corner of the figure.

interferometer in the future.

### 2.4.1 Optical fiber alignment

The introduction of the optical fibers into the experimental setup allowed to make the probe incidence angle variation easy, fast and without any perturbation of the optical path. The polarization of the light in the optical system plays crucial role in this work, so the choice was done to use the polarization-maintaining (PM) single-mode fibers (SMF). These PM fibers allow to maintain the polarization state of light between two points with no significant change to the initial polarization state. This is possible due to the introduced mechanical stress that creates the birefringence of the fiber. The stress may be introduced by the rods that are inside the fiber, as in the fibers with bow-tie or panda profile. Another way to introduce birefringence is directly to make the fiber asymmetric as it is done in the elliptic fiber profile. Fig. 2.6 shows these 3 types of the PM fibers along with a non-PM single-mode SM fiber (top left).

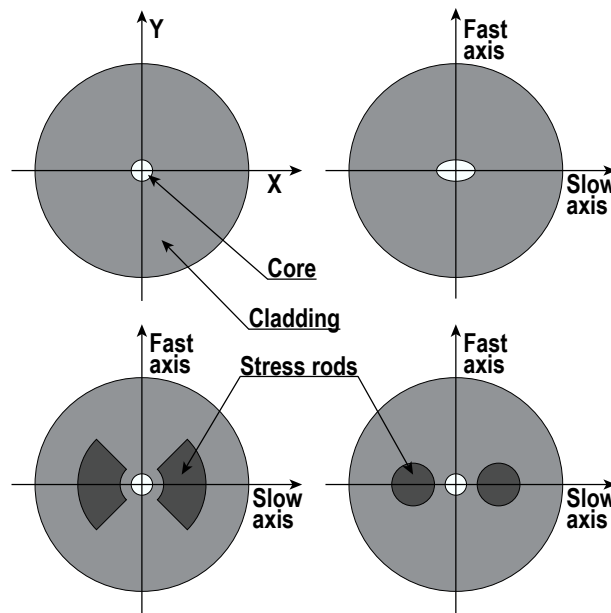


Figure 2.6 – Schematic of SMF: non-PM (top left), PM with elliptical core (top right), Bow-Tie (bottom left), PANDA (bottom right).

We have decided to choose the PANDA type optical fiber with the FC/APC connection type in order to be able to connect the collimators for the light insertion and collimation at the fiber input and output, respectively (FC and APC stand for Fiber Connector and Angle Polished Contact, respectively). The choice of the connection type plays important role since the FC/PC fibers require normal incidence of the laser beam for the effective light insertion. Use of the FC/APC connection type is preferable in schemes like the one in this work since in other case the light reflected by the fiber inner and outer surfaces will follow exactly the same optical path leading to unwanted light on the photodetector

and inside the laser cavity. Using the FC/APC connectors allows to remove this problem thanks to the angular polishing at  $8^\circ$  of the fiber end. The light incidence angle is  $11^\circ 40'$  with respect to the optical axis of the fiber is needed to take the refraction into account for the efficient light insertion into the fiber [190].

For the light insertion into the fiber, the beam walk method was used. It is an iterative procedure of linear beam shift and angular compensation of the laser beam shift (or vice versa) on the target surface to achieve wanted beam position and in the same time for the beam to fall on the surface with the desired angle. Currently, two mirrors could be used for the beam linear and angular displacement along X, Y,  $\theta_x$  and  $\theta_y$  (XY is the plane that contains the lens of the fiber collimator, perpendicular to the incident laser beam). Here, the main goal is to insert the light inside the optical fiber by directing the laser beam on the fiber collimator lens. In our case, modification of this method was initially employed, where the fiber collimator was set on top of the multi-axis stage with variable X, Y,  $\theta_x$  and  $\theta_y$  (see Fig. 2.5). Due to the constant drift of the stage, the realignment was required before every experimental session, which is no longer the case if a pair of mirrors is used.

Let us talk about the beam walk method in details, since this is the technique for the light-to-fiber coupling.

Consider a basic case, where two mirrors are used to reflect the laser beam into the collimator of the optical fiber (see Fig. 2.7). The collimator and the fiber in this case are perfectly matched before the beam walk method implementation begins, which means the following:

- the optical fiber and the collimator have the same connection type;
- fiber and collimator are chosen to operate at the same wavelength;
- the laser beam size is equal to the value written in the collimator specifications;
- for the PM fiber, the input light is polarized along the fast or slow axis (see Fig. 2.6).

Both fibers in our setup are transmitting the polarized light oriented along the fast axes. Failing to align the polarization of light along one of the main axes of the optical fiber can lead to the deterioration or loss of the fiber's main property of maintaining polarization.

In order for the operation to be simple and fast, the required components for the light insertion into the fiber and its collimation at the fiber output are as follows (the actual models of the components used in this work are given in the brackets):

- laser (Tsunami 3960C-15HP by Spectra-Physics);
- 2 mirrors in kinematic mirror mounts with the possibility to adjust  $\theta_x$  and  $\theta_y$ , *i.e.*, yaw and tilt angles in Fig. 2.7;
- fiber collimator for the light-to-fiber coupling insertion (F-H5-NIR-APC with adjustable focus);
- optical fiber (PM single mode cable, FC/APC patched, 1m long, P3-780PM-FC-1);
- alignment visualization comprising a camera (WAT-902B, Watec), with a Nikon

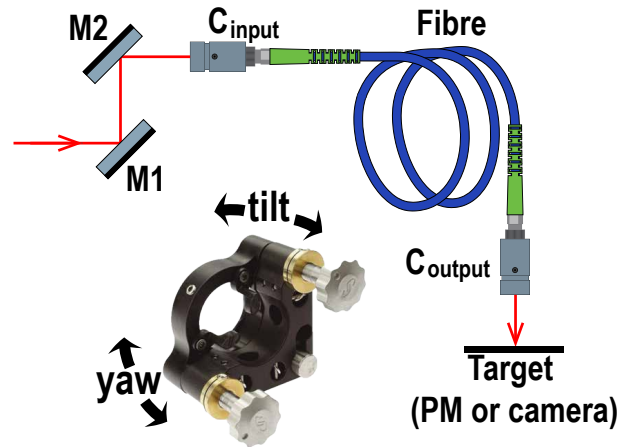


Figure 2.7 – Schematic of the configuration that was used for the light insertion in optical fiber with the beam walk method.

AF-S Micro NIKKOR 60 mm f/2.8G ED objective (C-mount adapter to fit the camera with the possibility to manually adjust Iris is required) connected to a screen via BNC/RCA or RCA/RCA cable);

- power meter (PM100D console with S121C sensor, Thorlabs).

After installation of the necessary equipment on the optical table, there are few preparation steps that have to be done. The first step is to deliver the laser beam to the center of the input collimator and to measure the power at the input with help of a power meter (PM) and afterwards to place the PM in a position where it blocks the possible beam of light exiting the output collimator, as is it shown in Fig. 2.7. If the power at the output is around 60-90% compared to the input power, then it is necessary to check if there is no other light source, that hits the PM, and if this is not the case - the beam walk method still can be used to ameliorate this result. In more realistic case, the PM shows a weak light transmission or an absence of light. Replacement of the PM with a camera was a good option in our configuration, since camera was capable to register the light that was too weak for the PM to sense its presence. If the light cannot be observed with a camera as well, it is necessary to try changing its position, focusing and the observation angle. If there is no signs of the light transmission, then a gradual increase of the input power can help (with respect to the damage threshold of the fiber). If after following all the above-mentioned steps there is no light transmission, a sequential adjustment with every of the 4 screws of M1 and M2 mirrors - 2 vertical adjustment screws (VAS) and 2 horizontal adjustment screws (HAS), meaning that each screw is slightly rotated clockwise (CW) and counterclockwise (CCW) with return to the initial position after both moves. When the transmitted light is finally observed, it is necessary to start the beam walk in order to improve the result:

1. Starting with the HAS of the M1, maximize the power of the transmitted light with all the HAS and VAS of both mirrors by turning them in CW or CCW direction - depending on what direction leads to the power going up. The camera is replaced with a PM when the PM is sensitive enough.
2. Turn the HAS of the M1 in CW direction. If the power is decreasing - change the direction to the CCW. After reaching the maximum of the transmitted power - continue to turn the screw in the same direction until the power is dropped by 50% from maximum. Note both maximum and the intentionally decreased power values.
3. Turn the HAS of the M2 in CW direction. The decreasing power indicates that the direction has to be changed to CCW. After reaching the maximum - compare the power to the maximum achieved at previous step.
4. If the power is higher - repeat steps 2 and 3 until the maximum power at step 3 is lower than it was at step 2. Turn the HAS of M2 in CW direction until the power reaches the value obtained at the end of the step 2. Turn the HAS of the M1 in CW direction until the previously achieved maximum is reached. Return to the steps 2, decrease the amount of the power drop and move to the step 3.
5. Repeat steps 2, 3 and 4 until the maximum achievable power is reached. This can be understood when a small power drop achieved by turning the HAS of the M1 in CW or CCW direction at step 2 cannot be compensated by turning the HAS of the M2.
6. Perform the steps 2-5 with the VAS of both mirrors.
7. Repeat to perform the steps 2-5 for HAS and VAS interchangeably, until the maximum is achieved for both.
8. If the adjustable collimator is used - adjust its position by a small increment of its position and repeat the beam walk procedure starting from the step 1. Continue the collimator adjustment until reaching the maximum light-to-fiber coupling.

### 2.4.2 Polarization optics installation

The constructed interferometer operation is based on the use of multiple optical components that alter the polarization state of light: polarizers and wave retarders (wave plates). One can describe a linear polarizer as an optical element that is capable of filtering the light polarization in such a way that the output light is linearly polarized for any polarization of the incident light except for the case where the polarization of the incident light is perpendicular to the transmission axis of the polarizer. Ideally, in the latter case, the light does not pass at all, while, if the incident light polarization is oriented along the transmission axis, it has to be transmitted entirely. But in the case of a real polarizer,

the output light will be attenuated by an optically dense medium for any polarization of the incident light and there will be still some light passing through the polarizer even in the case where the polarization is perpendicular to the transmission axis. The function of wave plates, on the other hand, is to introduce a certain delay between the orthogonal components of the electric field, depending on how the wave passes through the wave plates.

Polarization optics, such as wave plates, polarizers, and polarizing beam splitters, requires attention during installation and use. The appearance of the retardation errors is inevitable due to the fluctuations of power and wavelength of a laser, room temperature variations or a human-factor error during the installation and alignment processes.

Correct estimation of the retardation errors can serve for the compensation of these errors. Consider a case where the wavelength of the laser is slightly different from the one for which the wave plate is designed. The estimation of the error in retardance between two waves can be done by using the data from Fig. 2.8 as a function of wavelength. Knowing the difference between the laser central wavelength and the wavelength for which the wave plate is designed, the compensation is possible in case of a minor error. The process is based on the wave plate tilting with respect to its fast or slow axis or by rotating the wave plate. The result of the compensation is controlled with help of the polarizer, by measuring the transmitted light extinction at two perpendicular polarizer orientations.

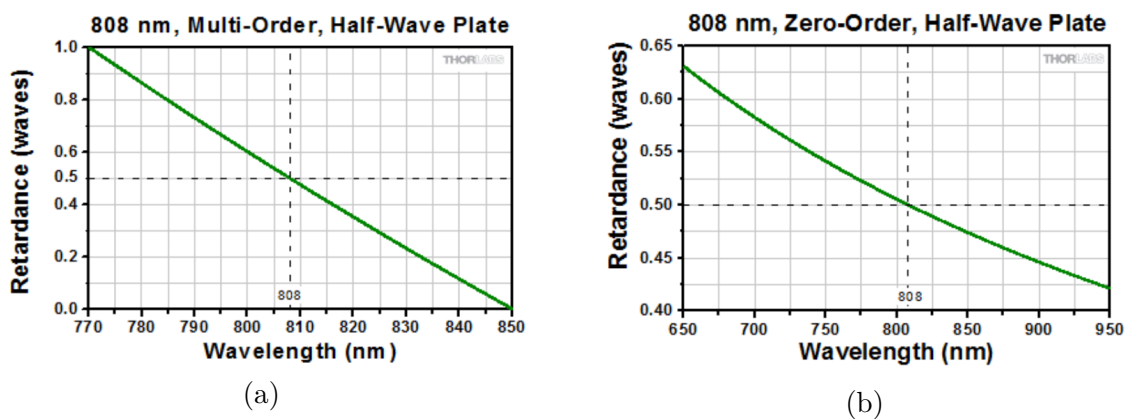


Figure 2.8 – Retardance of a multiorder (a) and zero-order (b) half-wave plates as a function of wavelength. The nature of a zero-order wave plate (b) allows for the small errors to be tolerated while the same error will result in cumulative error based on how many  $\lambda$ -orders is the total wave plate thickness. The central wavelength shift from 808 nm to 800 nm will result in change of the retardance from the initial value of  $0.5\lambda$  to  $0.5053\lambda$  in case of zero-order wave plate and for the multi-order wave plate the change is much more significant:  $0.6011\lambda$  (reprinted from [Thorlabs](#) website).

## 2.5 Detection

One of the most important elements of an experimental setup is the detector, as it helps to detect certain phenomena and therefore draw definite conclusions from them. This experimental setup uses 2 optical radiation detectors: the laser viewing card VRC5 (Fig. 2.9a) and the large area balanced photoreceiver 2307 (Fig. 2.9b). They serve different purposes, have major differences in design, but are both critical at one time or another. Even before the IR laser beam is first redirected, there is a need to see the laser beam, as the human eye is only sensitive to the visible part of the spectrum. During the installation phase, the missing VRC5 makes it very dangerous not only for the operator, but also for everyone in the vicinity since this powerful invisible beam of light, coming from a laser, can become visible in a short time by igniting surrounding elements (the flame is already visible in the visible spectrum) or can burn (eye or skin) or even blind someone in a much shorter time than a fraction of a second. In an even worse safety situation, this laser beam can also injure someone passing outside a window or through a door left open for ventilation, as well as someone who decides to look in whilst ignoring warnings, prohibitions or missing danger warnings. The installation of 2307 is only required at the very last moment of assembly, in order to fix it in a certain spot.



Figure 2.9 – Two types of the detectors: a laser viewing card VRC5 (a) allows to see the position of the laser beam, hence is critical during the alignment stage (reprinted from [Thorlabs](#) website) and a large area balanced photoreceiver 2307 (b) whose role is to detect the changes in the probing radiation resulting from the action of the pump light on the sample (reprinted from [Newport](#) website)

The preceding paragraph is written to remind you that even such an important device as a detector does not make much sense if you will not be able to see its result. It is for this reason that it is always important to observe safety precautions when working with

a device such as a laser and that, at first glance, simple things like a viewing card VRC5 can prevent non-recoverable damage.

The 2307 photoreceiver is used in this work to detect variations in laser beam intensity caused by acoustic waves which were excited by the pump beam. An additional function of this light-sensitive element is to prevent noise generated in the laser from entering the output signal through the presence of two light-sensitive areas, one of which is receiving the useful signal while the other one is receiving the light directly from the laser.

As an electronic device, the photoreceiver introduces additional noise to the signal, which unfortunately cannot be eliminated due to the very nature of electronics. It is worth considering thermal noise, that results from the random motion of heat carriers during non-zero temperature operation, and Schottky noise, that is caused by chaotic fluctuations due to the quantum nature of electrons and photons inside electronics and when they hit the light-sensitive areas, respectively.

## 2.6 First test of the experimental setup in the transient reflectivity configuration

In order to test the experimental setup and check that it was allowing to obtain some picosecond acoustic signals, it was decided to conduct the first measurement in the transient reflectivity configuration. The setup was therefore transformed into the one suitable for this type of measurements by removing QWP1, QWP2 and POL2 (Fig. 2.1) and by directing all the probe power to the clockwise direction of the pump beam propagation by the rotation of HWP1. The two objective lenses needed on the probe path were the same objective lens with a 20X magnification from Mitutuyo with the reference M Plan Apo SL 20X (with a numerical aperture [NA] of 0.28), where SL stands for super long working distance (30.5 mm). The pump was focused using a lens of focal length 100 mm. After obtaining the first results, the data treatment program has been written so the graphs of this report are made with this program.

The first test was conducted on an aluminum (Al) sample where the thermal signal has been captured (Fig. 2.10). A fast heating and slow cooling of the material can be noticed.

In order to see the Brillouin oscillations, we have chosen a piece of a (111)-cut GaAs wafer as a sample. For the measurement, the angle of probe incidence was set to  $\theta_i = 40^\circ$ . The measured transient reflectivity signal, the signal with the removed slowly-varying background, and the resulting frequency spectrum of the latter, are presented in Fig. 2.11 (a), (b) and (c) respectively.

To test the rotation mechanism, I have then measured the Brillouin frequency for different values of the probe incidence angles. The chosen values of  $\theta_i$  are  $40^\circ$ ,  $45^\circ$ ,  $50^\circ$ ,

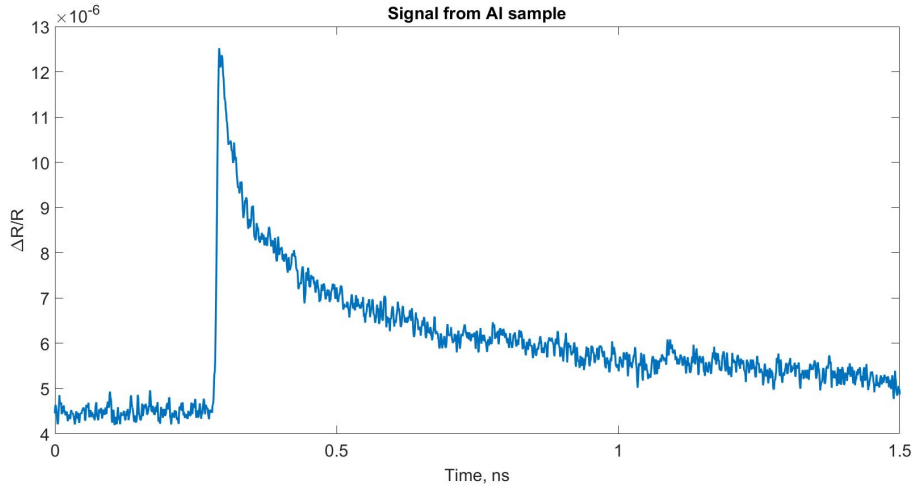


Figure 2.10 – Transient reflectivity measurement on an Al sample.

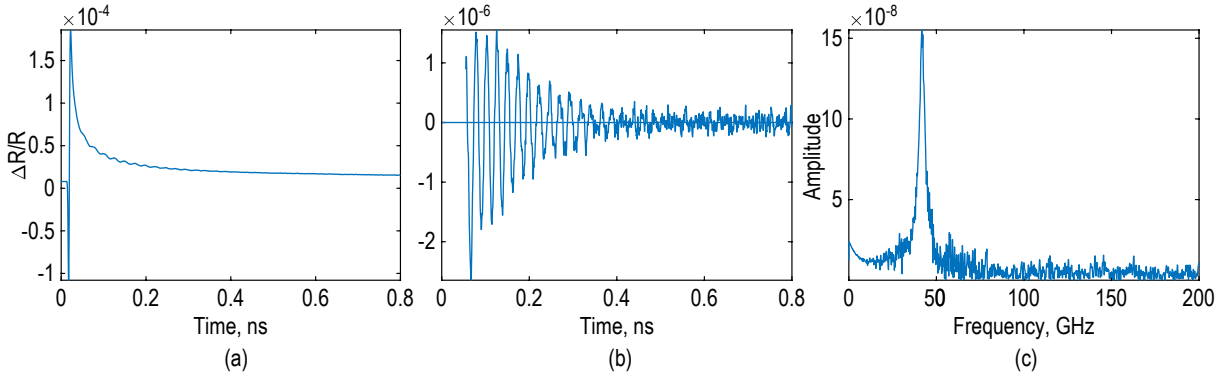


Figure 2.11 – (a) Result of the transient reflectivity measurement. (b) Result of the fitted background subtraction from the measured signal where the non-oscillating part before 0.01 ns has been cut out. (c) Fourier transform of the oscillating part of the measured signal (after 0.1 ns on the graph) showing 41.63 GHz Brillouin frequency.

$55^\circ$ ,  $63^\circ$ , and  $73^\circ$ , which corresponds to the refracted angles  $\theta_{in}$  of  $10^\circ$ ,  $11^\circ$ ,  $12^\circ$ ,  $13^\circ$ ,  $14^\circ$ , and  $15^\circ$  inside the GaAs sample, respectively. The dependance of the calculated and measured Brillouin frequency on the refracted angle  $\theta_{in}$  are shown in Fig. 2.12, where measurements for 6 different angles of incidence were done consecutively, with 50 averages per measure. The figure includes the error bars that represent the full-width at half maximum (FWHM) of the Brillouin peak in the Fourier space. This figure also shows the theoretical Brillouin frequencies calculated for two different longitudinal wave velocities in GaAs, where the Brillouin frequency  $f_B$  are calculated using the formula Eq. (1.4), reminded here for convenience:

$$f_B = \frac{2nv_{ac}}{\lambda_0} \cos \theta_{in}. \quad (2.3)$$

The refractive index of GaAs at  $\lambda_0 = 810$  nm is  $n = 3.669$  (taken from [191]),  $v_{ac} = 5397$  m s $^{-1}$  and  $5447$  m s $^{-1}$  are the maximum and minimum values of the longitudinal wave velocity taken from Ref. [192]. The expected decrease of the Brillouin frequency with

increasing incidence angle is experimentally recovered, with the complete interval of the theoretically-estimated values inside the confidence interval of the experimental results.

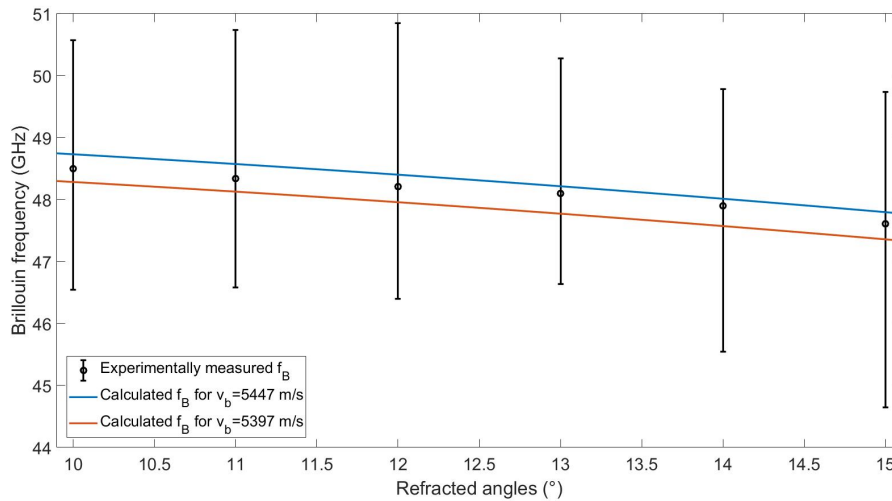


Figure 2.12 – Dependence of the Brillouin frequency on the probe incidence angle.

## 2.7 Chapter summary

In this Chapter, the experimental setup has been presented in details. The versatility of its use for doing reflectometric or interferometric detection has been introduced. Then, the chosen solution for allowing easy change of the probe angle of incidence has been described and explained in details for the most important components where the good choice will matter for the good operation of the instrument. Few indications on how to install, align and adjust some key elements have also been described. Finally, the first signals obtained in reflectometric regime of detection have been shown.

Now that the practical details about the implemented solution of our Sagnac inteferometer and the first experimental (reflectometric) results have been discussed, the next chapter will focus on the interferometric regime of detection. On the one hand, theoretical expectations about the signals that can be detected thanks to this interferometer will be discussed, together with what could be critical for obtaining satisfying results. On the other hand, our Sagnac interferometer will finally be put at use to conduct an experiment of depth profiling in a homogeneous sample of GaAs, to demonstrate its working capabilities and discuss some of its characteristics.

# ULTRAFAST OPTICAL INTERFEROMETRY FOR DEPTH-PROFILING OF MATERIALS BY TIME-DOMAIN BRILLOUIN SCATTERING

---

As presented in the previous chapter 2, a self-stabilized Sagnac inteferometer has been designed and assembled in order to allow precise and easy variations of the probe incidence angle with the particularity that it keeps the optical path always constant and that the sample remains motionless relatively to the pump beam. It is now proposed to apply this interferometer to perform time-domain Brillouin scattering (TDBS) by ultrafast optical interferometry, making possible to split the variations in amplitude and in phase of the transient optical field reflectivity, contrary to the case where the TDBS measurement is achieved by means of reflectometry measurement. This possibility should allow to reveal the best axial resolution the TDBS technique can offer, which should not be limited by the probed acoustic wavelength set by the Brillouin scattering interaction, but by the characteristic length of the acoustic pulse. There should be no limitation coming from the signal processing either, since the instantaneous frequency should be (theoretically) directly derivable from the measured instantaneous phase.

In this chapter, it is proposed first to discuss, from a theoretical point of view, the expected performance such an interferometric-based TDBS measurement should be able to provide. The limitations will also be discussed, especially with regards to the fact that the detected signal will never be coming only from acoustic contributions. A signal processing procedure will then be proposed in order to allow the extraction of the acoustic contributions from the experimental signals. Experiments on a homogeneous sample made of GaAs will be presented to demonstrate experimentally the possibilities and the limitations of the constructed interferometer. A discussion summarizing the results and the important conclusions that can be drawn from them will close the chapter.

### 3.1 Theoretical expectations on axial resolution

Until now, to the best of our knowledge, there are no definite experimental prove for the expectations that the axial (along the propagation direction of the coherent acoustic pulse [CAP], i.e., depth) resolution in TDBS imaging could be limited only by the CAP spatial localization, i.e., the width of the launched CAP or the width of the strain front in the CAP where the photoelastic scattering of the probe light takes place. Although it has been demonstrated that the axial resolution can be deeply sub-optical [15, 16], the axial resolution limited by the CAP spatial localization has not yet been demonstrated.

As already discussed in chapter 1 and in our opinion, this situation is largely due to the fact that, until now, only the detection of the transient optical intensity reflectivity,  $dR/R$ , was realized in the ultrafast pump-probe experiments for the imaging via TDBS technique. These experiments measure the amplitude of the optical electric field reflectivity,  $dr/r$ , where the information the phase of  $dr/r$  is lost because of  $R = rr^* = |r|^2$ . Thus, one or another type of signal processing should be applied to the detected Brillouin oscillations with time-varying amplitude and frequency, in order to formally extract the time-dependent frequency, carrying the information on the local refractive index,  $n(t)$ , and sound velocity,  $v_{ac}(t)$ . In most of the cases, different kinds of the processing based on the integral transforms (like Fourier or Hilbert transforms) are applied, and the axial resolution of the TDBS is limited by the temporal width, related to the spatial width by  $v_{ac}(t)$ , of the window for the integral transformation. Usually, this window is not shorter than one length of the Brillouin oscillation, which in turn is not shorter than half of the probe light wavelength in the medium. Therefore, the reported axial resolution can be sub-optical but not deeply sub-optical. The case of deeply sub-optical axial resolution was reported by the fitting of the fractions of a single Brillouin oscillation period in the time-domain to the theoretical expectations [15, 16]. However, in this case, the ability to reveal the local values of the Brillouin frequency with the highest axial resolution is also limited, similarly to the application of the integral transforms, by the uncertainty in the values of the fitting theoretical parameters, which is increasing with diminishing interval of signal fitting, the number of the experimentally measured points in this interval and the signal-to-noise ratio. In addition, the fits are explicitly assuming quasi-periodic sinus-like (harmonic) variations of acoustically-induced  $dR/R$ , which is not a local experimental observation.

The information on the local  $n(t)$  and  $v_{ac}(t)$  is theoretically « hidden » inside the change of the phase shift between the acoustically-scattered light and the reflected light used for heterodyning, i.e., in variations in the phase of  $dr/r$  [17, 57]. This phase is proportional to the optical thickness of the media, separating the CAP and the stationary surfaces/interfaces reflecting the probe light. Thus, the phase shift variation during the small time interval  $dt$  depends on the local refractive index in the position of the CAP,

$n(t)$ , and the CAP displacement,  $v_{ac}(t)dt$ , which controls the change of the geometrical thickness of the media separating the CAP and the stationary surface/interfaces reflecting probe light. Therefore, as introduced in chapter 1, the information on the local  $n(t)$  and  $v_{ac}(t)$  is contained in the time derivative,  $\frac{\partial\varphi_r}{\partial t}(t)$ , of the transient optical field reflectivity phase,  $\varphi_r(t)$ . In the situation where the CAP is launched from the surface of a semi-infinite sample, with material inhomogeneity only in the direction normal to its surface, the probe light is scattered once by the CAP and reflected once at the surface, and the time derivative of the transient optical field reflectivity phase reads

$$\frac{\partial\varphi_r}{\partial t}(t) = 2\pi \frac{2n(t)v_{ac}(t)}{\lambda_0} \cos[\theta_{in}(t)], \quad (3.1)$$

where  $\theta_{in}(t)$  is the local angle between the directions of the CAP and the  $\lambda_0$ -wavelength probe light propagation inside the medium. Measurement of  $\varphi_r(t)$  and its time derivative calculation should then provide the opportunity to determine the local product  $n(t)v_{ac}(t)$ , without the need to discuss/define the Brillouin frequency, and hence without the need to use signal processing techniques to assess instantaneous frequency of a signal. Hence, the characteristic dimension of the CAP should theoretically be the only limitation to the axial resolution.

## 3.2 Choice of the incidence angle range for good sensitivity

For creating the separate images of the optical refractive index and of the sound velocity, it is desirable to make the imaging with the smallest number of probe light incidence angles, leading to clear distinct measurements of different time trace of  $\frac{\partial\varphi_r}{\partial t}(t)$  [Eq. (3.1)]. In the simplest and the most relevant to our future experimental show-cases analysis, we consider a semi-infinite medium with the parameters varying along a single direction, which is normal to the sample/air interface. The refraction of the probe light, when it propagates in such continuously layered media with varying  $n(t)$ , is described by the relation

$$n(t) \sin[\theta_{in}(t)] = \sin(\theta_i), \quad (3.2)$$

where  $\theta_i$  is the angle of probe light incidence on the air/sample interface and where we approximated the refractive index of air by 1. Then,

$$\frac{\partial\varphi_r}{\partial t}(t) = \frac{2\pi}{\lambda_0} 2v_a(t) \sqrt{[n(t)]^2 - [\sin(\theta_i)]^2}. \quad (3.3)$$

Therefore, the differentiation of this relation over  $\theta_i$  predicts that

$$\frac{\partial^2 \varphi_r}{\partial \theta_i \partial t}(t) = -\frac{2\pi}{\lambda_0} v_a(t) \sin(2\theta_i) / \sqrt{[n(t)]^2 - [\sin(\theta_i)]^2}. \quad (3.4)$$

Thus,  $\frac{\partial \varphi_r}{\partial t}(t)$  of our interest exhibits the slowest variation with the angle of probe incidence for the nearly normal incidence of the probe on the surface,  $\theta_i \rightarrow 0$ . With increasing angle of probe incidence, the magnitude of  $\frac{\partial \varphi_r}{\partial t}(t)$  is continuously increasing. The fastest variations take place for incidence angle of the probe light around  $45^\circ$ ,  $\theta_i \rightarrow \pi/4$ .

From the previous discussions, it is therefore expected that the best axial resolution can be performed thanks to the use of an interferometric measurement and it is also expected that the best sensitivity to variations with respect to the angle of incidence is not at very small nor at very large incidence angles, but at angle of incidence around  $45^\circ$ . It is now proposed to derive a model for the intensity field reaching the balanced photodetector in order to mind-print the best case scenario, to analyze which factors are most likely to cause actual performance to deviate from their theoretical expectations and to discuss how to prevent this experimentally.

### 3.3 Light intensity reaching the photodetector in ultrafast optical interferometry

The interferometric signal is obtained by making the two pulse split from the delayed probe pulse (namely, the reference pulse and the probing pulse) to interfere on the photo-sensitive surface of the « + » channel of the photodetector. To derive the light intensity on that surface of detection, it is convenient to perform Jones calculus.

To do so, a simplified version of the interferometric part of the constructed setup is depicted in Fig. 3.1. The time-delayed probe pulse is split on the non-polarizing beam splitter (NPBS) in two parts: a first part is steered to the « - » channel of the balanced photodetector ; a second part is further divided in two on the polarizing beam splitter (PBS). The probing pulse (red solid line) is propagating clockwise, starting with a polarization perpendicular to the plane of incidence, referred to a s-polarization, just after reflection on the PBS and escaping the interferometer loop with a polarization parallel to the plane of incidence, referred to a p-polarization, upon transmission through the PBS. The reference pulse (black dotted line) is propagating counter-clockwise, starting with a p-polarization just after transmission by the PBS and escaping the interferometer loop with a s-polarization upon reflection on the PBS. Finally, those two probe pulses escaped from the interferometer loop reflect on the NPBS towards the « + » channel of the balanced photodetector. It is clear that both electric fields are orthogonally polarized (linear

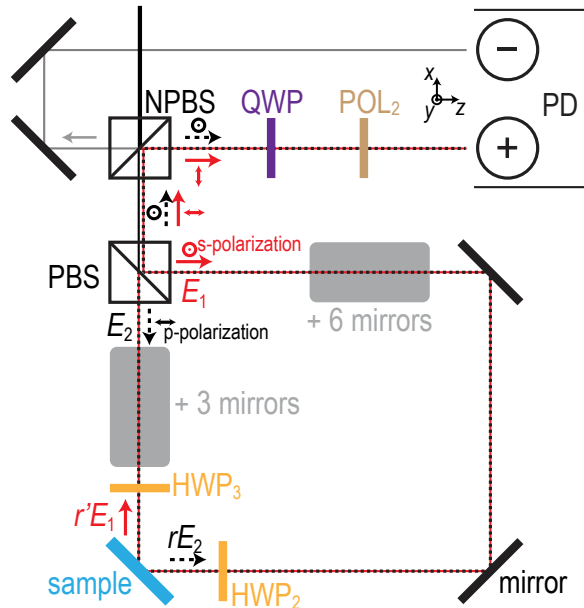


Figure 3.1 – Simplified version of the interferometric part of the constructed setup. The polarizations are depicted by double-headed arrows or circles with centered points for p-polarization and s-polarization, respectively. The probing beam clockwise path ( $E_1$ ) is in red solid lines. The reference beam counter-clockwise path ( $E_2$ ) is in black dotted lines. The light path dedicated to balance the photodetector is in gray solid lines. PD: photodetector, NPBS: non-polarizing beam splitter, PBS: polarizing beam splitter, HWP: half-wave plate, QWP: quarter-wave plate, POL: polarizer.

p-polarization and linear s-polarization) at the output of the interferometer loop (after the PBS) and that, upon the last reflection on the NPBS, an additional  $\pi$  phase shift is introduced since the p-polarized light (probing) is reversed, contrary to the s-polarized one (reference). Note that assuming a  $\pi$  phase shift is, strictly saying, inaccurate because the reflection coefficients of p-polarized and s-polarized light are theoretically not equal, which is disregarded here.

Consider the probing  $E_{1r}$  and the reference  $E_{2r}$  complex amplitudes of the corresponding electric fields, the Jones vector of the total electric field after the NPBS reads, following the previous discussion:

$$\vec{E}_{tot} = \begin{pmatrix} -E_{1r} \\ E_{2r} \end{pmatrix}. \quad (3.5)$$

Using the Jones calculus (details of which are given in Appendix B), the total electric field after the quarter-wave plate (QWP) and polarizer (POL<sub>2</sub>) can be obtained, leading to the expression of the intensity.

Contrary to the case discussed in chapter 1 (Sec. 1.4.3), while presenting the solution to make interfere orthogonally polarized light waves discussed in Ref. [186], the choice has been made in our case to set the QWP either to  $0^\circ$  and  $90^\circ$  (two measurements have to be done) and to set the polarizer POL<sub>2</sub> at  $45^\circ$ , as done in Ref. [13]. This is indeed preferable

in our case because we are using a thick polarizer, the rotation of which hence being able to induce unwanted beam walking.

From Jones calculus (Appendix B), the total electric field after the QWP set to an arbitrary angle  $\psi$  and the POL<sub>2</sub> set to 45° reads:

$$\vec{E}_{tot}^{\psi} = \frac{e^{i\pi/4}}{\sqrt{2}} (-A_{\psi}E_{1r} + B_{\psi}E_{2r}) \begin{bmatrix} \frac{1}{\sqrt{2}} \\ \frac{1}{\sqrt{2}} \end{bmatrix}, \quad (3.6)$$

where  $A_{\psi}$  and  $B_{\psi}$  are defined as follows:

$$A_{\psi} = \cos^2 \psi + i \sin^2 \psi + (1 - i) \sin \psi \cos \psi, \quad (3.7a)$$

$$B_{\psi} = \sin^2 \psi + i \cos^2 \psi + (1 - i) \sin \psi \cos \psi. \quad (3.7b)$$

Consider now that  $r$  is the complex amplitude-reflection coefficient (reflectance) of the sample seen by the reference pulse ( $E_{2r}$ ) and that  $r'(t)$  is the coefficient seen by the probing pulse ( $E_{1r}$ ), where  $t$  is the time delay between the pump and the probe pulses. The reflectance seen by the reference pulse is assumed to be  $r = r_0 e^{i\varphi_0}$  and that seen by the probing pulse is assumed to be  $r'(t) = r_0 e^{i\varphi_0} (1 + \rho(t) e^{i\varphi_r(t)})$ , where  $\rho(t)$  and  $\varphi_r(t)$  stand for the amplitude and phase of the relative perturbation of the sample reflectance, respectively, induced by the pump pulse. It is assumed that  $\rho(t) \ll 1 \forall t$ . Note that this expression of  $r'(t)$  is not the same as in Ref. [13]. With the here-assumed definition of  $r$  and  $r'(t)$ , the relative variation in the complex optical electric field reflectivity  $dr(t)/r$  is:

$$\frac{dr}{r}(t) = \frac{r'(t) - r}{r} = \rho(t) e^{i\varphi_r(t)}. \quad (3.8)$$

Note also that we cannot assume here that  $\varphi_r(t)$  is small relative to 1, contrary to the described case in Ref. [13] of an absorbing material, because the sample is here assumed to be transparent and hence  $\varphi_r(t)$  will increase with time while the acoustic pulse will propagate. Following the definitions of  $r$  and  $r'(t)$ , the reference and probing electric fields can be expressed as:

$$E_{1r} = r'(t)E_1, \quad (3.9a)$$

$$E_{2r} = rE_2, \quad (3.9b)$$

where  $E_1$  and  $E_2$  are the amplitude of reference and probing electric fields incident on the sample surface, respectively.

Using Eqs. (4.2) in Eq. (3.6) allows to derive the expression of the total electric field intensity  $I_{\psi}$  reaching the « + » channel of the photodetector. Omitting the dependency

of  $r'$  with  $t$  and with the complex conjugation noted as « \* », the intensity reads:

$$I_\psi = \frac{1}{2} \left[ r'(r')^* A_\psi A_\psi^* E_1^2 + r r^* B_\psi B_\psi^* E_2^2 - E_1 E_2 \left( r' r^* A_\psi B_\psi^* + (r')^* r A_\psi^* B_\psi \right) \right]. \quad (3.10)$$

The factors in Eq. (3.10) read as follows:

$$r'(r')^* = r_0^2 \left[ 1 + 2\rho(t) \cos \varphi_r(t) + \rho(t)^2 \right] \approx r_0^2 \left[ 1 + 2\rho(t) \cos \varphi_r(t) \right], \quad (3.11a)$$

$$r r^* = r_0^2, \quad (3.11b)$$

$$r' r^* = r_0^2 \left[ 1 + \rho(t) e^{+i\varphi_r(t)} \right], \quad (3.11c)$$

$$(r')^* r = r_0^2 \left[ 1 + \rho(t) e^{-i\varphi_r(t)} \right], \quad (3.11d)$$

$$A_\psi A_\psi^* = 1 + \frac{1}{2} \sin 4\psi, \quad (3.11e)$$

$$B_\psi B_\psi^* = 1 - \frac{1}{2} \sin 4\psi, \quad (3.11f)$$

$$A_\psi B_\psi^* = \sin^2(2\psi) - i \cos(2\psi), \quad (3.11g)$$

$$A_\psi^* B_\psi = \sin^2(2\psi) + i \cos(2\psi). \quad (3.11h)$$

From the previous expressions, it can be seen in particular that, for  $\psi = 0^\circ$  and  $\psi = 90^\circ$ , the following simplifications appear:

$$A_{0^\circ} A_{0^\circ}^* = A_{90^\circ} A_{90^\circ}^* = 1, \quad (3.12a)$$

$$B_{0^\circ} B_{0^\circ}^* = B_{90^\circ} B_{90^\circ}^* = 1, \quad (3.12b)$$

$$A_{0^\circ} B_{0^\circ}^* = A_{90^\circ}^* B_{90^\circ} = -i, \quad (3.12c)$$

$$A_{90^\circ} B_{90^\circ}^* = A_{0^\circ}^* B_{0^\circ} = +i, \quad (3.12d)$$

$$(3.12e)$$

which leads to:

$$I_{0^\circ}(t) = \frac{r_0^2}{2} \left[ E_1^2 + E_2^2 + 2E_1^2 \rho(t) \cos \varphi_r(t) - 2E_1 E_2 \rho(t) \sin \varphi_r(t) \right], \quad (3.13a)$$

$$I_{90^\circ}(t) = \frac{r_0^2}{2} \left[ E_1^2 + E_2^2 + 2E_1^2 \rho(t) \cos \varphi_r(t) + 2E_1 E_2 \rho(t) \sin \varphi_r(t) \right]. \quad (3.13b)$$

Assuming that the detector sensitivity  $S$  in  $\text{V m}^2 \text{W}^{-1}$  is the same for both channels, it is clear from Eqs. (3.13) that the needed intensity  $I_{ref}$  for balancing the photodetector (see gray solid line reaching the « - » channel of the photodetector in Fig. 3.1) is the same for these two orientations of QWP:  $I_{ref} = \frac{r_0^2}{2} (E_1^2 + E_2^2)$ . It is also obvious that equating the amplitude of both reference and probing electric fields,  $E_1 = E_2$ , leads to the possibility of splitting the time variation of  $\rho(t)$  to that of  $\varphi_r(t)$  by differently combining the half-sum and the half-difference of below presented outputs of the balanced photodetector obtained

for  $\psi = 0^\circ$  and  $\psi = 90^\circ$ :

$$s_{0^\circ}(t) = S(I_{0^\circ}(t) - I_{ref}) = Sr_0^2 E_1^2 [\rho(t) \cos \varphi_r(t) - \rho(t) \sin \varphi_r(t)], \quad (3.14a)$$

$$s_{90^\circ}(t) = S(I_{90^\circ}(t) - I_{ref}) = Sr_0^2 E_1^2 [\rho(t) \cos \varphi_r(t) + \rho(t) \sin \varphi_r(t)], \quad (3.14b)$$

which leads to:

$$Sr_0^2 E_1^2 \rho(t) = \sqrt{\left[\frac{s_{90^\circ}(t) + s_{0^\circ}(t)}{2}\right]^2 + \left[\frac{s_{90^\circ}(t) - s_{0^\circ}(t)}{2}\right]^2}, \quad (3.15a)$$

$$\varphi_r(t) = \mathcal{U} \left\{ \arctan \left[ \frac{s_{90^\circ}(t) - s_{0^\circ}(t)}{s_{90^\circ}(t) + s_{0^\circ}(t)} \right] \right\}, \quad (3.15b)$$

where  $\mathcal{U}$  is the phase unwrapping operation.

### 3.4 Illustration of the theoretical expectations and of few factors influencing the actual performances

To obtain the expressions of  $\rho(t)$  and  $\varphi_r(t)$  in Eqs.(3.15), it is important to remember that the expression  $r'(t) = r_0 e^{i\varphi_0} [1 + \rho(t)e^{i\varphi_r(t)}]$  has been assumed, where  $\rho(t)$  and  $\varphi_r(t)$  are linked to the transient optical field reflectivity variation due to a propagating acoustic pulse in a transparent semi-half space. Unfortunately,  $r'(t)$  is usually « poisoned » by extra terms caused by the pump laser pulse because of the temperature dependence of the optical reflectivity and/or by the processes taking place during the short intervals of time when the acoustic strain pulse interacts with the surfaces/interfaces [17]. It is proposed in this section to first illustrate ideal cases with constant and linear variations with time of acoustic velocity and refractive index and then to look at effects on the signals and calculated  $\rho(t)$  and  $\varphi_r(t)$  of different types of « poisoning » terms.

For all cases treated in this section, the probe wavelength is assumed to be  $\lambda_0 = 800$  nm, the incidence angle of the probe light on the free surface of the semi-half space is assumed to be  $\theta_i = 45^\circ$  and the acoustic velocity and refractive index at  $\lambda_0$  are based on that of GaAs. The laws of  $v_{ac}(t)$  and  $n(t)$  time variations are:

$$v_{ac}(t) = v_{ac}(0) = 4730 \text{ nm ns}^{-1} \forall t, \quad (3.16a)$$

$$n(t) = n(0) = 3.6835 \forall t, \quad (3.16b)$$

in the case of constant parameters equivalent to a homogeneous sample of GaAs and:

$$v_{ac}(t) = v_{ac}(0)(1 - 0.5t), \quad (3.17a)$$

$$n(t) = n(0)(1 - 0.3t), \quad (3.17b)$$

in the case of a linear decrease of  $v_{ac}(t)$  and  $n(t)$  with time with a rate of 50% and 30% decrease per nanosecond, respectively, equivalent to an inhomogeneous sample. The transient optical field reflectivity variations in amplitude and phase are defined as:

$$\rho(t) = Ae^{-t/\tau}, \quad (3.18a)$$

$$\varphi_r(t) = \frac{4\pi}{\lambda_0} \int_0^t v_{ac}(t') \sqrt{n(t')^2 - \sin^2 \theta_i} dt', \quad (3.18b)$$

where  $A$  and  $\tau$  stand for the amplitude and the decay time of the acoustic contribution to the transient optical field reflectivity, respectively, and are set to  $A = 10^{-6}$  and  $\tau = 0.3$  ns. The signals are assumed to be measured over 1 ns, with a sampling frequency of 1 THz. The reference and probing electric field amplitude are assumed to be equal and set to unity:  $E_1 = E_2 = 1 \text{ V m}^{-1}$ .

### 3.4.1 Ideal cases

First, it is ideally considered that there is no other contribution in  $s_{0^\circ}$  and  $s_{90^\circ}$  than the acoustic one. In the case of a homogeneous sample, the simulated output signals from the balanced photodetector,  $s_{0^\circ}(t)$  and  $s_{90^\circ}(t)$ , normalized by the detector sensitivity  $S$ , are depicted in Fig. 3.2(a) for  $\psi = 0^\circ$  (top) and  $\psi = 90^\circ$  (bottom). Both signals show a damped sine function with a constant frequency and are in quadrature, as expected. The calculated temporal variations of  $\rho(t)$  and  $\varphi_r(t)$  [orange solid lines in Fig. 3.2(b)] superimpose with the set ones [black dashed lines in Fig. 3.2(b)] as expected from the theory.

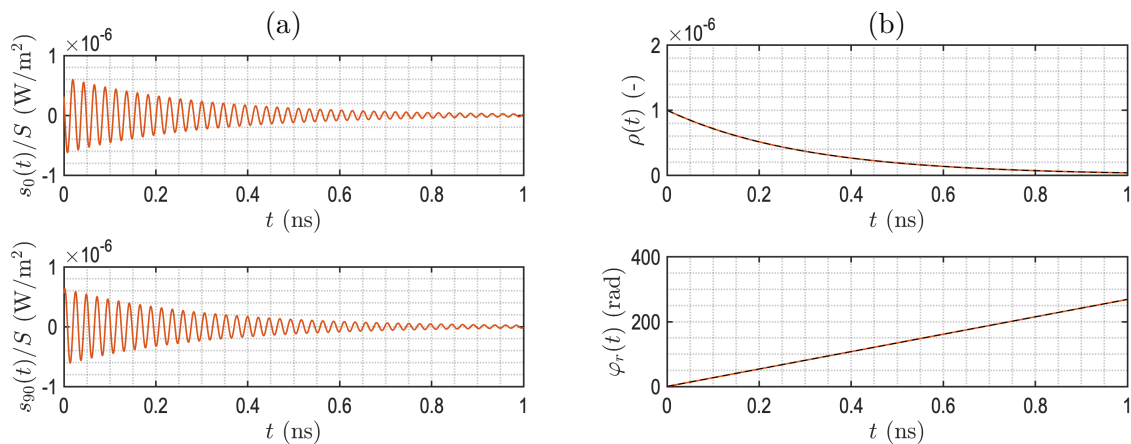


Figure 3.2 – Ideal case of the acoustic contribution for a homogeneous sample: (a)  $s_{0^\circ}(t)/S$  (top) and  $s_{90^\circ}(t)/S$  (bottom) as a function of pump-probe delay, (b)  $\rho(t)$  (top) and  $\varphi_r(t)$  (bottom) as a function of pump-probe delay. In (b), the set temporal variations of  $\rho(t)$  and  $\varphi_r(t)$  are the black dashed lines, while the calculated ones from the signals in (a) are the orange solid lines.

In the case of an inhomogeneous sample, the normalized simulated output signals from

the balanced photodetector,  $s_{0^\circ}(t)/S$  and  $s_{90^\circ}(t)/S$ , are depicted in Fig. 3.3(a) for  $\psi = 0^\circ$  (top) and  $\psi = 90^\circ$  (bottom). Both signals show also a damped sine function and are also in quadrature, but the instantaneous frequency is now decreasing with time. Yet, the set variations and the calculated temporal ones of  $\rho(t)$ , which is the same as for the case of the homogeneous sample, and  $\varphi_r(t)$ , which deviates from the linear law to a power law of degree 3 here, still superimpose [Fig. 3.3(b)].

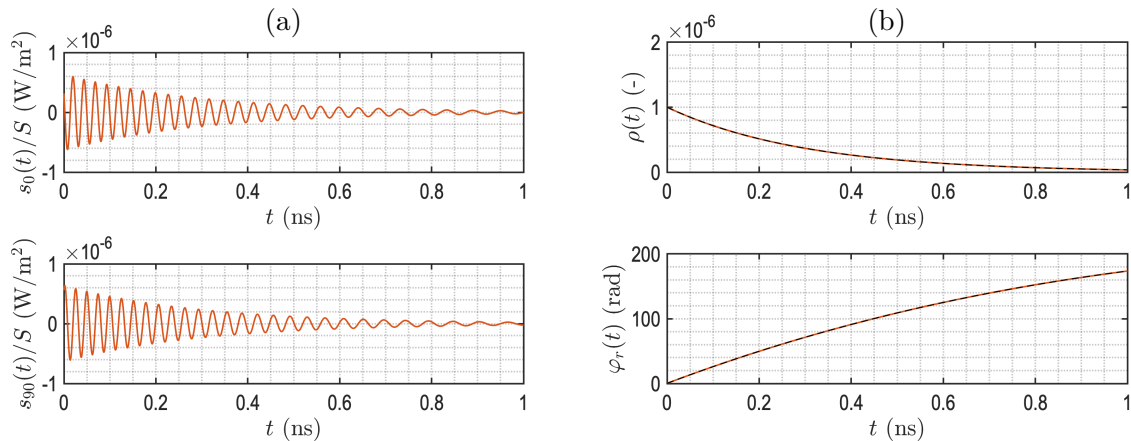


Figure 3.3 – Ideal case of the acoustic contribution for an inhomogeneous sample: (a)  $s_{0^\circ}(t)/S$  (top) and  $s_{90^\circ}(t)/S$  (bottom) as a function of pump-probe delay, (b)  $\rho(t)$  (top) and  $\varphi_r(t)$  (bottom) as a function of pump-probe delay. In (b), the set temporal variations of  $\rho(t)$  and  $\varphi_r(t)$  are the black dashed lines, while the calculated ones from the signals in (a) are the orange solid lines.

The previous results show that in the ideal case, where only acoustic perturbations contribute to the signals, where all other parameters are precisely set to their correct (set by the theory) value and without any source of noise, the reconstructed amplitude and phase variations match perfectly the theory. In a real-life experiments, everything is far from being perfect and it is now proposed to discuss few perturbations from the ideal case and their effects on the results.

### 3.4.2 Effect of misbalancing the reference and probing electric field amplitudes

Everything being set as previously, the effect of misbalancing the reference and probing electric field amplitudes is illustrated by assuming a ratio of  $E_2$  to  $E_1$  equal to  $1/2$ :  $E_1 = 1 \text{ V m}^{-1}$  and  $E_2 = 0.5 \text{ V m}^{-1}$ . The obtained results in such case for a homogeneous sample are shown in Fig. 3.4, while those for an inhomogeneous sample are in Fig. 3.5. In both cases, it is clear that the amplitudes of  $s_{0^\circ}(t)$  and  $s_{90^\circ}(t)$  are now different, resulting in a clear oscillating effect on the reconstructed temporal evolution of  $\rho(t)$  [top of Figs. 3.4(b) and 3.5(b)], while the reconstructed evolutions of  $\varphi_r(t)$  [bottom of Figs. 3.4(b) and 3.5(b)] seem to be less affected by this mismatch. In order to quantify this effect, the normalized

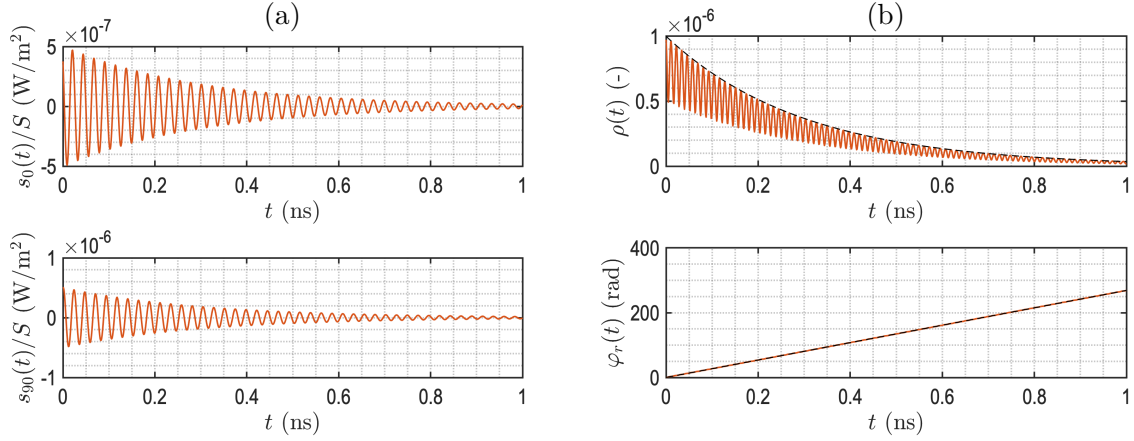


Figure 3.4 – Effect of misbalancing the reference and probing electric field amplitudes for a homogeneous sample: (a)  $s_0(t)/S$  (top) and  $s_{90^\circ}(t)/S$  (bottom) as a function of pump-probe delay, (b)  $\rho(t)$  (top) and  $\varphi_r(t)$  (bottom) as a function of pump-probe delay. In (b), the set temporal variations of  $\rho(t)$  and  $\varphi_r(t)$  are the black dashed lines, while the calculated ones from the signals in (a) are the orange solid lines.

root mean squared error (NRMSE) between the set (black dashed lines) and reconstructed (orange solid lines) temporal variations of  $\rho(t)$  and  $\varphi_r(t)$  are calculated. The NRMSE is defined as  $NRMSE = \sqrt{\frac{1}{N} \sum_{n=1}^N (y_n - \hat{y}_n)^2} / (\max_n y_n - \min_n y_n)$ , where  $N$  is the total number of points in time,  $y_n$  and  $\hat{y}_n$  are the set and reconstructed parameter (either amplitude or phase). In both cases of a homogeneous and an inhomogeneous samples, the NRMSE for the amplitude is equal to 11.6%, while that for the phase is equal to about 0.1%, confirming the observation that the effect of misbalancing  $E_1$  and  $E_2$  has much more influence on the reconstruction of  $\rho(t)$  than that of  $\varphi_r(t)$ . Indeed, even though  $I_{ref}$  is set correctly, the fact that  $E_1 \neq E_2$  precludes the factorization by  $E_1^2$  in Eqs. (3.14a), which leads to:

$$\sqrt{\left[\frac{s_{90^\circ}(t) + s_0(t)}{2}\right]^2 + \left[\frac{s_{90^\circ}(t) - s_0(t)}{2}\right]^2} = Sr_0^2 E_1^2 \rho(t) \sqrt{1 + \frac{E_2^2 - E_1^2}{E_1^2} \sin^2 \varphi_r(t)}, \quad (3.19)$$

which explains the oscillating behavior of the reconstructed  $\rho(t)$  at the top in Figs. 3.4(b) and 3.5(b).

### 3.4.3 Effect of thermal background

Everything being set as in the ideal case, the effect of thermal background usually encountered in experiments is now taking into account. To do so, an exponential term, decaying with time is added to reflection coefficient  $r'(t)$  that now reads:

$$r'(t) = r_0 e^{i\varphi_0} \left(1 + \rho(t) e^{i\varphi_r(t)}\right) + A_b e^{i(\varphi_0 + \varphi_b)} e^{-t/\tau_b}, \quad (3.20)$$

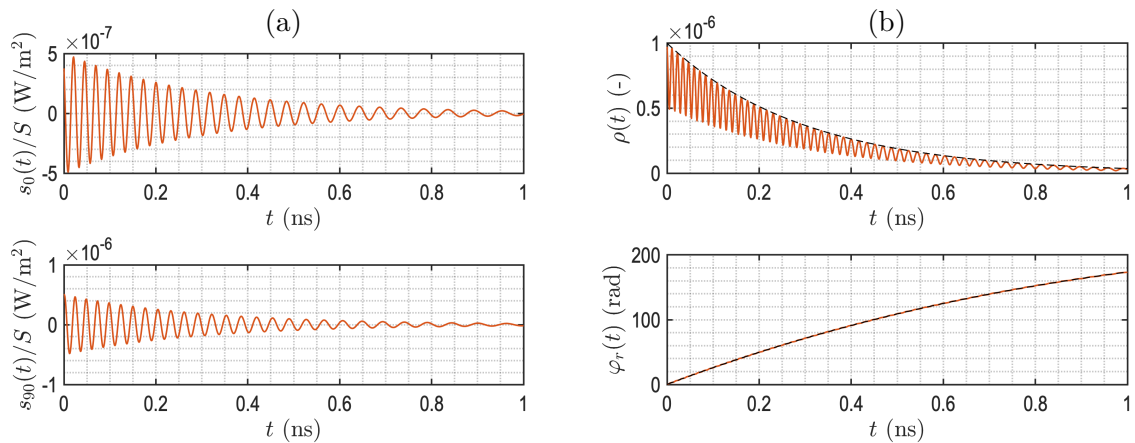


Figure 3.5 – Effect of misbalancing the reference and probing electric field amplitudes for an inhomogeneous sample: (a)  $s_{0^\circ}(t)/S$  (top) and  $s_{90^\circ}(t)/S$  (bottom) as a function of pump-probe delay, (b)  $\rho(t)$  (top) and  $\varphi_r(t)$  (bottom) as a function of pump-probe delay. In (b), the set temporal variations of  $\rho(t)$  and  $\varphi_r(t)$  are the black dashed lines, while the calculated ones from the signals in (a) are the orange solid lines.

where  $A_b$ ,  $\varphi_b$ , and  $\tau_b$  stand for the amplitude, the phase, and the decay time of the thermal background, respectively. For the illustration, those parameters are set to  $A_b = -2 \cdot 10^{-5}$ ,  $\varphi_b = \pi/6$ , and  $\tau_b = 0.5$  ns.

The effect of such a background on the output signals from the balanced photodetector is clear already in the case of a homogeneous material shown in Fig. 3.6(a): the acoustic parts of the signals (oscillations) are superimposed on a slowly decaying exponential term and the amplitudes of  $s_{0^\circ}(t)$  and  $s_{90^\circ}(t)$  are not equivalent anymore since the contributions of the background on the two last terms in the expression of  $I_{0^\circ}(t)$  and  $I_{90^\circ}(t)$  (Eq. (3.13)) are subtracted or added, respectively. Because of this « poisoning » term, the reconstructed temporal evolutions of  $\rho(t)$  and  $\varphi_r(t)$  are completely off compared to the expectation where only acoustic contributions are kept for the calculations. It will be seen in the next section 3.6 how to bypass this limitation.

### 3.4.4 Effect of sample properties variations between both measurements

In order to split the variations of the amplitude  $\rho(t)$  and the phase  $\varphi_r(t)$  of the transient reflectivity of the optical field, one obvious assumption, unmentioned up to now and yet very important, is that the two conducted measurements with the QWP at  $0^\circ$  and  $90^\circ$  done in a row should measure the same variations. Say differently, it is very important that the probed transient reflectivity of the optical field,  $dr(t)/r$ , is not changing between the two measurements. To demonstrate this important assumption, the case where the sample properties vary between two subsequent measurements is now proposed.

Everything being set as in the ideal case for an inhomogeneous sample, it is here as-

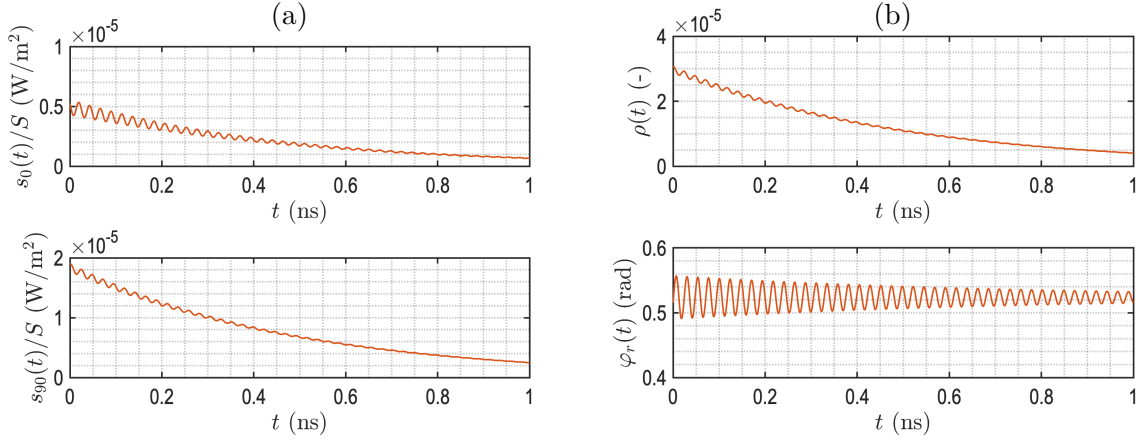


Figure 3.6 – Effect of taking into account the thermal background for a homogeneous sample: (a)  $s_{0^\circ}(t)/S$  (top) and  $s_{90^\circ}(t)/S$  (bottom) as a function of pump-probe delay, (b)  $\rho(t)$  (top) and  $\varphi_r(t)$  (bottom) as a function of pump-probe delay. In (b), the set temporal variations of  $\rho(t)$  and  $\varphi_r(t)$  are not shown in order to be able to see the calculated ones (orange solid lines).

sumed that  $v_{ac}(t)$  and  $n(t)$  vary between the two measurements. For the first measurement where  $\psi = 0^\circ$ ,  $v_{ac}^{0^\circ}(t)$  and  $n^{0^\circ}(t)$  read, as previously:

$$v_{ac}^{0^\circ}(t) = v_{ac}(0)(1 - 0.5t), \quad (3.21a)$$

$$n^{0^\circ}(t) = n(0)(1 - 0.3t). \quad (3.21b)$$

For the second measurement where  $\psi = 90^\circ$ ,  $v_{ac}^{90^\circ}(t)$  and  $n^{90^\circ}(t)$  read:

$$v_{ac}^{90^\circ}(t) = v_{ac}(0)(0.95 - 0.45t), \quad (3.22a)$$

$$n^{90^\circ}(t) = n(0)(0.95 - 0.25t). \quad (3.22b)$$

Changes in the value of the acoustic velocity and the refractive index at the origin of time, as well as changes in the linear rates of change, are introduced. This leads to the output signals of the balanced photodetector depicted in Fig. 3.7(a), where the introduced differences are not particularly eye-catching. Yet, comparing in Fig. 3.7(b) the set temporal variations of  $\rho(t)$  and  $\varphi_r(t)$  at the time of the first measurement ( $\psi = 0^\circ$ ) in black dashed lines to the calculated variations (orange solid lines) from the signals in (a), it is obvious that the later ones deviate from the former ones, hence precluding any hope to recover from these results the distributions of the acoustic and optical material properties.

### 3.4.5 Effect of measurement noises

Although the results of the previous subsection were expected since the tested material had undergone changes in properties between the two measurements, another case where

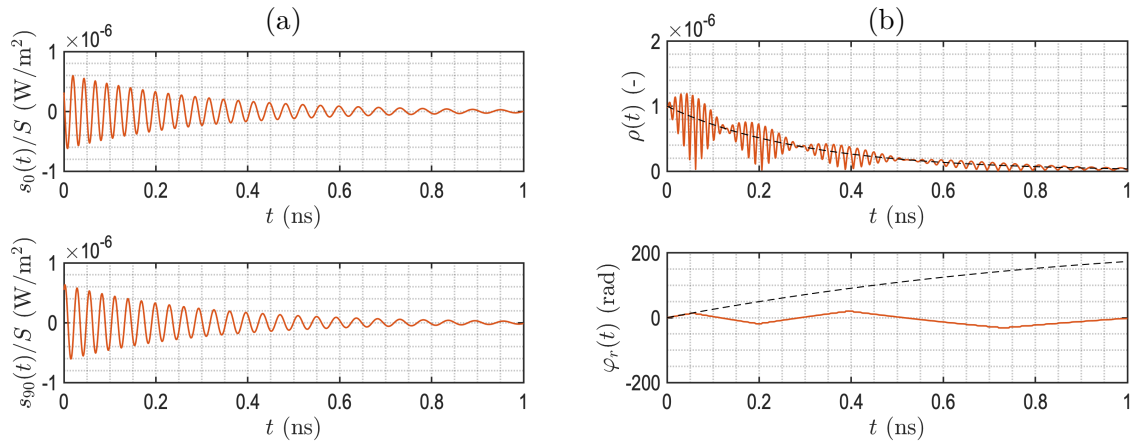


Figure 3.7 – Effect of sample properties variation between the measurement done with the QWP set at  $\psi = 0^\circ$  and that done with the QWP at  $\psi = 90^\circ$  for an inhomogeneous sample: (a)  $s_{0^\circ}(t)/S$  (top) and  $s_{90^\circ}(t)/S$  (bottom) as a function of pump-probe delay, (b)  $\rho(t)$  (top) and  $\varphi_r(t)$  (bottom) as a function of pump-probe delay. In (b), the set temporal variations of  $\rho(t)$  and  $\varphi_r(t)$  at the time of the first measurement ( $\psi = 0^\circ$ ) are the black dashed lines, while the calculated ones from the signals in (a) are the orange solid lines.

the measured signals at  $\psi = 0^\circ$  and  $\psi = 90^\circ$  might deviate from each other, although the material properties are stable, is encountered due to measurement noises.

Everything being set as in the ideal case for a homogeneous sample, it is considered that a different additive uniform white noise is added to each of the output signals of the photodetector  $s_{0^\circ}(t)$  and  $s_{90^\circ}(t)$  in both cases with a signal-to-noise ratio (SNR) of +3 dB. The results of one run are displayed in Fig. 3.8. The noise is clearly deteriorating the reconstruction of both  $\rho(t)$  and  $\varphi_r(t)$ . The NRMSE over the 1 ns of measurement for the amplitude is of about 20%, while that for the phase is of about 24%. By restricting the analysis to the first 0.3 ns, over which the SNR is +7.7 dB, the NRMSE for the amplitude increase to 30%, while that for the phase drastically drop to 0.4%. Say differently, the effect on the noise on the reconstruction of the phase of the transient reflectivity optical field seems to decrease as the level of the noise decrease, while such a conclusion cannot be drawn for the amplitude.

In order to complete this effect of the noise, this model has been run for 101 different SNRs, linearly distributed from -3 dB to +20 dB, each time 1000 times to vary the random noise and compute the mean and standard deviation of NRMSE for the amplitude and the phase over 1 ns at each SNR. The results of such a computation are shown in Fig. 3.9, where the solid line stands for the mean value of the NRMSE over the 1000 repetitions, while the vertical bars stand for the interval of 95% confidence (*i.e.*,  $\pm 2\sigma$ , with  $\sigma$  the standard deviation of the NRMSE over the 1000 repetitions).

It can be seen in Fig. 3.9 that the mean of the NRMSE follow the same trend for both reconstructions  $\rho(t)$  and  $\varphi_r(t)$ : the lower the SNR, the higher the error. Obviously, this trend was expected. More interestingly, the phase shows in average to be less sensitive

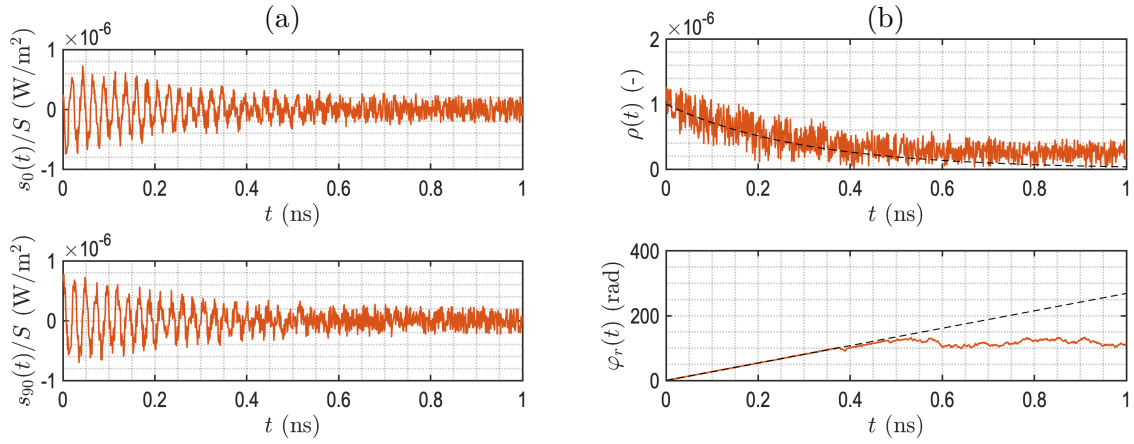


Figure 3.8 – Effect of noise measurements for a homogeneous sample: (a)  $s_{0^\circ}(t)/S$  (top) and  $s_{90^\circ}(t)/S$  (bottom) as a function of pump-probe delay, (b)  $\rho(t)$  (top) and  $\varphi_r(t)$  (bottom) as a function of pump-probe delay. In (b), the set temporal variations of  $\rho(t)$  and  $\varphi_r(t)$  are the black dashed lines, while the calculated ones from the noisy signals in (a) are the orange solid lines.

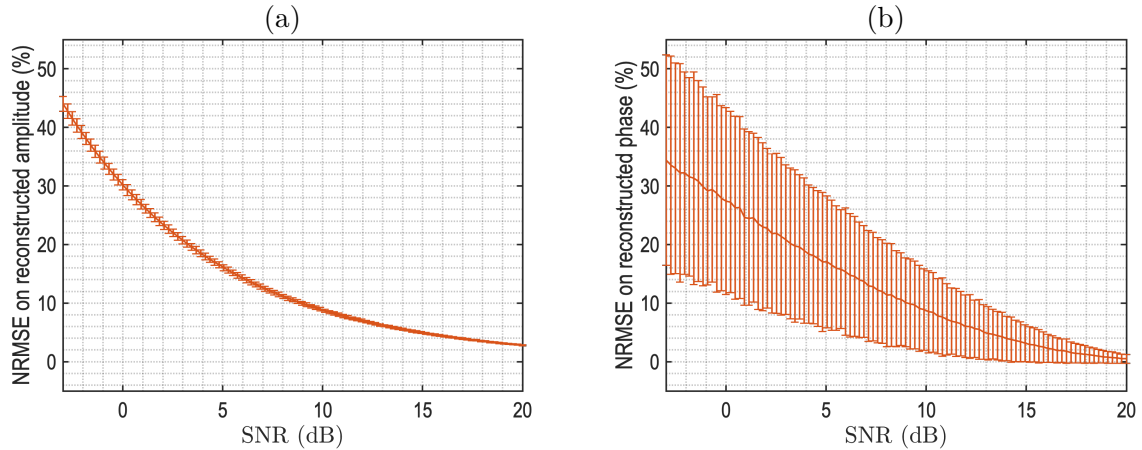


Figure 3.9 – Normalized root mean squared error (NRMSE) as a function of the signal-to-noise ratio (SNR) of  $s_{0^\circ}(t)$  and  $s_{90^\circ}(t)$  to which a uniform white noise has been added: (a) NRMSE of  $\rho(t)$ , (a) NRMSE of  $\varphi_r(t)$ . In (a) and (b), the solid line stands for the mean value of the NRMSE over 1000 repetitions of the simulation with the same SNR, while the vertical bars stand for the interval of 95% confidence (*i.e.*,  $\pm 2\sigma$ , with  $\sigma$  the standard deviation of the NRMSE over the 1000 repetitions).

to the additive white noise than the amplitude, no matter the SNR, but the error due to the noise is much more scattered (much less predictable) for the phase than for the amplitude. This analysis shows that having a good SNR is of utmost importance to have good confidence in the measured  $\varphi_r(t)$  and hence in the distribution of material properties one could obtain from it.

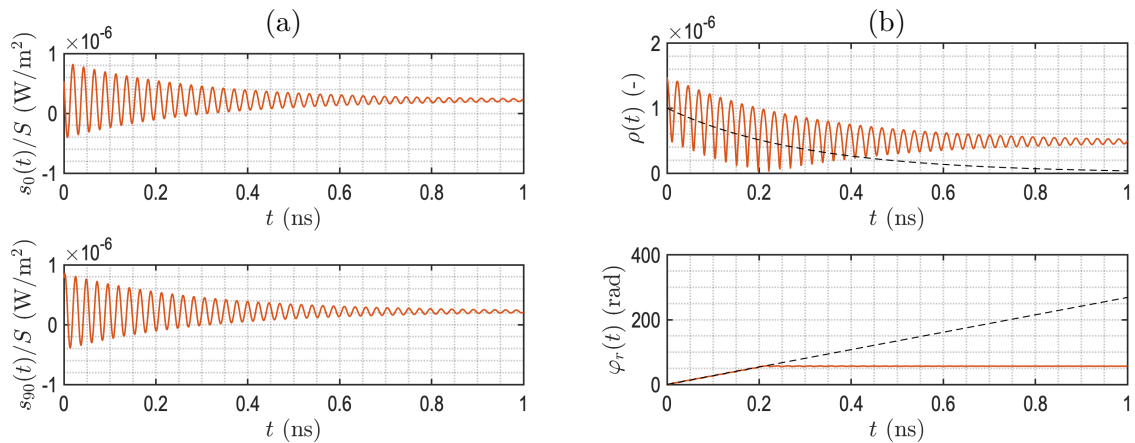


Figure 3.10 – Effect of QWP tiny misorientation for a homogeneous sample: (a)  $s_0(t)/S$  (top) and  $s_{90^\circ}(t)/S$  (bottom) as a function of pump-probe delay, (b)  $\rho(t)$  (top) and  $\varphi_r(t)$  (bottom) as a function of pump-probe delay. In (b), the set temporal variations of  $\rho(t)$  and  $\varphi_r(t)$  are the black dashed lines, while the calculated ones from the noisy signals in (a) are the orange solid lines.

### 3.4.6 Effect of the deviation from the expected $0^\circ$ and $90^\circ$ orientations of QWP

Last but not least, it is finally proposed to illustrate and analyze the effect of a misalignment of QWP from the ideal  $0^\circ$  and  $90^\circ$  angles between the fast axis of QWP and the p-polarization direction ( $x$ -axis in Fig. 3.1). Everything being set as in the ideal case for a homogeneous sample, the model is run by considering a tiny deviation of the angles that are set to  $\psi = 0.02^\circ$  and  $\psi = 89.98^\circ$ . The results for such a tiny deviation from the expected orientations of QWP are shown in Fig. 3.10. Surprisingly, the effect is striking! To understand how such a tiny deviation could lead to such a dramatic effect on the results where the NRMSEs for the reconstructed amplitude and phase over 1 ns already reach about 38% and 41%, respectively, it is instructive to look at the Taylor expansions of the output signals of the photodetector around  $0^\circ$  and  $90^\circ$ .

To derive the Taylor expansion, Eqs. (3.10) and (3.11a) are combined to obtain, after some trigonometric transformations:

$$I_\psi = \frac{r_0^2 E_1^2}{2} [3 - \cos 4\psi + (1 - \sin 4\psi - \cos 4\psi)\rho(t) \cos \varphi_r(t) - 2 \cos 2\psi \rho(t) \sin \varphi_r(t)]. \quad (3.23)$$

Using the facts that:

$$\frac{\partial^n \cos 4\psi}{\partial \psi^n} = 4^n \cos \left( 4\psi + n \frac{\pi}{2} \right), \quad (3.24a)$$

$$\frac{\partial^n \sin 4\psi}{\partial \psi^n} = 4^n \sin \left( 4\psi + n \frac{\pi}{2} \right), \quad (3.24b)$$

$$\frac{\partial^n \cos 2\psi}{\partial \psi^n} = 2^n \cos \left( 2\psi + n \frac{\pi}{2} \right), \quad (3.24c)$$

the following simple expressions of the derivatives of  $I_\psi$  are obtained:

$$\frac{\partial^{2n+1} I_\psi}{\partial \psi^{2n+1}}(\psi = 0^\circ) = \frac{\partial^{2n+1} I_\psi}{\partial \psi^{2n+1}}(\psi = 90^\circ) = -2 \times 16^n r_0^2 E_1^2 \rho(t) \cos \varphi_r(t) \quad \forall n \in \mathbb{N}, \quad (3.25a)$$

$$\frac{\partial^{2n} I_\psi}{\partial \psi^{2n}}(\psi = 0^\circ) = -\frac{r_0^2 E_1^2}{2} [16^n + 16^n \rho(t) \cos \varphi_r(t) + 2 \times 4^n \rho(t) \sin \varphi_r(t)] \quad \forall n \in \mathbb{N}^*, \quad (3.25b)$$

$$\frac{\partial^{2n} I_\psi}{\partial \psi^{2n}}(\psi = 90^\circ) = -\frac{r_0^2 E_1^2}{2} [16^n + 16^n \rho(t) \cos \varphi_r(t) - 2 \times 4^n \rho(t) \sin \varphi_r(t)] \quad \forall n \in \mathbb{N}^*. \quad (3.25c)$$

Finally, the previous expressions allow the following presentation for the Taylor expansions of the outputs of the balanced photodetector  $s_\psi$  around  $0^\circ$ :

$$\begin{aligned} s_{0^\circ+\Delta\psi} = s_{0^\circ} - \frac{r_0^2 E_1^2}{2} \left\{ \sum_{n=1}^{+\infty} \frac{16^n (\Delta\psi)^{2n}}{(2n)!} \right. \\ \left. + \rho(t) \cos \varphi_r(t) \left[ \sum_{n=1}^{+\infty} \frac{16^n (\Delta\psi)^{2n}}{(2n)!} - 4 \sum_{n=0}^{+\infty} \frac{16^n (\Delta\psi)^{2n+1}}{(2n+1)!} \right] \right. \\ \left. - 2\rho(t) \sin \varphi_r(t) \sum_{n=1}^{+\infty} \frac{4^n (\Delta\psi)^{2n}}{(2n)!} \right\}, \end{aligned} \quad (3.26)$$

and around  $90^\circ$ :

$$\begin{aligned} s_{90^\circ+\Delta\psi} = s_{90^\circ} - \frac{r_0^2 E_1^2}{2} \left\{ \sum_{n=1}^{+\infty} \frac{16^n (\Delta\psi)^{2n}}{(2n)!} \right. \\ \left. + \rho(t) \cos \varphi_r(t) \left[ \sum_{n=1}^{+\infty} \frac{16^n (\Delta\psi)^{2n}}{(2n)!} - 4 \sum_{n=0}^{+\infty} \frac{16^n (\Delta\psi)^{2n+1}}{(2n+1)!} \right] \right. \\ \left. + 2\rho(t) \sin \varphi_r(t) \sum_{n=1}^{+\infty} \frac{4^n (\Delta\psi)^{2n}}{(2n)!} \right\}. \end{aligned} \quad (3.27)$$

As  $\rho(t) \ll 1 \forall t$ , the first term in the brackets will be prevailing over the two others, which will have the main effect to upshift or downshift by a constant value the expected signals at  $0^\circ$  and  $90^\circ$ . Such a tiny deviation from the orientations of QWP are practically inevitable. It can be understood from the previous analysis that removing the mean value of the output signal could allow to recover more acceptable results, as it can be seen in

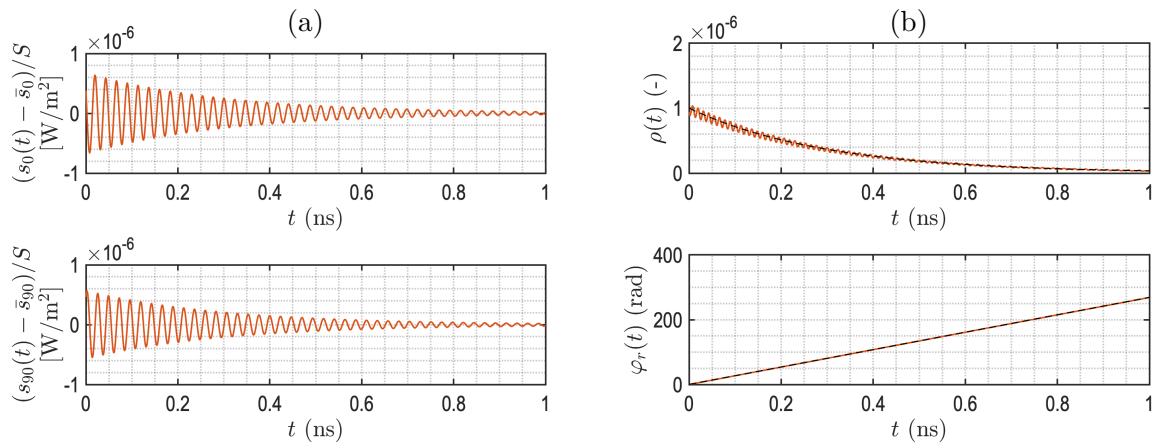


Figure 3.11 – Results of the compensation of the effect of QWP misorientation for a homogeneous sample after subtraction of the mean value of the output signal of the photodetector: (a)  $(s_{0^\circ}(t) - \bar{s}_{0^\circ})/S$  (top) and  $(s_{90^\circ}(t) - \bar{s}_{90^\circ})/S$  (bottom) as a function of pump-probe delay, (b)  $\rho(t)$  (top) and  $\varphi_r(t)$  (bottom) as a function of pump-probe delay, where  $\bar{s}$  stands for the mean value of  $s(t)$ . In (b), the set temporal variations of  $\rho(t)$  and  $\varphi_r(t)$  are the black dashed lines, while the calculated ones from the noisy signals in (a) are the orange solid lines.

Fig. 3.11, where the mean value has been removed from both output signals obtained this time with  $\psi = 5^\circ$  and  $\psi = 85^\circ$ . Despite this large deviation, the NRMSEs for the reconstructed amplitude and phase over 1 ns are of about 2.5% and 0.04%, respectively, which is far better than previously.

The previous analysis has allowed to propose a solution in order to avoid inconveniences due to a misorientation of QWP. The next section is now meant to summarize the different effects discussed in this section and to propose some solutions to limit them.

### 3.5 Summary of the listed factors influencing the results and few solutions to limit them

In the previous section 3.4, few factors leading to a deviation of the results from that of the ideal case where the only contribution to the output signal of the photodetector is the acoustic contribution have been listed. These factors could be grouped in two categories: (i) experimental and (ii) human factors. In the former case, we have discussed the effect of thermal background, of sample properties variations during the measurement, and of measurement noises. In the later case, the effect of misbalancing the reference and probing electric field amplitudes and that of a misorientation of QWP have been illustrated.

Although human factors might be diminished by precise and carefully-adjusted settings, small deviations from the ideal cases are unavoidable. To compensate for such deviations, the output signals  $s_{0^\circ}$  and  $s_{90^\circ}$  should be processed prior their use to extract

$\rho(t)$  and  $\varphi_r(t)$ . As discussed in the end of the subsection 3.4.6, removing the mean value of both output signals allows to reduce the effect of a QWP misorientation. Misbalancing the reference and probing electric field amplitudes mainly influences the reconstruction of  $\rho(t)$ , as seen in the subsection 3.4.2. Filtering out this effect *a posteriori* is a complicated option as it would imply a very good estimate of  $\varphi_r(t)$  in order then to find the multiplicative factor  $\frac{E_2^2 - E_1^2}{E_1^2}$  in Eq. (3.19) through a minimization algorithm. As the misbalancing of  $E_1$  and  $E_2$  will never be the only deviation from the ideal case at play, this *a posteriori* processing might lead to worse reconstruction than without. Yet, the results in the case of a misbalancing shown in Figs. 3.4 and 3.5 were obtained for  $E_2/E_1 = 50\%$ . For sure, such a large misbalancing can be avoided practically to reach a relative ratio  $(E_2 - E_1)/E_1$  of at least  $\pm 5\%$ , which in turn corresponds to a NRMSE for the reconstructed  $\rho(t)$  of less than 1%, where all other parameters are that of the ideal case (see Fig. 3.12 showing the NRMSE where the ratio  $E_2/E_1$  spans from 1% to 200%).

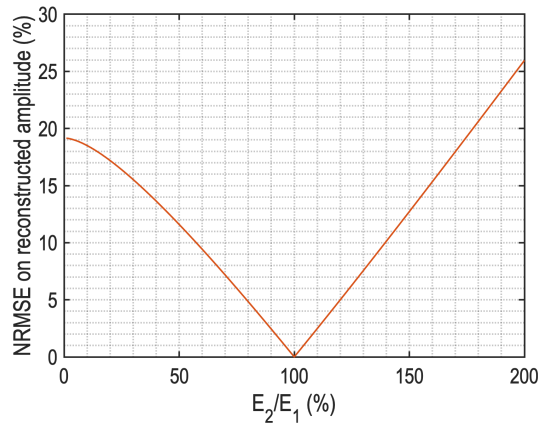


Figure 3.12 – Normalized root mean squared error (NRMSE) for the reconstructed  $\rho(t)$  as a function of the ratio  $E_2/E_1$  spanning from 1% to 200%, *i.e.*,  $(E_2 - E_1)/E_1$  spanning from -99% to 100%.

Limiting the effects of experimental factors is less straightforward, yet few solutions could help. With a careful alignment of pump and probe laser spots, the use of a synchronous detection with the help of an acousto-optic modulator modulating the pump pulse intensity at a hundreds kHz or fewMHz fixed frequency and a lock-in amplifier (see Fig. 2.2), together with hundreds averaging, reduces the measurement noises, although reaching a SNR better than +20 dB remains challenging, if ever possible. Yet, filtering out the high-frequency noise by signal processing is usually possible and will be illustrated in the next section.

As previously discussed, avoiding sample properties variations between the two subsequent measurements of  $s_{0^\circ}$  and  $s_{90^\circ}$  is mandatory. This necessity seems to preclude any measurement of transient changes of sample due to, for example, chemical reactions or external actions. Yet, the characteristic time of such sample transformations might be large enough to allow their measurements by ultrafast optical interferometry. To do so,

the pump-probe setup should be based on an asynchronous optical sampling to perform the pump-probe time delay, instead of on the slow scanning of a mechanical delay line, and the output signals  $s_{0^\circ}$  and  $s_{90^\circ}$  should be acquired in parallel by using two balanced photodetectors, which would require an additional calibration step to compensate the difference in detector sensitivity and would reduce by twice the amount of light reaching the photodetector imposing additional averagings to compensate the lowering of the SNR.

Last but not least, the effect of thermal background is the most difficult to avoid. Experimentally, this effect might be limited by two means.

The first mean is to design a specific configuration for the experiments where only the acoustic contribution is probed by the probe pulses. It can be achieved for instance by using a specifically designed opto-acoustic generator made of a thermal sink substrate transparent to the pump laser wavelength and an absorbing metal layer deposited on its surface [193]. With such an opto-acoustic generator, if the sample of interest is on top of the metal layer and if the pump laser is focused on the bottom interface between the substrate and the metal layer, the heat effect due to the pump pulse absorption can be confined near the substrate/metal interface. To do so, the metal layer should be thick enough so that the thermal field does not reach the top surface of the layer but thin enough for the acoustic pulse not to be attenuated too much when reaching the top surface. Additional parameters should be taken care of while preparing such a design, such as the choice of the metallic material and the substrate material in terms of acoustic impedance to avoid layer resonances and, if possible, to limit the impedance mismatch between the metal layer and the sample at the same time in order to maximize the acoustic pulse transmission from the metal to the sample.

The second mean would be to rearrange the constructed interferometer in order to set the lengths of the Sagnac arms around the sample to be closer to each other. This would provide the opportunity to measure directly the time derivative of the transient optical field reflectivity by two probe laser pulses with a short delay between them, instead of the numerical differentiation of its measured phase. This experimental differentiation would also acts as a high-pass filter, hence reducing the influence of the slowly-varying thermal background on the measurement. As a side note, this experimental differentiation might also reduce the effect of measurement noises that could limit the bandwidth of measurement when such differentiation is done numerically, *i.e.*, in post processing, because numerical differentiation exacerbates high-frequency noises.

While following one or several of the previous listed solutions, it is expected that the results will still deviate from the ideal case and further post-processing of the signals  $s_{0^\circ}$  and  $s_{90^\circ}$  is then required to reach better reconstruction of  $\rho(t)$  and  $\varphi_r(t)$ , which is discussed and illustrated in the next section.

## 3.6 Signal processing method to reduce the influence of other-than-acoustic contributions

As discussed in sections 3.4 and 3.5, despite the best care taken to set the here-developed ultrafast Sagnac interferometer, deviations from the ideal case are unavoidable. In this final section before experimentally testing the interferometer, it is proposed to use the developed model of the output signals of the balanced photodetector introduced in section 3.3 with realistic deviations from the ideal case in order to propose a signal processing procedure to limit the influences of unwanted factors and to discuss the limits of this procedure.

In this section, the choice of the material is restricted to a homogeneous sample of GaAs, with constant  $v_{ac} = 4730 \text{ mm ns}^{-1}$  and constant refractive index  $n = 3.6835$ . It is assumed that those properties remain constant for the two subsequent measurement with the interferometer, *i.e.* for orientation of the QWP theoretically at  $\psi = 0^\circ$  and  $\psi = 90^\circ$ . The deviation from those orientations are assumed small but not absent and the actual angles are considered to be  $\psi = 0.5^\circ$  and  $\psi = 89.5^\circ$ . The misbalance between the reference and probing electric field amplitudes is  $E_1 = 1 \text{ V m}^{-1}$  and  $E_2 = 0.95E_1 = 0.95 \text{ V m}^{-1}$ . The SNR, defined by using spectral power of the acoustic part of the signal, is set at 10 dB and, last but not least, the thermal background is set as in subsection 3.4.3 (Eq. (3.20)):  $A_b = -2 \cdot 10^{-5}$ ,  $\varphi_b = \pi/6$  and  $\tau_b = 0.5 \text{ ns}$ . The amplitude and the decay time of the acoustic contribution to the transient optical field reflectivity are set to  $A = 10^{-6}$  and  $\tau = 0.3 \text{ ns}$ . With those parameters, two cases are considered for the analysis: (i) the thermal background is first not considered, in order to analyze the influences of all other contributions (misbalanced amplitude, QWP misorientation, noises), (ii) the thermal background is added to the previous contributions. The output signals for both cases are shown in Fig. 3.13: (a) without and (b) with taking into account the thermal background.

There is no need to compute the reconstructed  $\rho(t)$  and  $\varphi_r(t)$  without applying any processing as it has already been demonstrated that for a tiny QWP misorientation, the reconstruction is impossible. First, if the processing proposed to correct the QWP orientation is applied, *i.e.*, removing the mean value from  $s_{0^\circ}(t)$  and  $s_{90^\circ}(t)$ , it can be seen in Fig. 3.14 that the reconstruction for  $\rho(t)$  and  $\varphi(t)$  are better without the thermal background than with. Yet, in the case without thermal background, the NRMSEs are of 8.5% and 9.7% for  $\rho(t)$  and  $\varphi_r(t)$ , respectively. These NRMSEs are in the expected range and might be attributed to the noise which has been shown (see Fig. 3.9) to deteriorate the reconstruction the most compared to the misbalanced amplitudes and QWP misorientation. Indeed, if noise is removed from the model, the NRMSEs decrease to 1.3% and 0.01% for  $\rho(t)$  and  $\varphi_r(t)$ , respectively. To remove the noise, a low-pass filter can be used. By applying an infinite impulse response (IIR) low-pass filter of order 6 with a passband

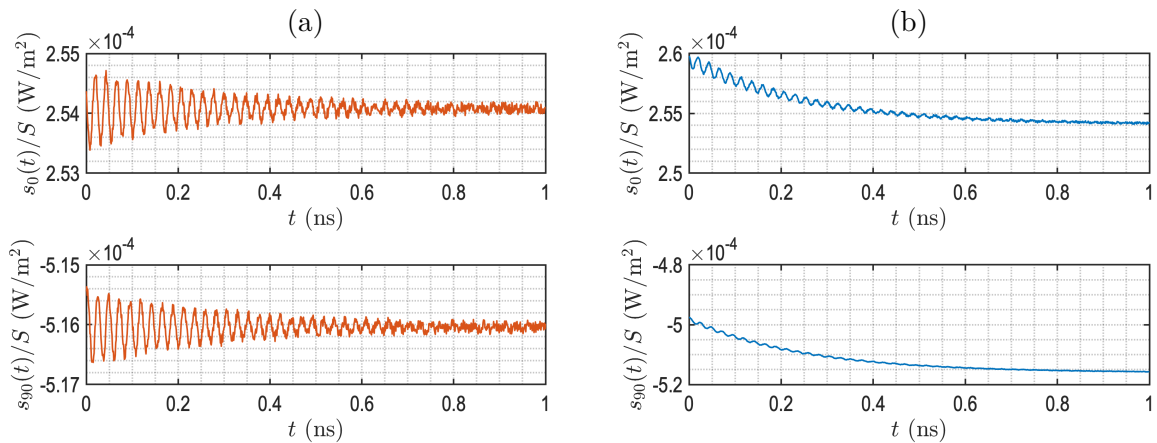


Figure 3.13 – Real-case simulated output signals  $s_0(t)/S$  (top) and  $s_{90}(t)/S$  (bottom) for a homogeneous sample: (a) misbalanced amplitude, QWP misorientation and noises are taken into account, (b) the thermal background is added to all the previous « poisoning » effects.

frequency set to 100 GHz and a passband ripple at 0.2 dB, the noise above 100 GHz is reduced and the NRMSEs drop down to 4.7% and 2.5% for  $\rho(t)$  and  $\varphi_r(t)$ , respectively.

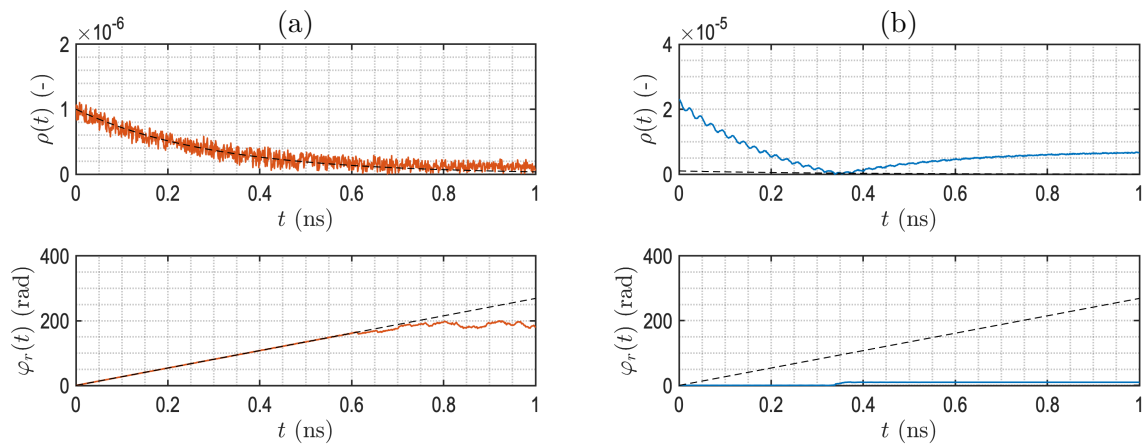


Figure 3.14 – Results of  $\rho(t)$  (top) and  $\varphi_r(t)$  (bottom) as a function of pump-probe delay after subtraction of the mean value of the output signals of the photodetector: (a) without and (b) with accounting for the thermal background. The set temporal variations of  $\rho(t)$  and  $\varphi_r(t)$  are the black dashed lines, while the calculated ones are the orange (a) and blue (b) solid lines.

Since the thermal background is not always a simple decaying exponential function, it is usually removed by using either a polynomial fit or a smoothing function. In the latter case, a local regression is applied by using weighted linear least squares and a first degree polynomial model in a moving average window spanning 50 points, *i.e.*, 50 ps, to smooth  $s_0(t)$  and  $s_{90}(t)$  before applying the low-pass filter and removing the remaining mean value, if any. The results following this process are shown in Fig. 3.15 where the improvement on the reconstruction in the case with the thermal background can be clearly

seen [Fig. 3.15(b)]. The NRMSEs in the case with the thermal background are of 4.7% and 2.4% for  $\rho(t)$  and  $\varphi_r(t)$ , respectively, while they are of 5.1% and 3%, respectively, for the case without the thermal background. Therefore, it can be seen that the smoothing is improving the accuracy of the reconstruction when the thermal background is present, whereas it is deteriorating the reconstruction when the thermal background is absent. The same conclusion could be drawn with a polynomial fit. In both cases, the parameters to remove the background, size of the widow and method for the smoothing or order of the polynomial function for the fit, are of utmost importance and should be chosen with great care. Yet, there is no precise rules to choose them, apart from a try and error method. In both cases, these methods can be seen as a way to high-pass filter the data.

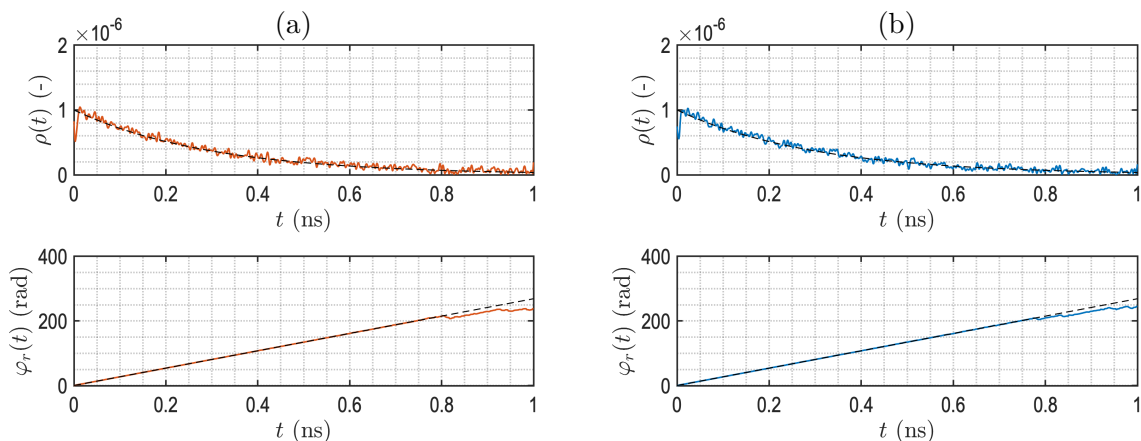


Figure 3.15 – Results of  $\rho(t)$  (top) and  $\varphi_r(t)$  (bottom) as a function of pump-probe delay after smoothing, low-pass filtering and subtraction of the mean value of the output signals of the photodetector: (a) without and (b) with accounting for the thermal background. The set temporal variations of  $\rho(t)$  and  $\varphi_r(t)$  are the black dashed lines, while the calculated ones are the orange (a) and blue (b) solid lines.

The drawbacks of filtering the data, by any means, is that the signal will be cleaner but distorted, which is something to avoid in this case as these two signals are then added and subtracted to compute  $\rho(t)$  and  $\varphi_r(t)$ . Since there is no reason for the noise to be the same for  $s_{0^\circ}(t)$  and  $s_{90^\circ}(t)$ , the results of the distortion will be different, exacerbating the deviation of the reconstructed  $\rho(t)$  and  $\varphi_r(t)$  from the expected ones. In any case, because of this deviation and of the remaining noise and oscillations inevitably present in the reconstructed  $\varphi_r(t)$ , the time differentiation needed to obtain the time variations of the product  $n(t)v_{ac}(t)$  should be done with great care and using advanced differentiation techniques such as smoothing followed by finite difference calculation, local approximation with linear models, Kalman filtering based methods or total variation regularization methods [194], which has not been done during this PhD work. Hence, in the next section where experiments are finally performed, the reconstruction will be, as in this and the previous sections, stopped at the step of the reconstruction of  $\rho(t)$  and  $\varphi_r(t)$ .

## 3.7 Time-domain Brillouin scattering measurements on a homogeneous GaAs wafer via ultrafast optical interferometry

In this last section of the chapter before the conclusion, it is finally proposed to perform time-domain Brillouin scattering measurements on a homogeneous sample of GaAs via ultrafast optical interferometry. After the experimental setup configuration and sample presentation, the results are shown, treated with the signal processing procedure discussed in section 3.6 and used to compute  $\rho(t)$  and  $\varphi_r(t)$ . A discussion analyzing the results and how they can be improved concludes this section.

### 3.7.1 Configuration of the experimental setup and presentation of the sample

The experimental configuration of the developed setup used in the experiments presented in the following is the one presented in chapter 2 in Fig. 2.2. Two set of measurements will be shown and discussed. For the first one, the following parameters were set:

- the pump and probe powers were both of 4 mW,
- the modulation frequency of the pump laser intensity was 400 kHz,
- the focusing objective lenses in the probe path were M Plan APO SL 20X (378-810-3) from Mitutoyo, with a working distance (WD) of 30.5 mm, a focal length of 10 mm and a numerical aperture (NA) of 0.28,
- the focusing objective lens of the pump laser was a M Plan APO 20X (378-804-3) from Mitutoyo, with a WD of 20 mm, a focal length of 10 mm and a NA of 0.42,
- the reference and probing electric fields reaching the surface of the sample were p-polarized,
- the probe light incidence angle  $\theta_i$  was  $60^\circ$ .

For the second set of measurements, the following parameters were set:

- the pump and probe powers were of 4 mW and 3 mW, respectively,
- the modulation frequency of the pump laser intensity was 200 kHz,
- the focusing objective lenses in the probe path were M Plan APO SL 20X (378-810-3) from Mitutoyo, with a working distance (WD) of 30.5 mm, a focal length of 10 mm and a NA of 0.28,
- the focusing lens of the pump laser was a 1 inch-diameter plano-convex converging lens of 75 mm-focal length,
- the reference and probing electric fields reaching the surface of the sample were s-polarized,

— the probe light incidence angle  $\theta_i$  was  $45^\circ$ .

For both sets of measurements, the fundamental laser wavelength of the Tsunami laser cavity was set to 810 nm (probe), hence the pump wavelength was 405 nm. Beam diameter at  $1/e^2$  is of about 2 mm. From the previous parameters, we can estimate the focus spot diameter of the probe beam to have been of about 5-6  $\mu\text{m}$  at  $1/e^2$  (in both cases), and that of the pump beam to have been of about 2.5-3  $\mu\text{m}$  in the first case, whereas it was of about 20  $\mu\text{m}$  in the second case.

The tested sample was, in both sets of measurements, a piece of a (100) GaAs wafer of 0.5 mm in thickness. The sample was supposedly homogeneous, with an expected acoustic velocity of the longitudinal acoustic mode of  $v_{ac} = 4711 \text{ nm ps}^{-1}$  (calculated from the elastic constants in Ref. [195]) and the same expected refractive index of  $n = 3.6381$  at 810 nm [196]. Note that earlier, Aspnes et al. had reported an experimental value of  $n = 3.6769$  at 810 nm light wavelength [197]. Since the reflection coefficient in amplitude of the probe light electric field at the free surface of the sample,  $r_0$ , depends on the polarization and on the angle of incidence  $\theta_i$ , it is instructive to plot  $r_0$  as a function of  $\theta_i$  for the p-polarized and s-polarized light. In Fig. 3.16, it can be seen that the amplitude  $|r_0|$  increase with  $\theta_i$  for a s-polarized light, while it is the opposite for a p-polarized light up to about  $74.6^\circ$ . It means that the amount of light reaching the acoustic pulse inside the bulk of the material will be less where the light polarization is perpendicular to the plane of incidence (s), as in the second set of measurements. It also means that the amount of light reflected on the stationary free surface and used for heterodyning the tiny amount of light scattered by the acoustic pulse will be less where the light polarization is parallel to the plane of incidence (p), as in the first set of measurements.

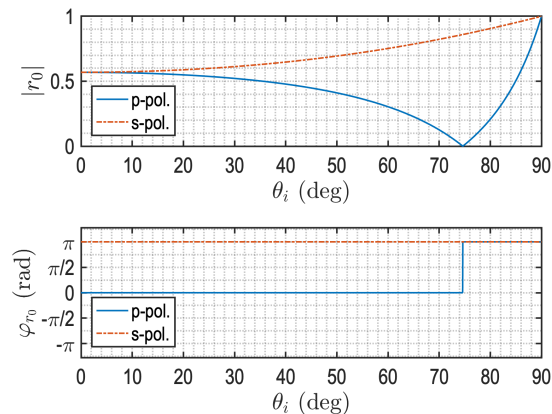


Figure 3.16 – Amplitude (top) and phase (bottom) of the reflection coefficient in amplitude of the probe light electric field at the free surface of a GaAs sample,  $r_0$ , as a function of the angle of incidence  $\theta_i$  for an electric field p-polarized (blue solid lines) and s-polarized (orange dashed-dotted lines).

### 3.7.2 Results

The output signals of the photodetector obtained in the first set of experiments, with the reference and probing beams being p-polarized and at an incidence angle of  $60^\circ$ , are shown in Fig. 3.17(a). Those of the second set of experiments, with the reference and probing beams being s-polarized and at an incidence angle of  $45^\circ$ , are shown in Fig. 3.17(b) with the same vertical scale. It is clearly noticeable from these figures that the signals obtained in the first measurements present both a larger absolute signal amplitude and a larger amplitude of the Brillouin oscillation than the signals obtained in the second set of measurements. The decrease in the absolute amplitude, while according to the light polarization a global increase in the second case could have been expected since  $|r_0|^2$  is higher in that case, might be explained by a less efficient generation in the second case than in the first case, which is mainly ascribed to the change in the optical focusing element for the pump laser beam which has a focal length of 10 mm in the first case, whereas it has a focal length of 75 mm in the second case: the pump intensity at the free surface of the GaAs sample is hence of about 60 times larger in the first case than in the second one, which is not compensated by the increase of  $|r_0|^2$  in the second case compared to the first one that is about 5 times. It is also noticeable that the amplitude of the Brillouin oscillation that are less in the second case than in the first case. This can be explained, on the one hand, by the fact that, in GaAs, the photoelastic coefficient  $p_{11}$  at play in the detection for an p-polarized light (first case) is slightly larger than the photoelastic coefficient  $p_{12}$  at play in the detection for a s-polarized light (second case). On the second hand, it should not be forgotten that the oscillation amplitude  $\rho(t)$  are also proportional to  $t_{01}t_{10}/r_0 = (1 - r_0^2)/r_0$  (see Eq. (13) in Ref. [17] after simplification), where  $t_{ij}$  is the complex transmission coefficient in field amplitude from medium  $i$  to medium  $j$  where medium 0 is air and medium 1 is GaAs. This factor is more than three times larger in the first case than in the second.

The raw signals are then processed as proposed in the section 3.6, that is to say by removing the background with the presented smoothing procedure, followed by applying the low-pass filter and finally removing the remaining mean value. Note that, prior to apply this whole procedure and because a perfect balancing of both channel (« + » and « - ») of the photodetector is not easy to keep for a long time, the mean value of each signal before  $t = 0$  ns is subtracted to the complete signal. The signals after applying the signal processing procedure,  $\tilde{s}_{0^\circ}(t)$  and  $\tilde{s}_{90^\circ}(t)$ , are shown in Fig. 3.18(a) for the first set of measurements and in Fig. 3.18(b) for the second one. The vertical scale is again the same but set such that the oscillations are visible. Just after  $t = 0$  ns, the oscillations due to the probe light interaction with the acoustic pulse are mixed with the background still remaining after the processing (that is also present before  $t = 0$  ns) and hence cannot be exploited. After  $t = 0.095$  ns, it is considered that only the Brillouin oscillations remained

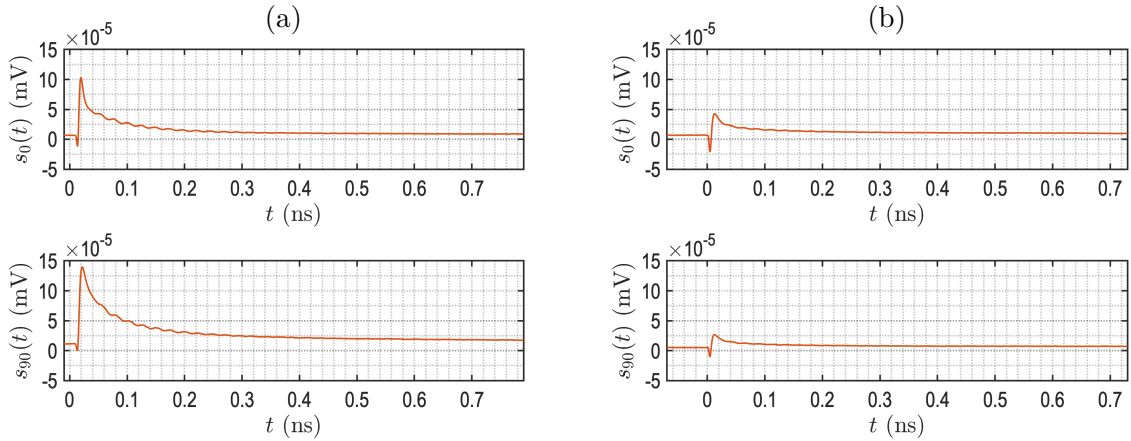


Figure 3.17 – Raw experimental signals for (a) the first set of measurements [ $\theta_i = 60^\circ$  and p-polarized light] and (b) the second set of measurements [ $\theta_i = 45^\circ$  and s-polarized light]:  $s_{0^\circ}(t)$  (top) and  $s_{90^\circ}(t)$  (bottom).

and are hence further treated to reconstruct the time variations of  $\rho(t)$  and  $\varphi_r(t)$  up to  $t = 0.6$  ns where the oscillations have vanished completely.

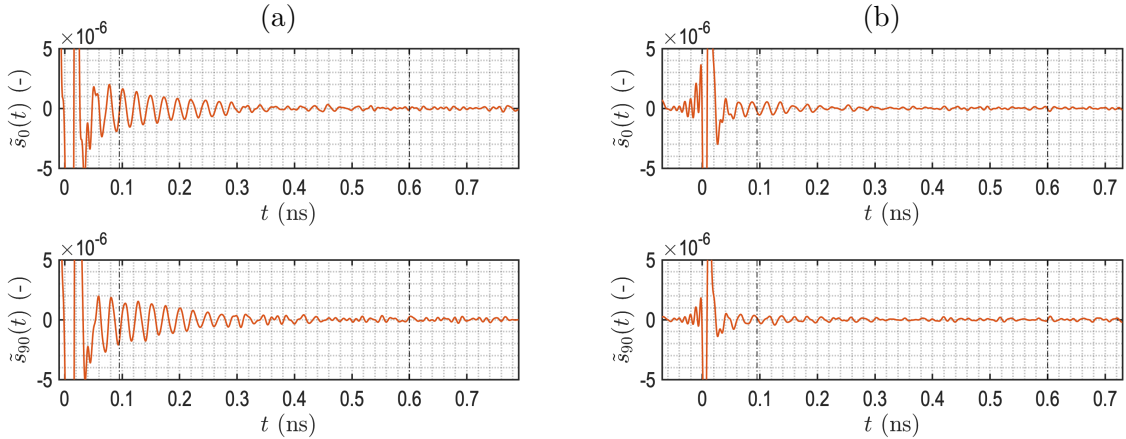


Figure 3.18 – Signals after applying the signal processing procedure (background removal, low-pass filtering and mean value removal) for (a) the first set of measurements [ $\theta_i = 60^\circ$  and p-polarized light] and (b) the second set of measurements [ $\theta_i = 45^\circ$  and s-polarized light]:  $\tilde{s}_{0^\circ}(t)$  (top) and  $\tilde{s}_{90^\circ}(t)$  (bottom). The vertical dotted-dashed lines in (a) and (b) stand for the time range shown in Fig. 3.19 for the reconstruction of  $\rho(t)$  and  $\varphi_r(t)$ .

Fig. 3.19 shows the results of the reconstruction of  $\rho(t)$  and  $\varphi_r(t)$  for  $t \in [0.095, 0.6]$  ns. From the experience gained during the study of the theoretical expectations (section 3.4), it is clear that the balancing of the reference and probing electric fields  $E_1$  and  $E_2$  is not done effectively in both cases, as it can be further understood from the spectrum of both reconstructed  $\rho(t)$  shown in orange solid lines in Fig. 3.20(a) and (b), respectively. It is obvious that the frequency peak in the spectrum of  $\rho(t)$  is at twice that of  $\tilde{s}_{0^\circ}$  in both cases, which is in agreement with the expression of  $\rho(t)$  derived in section 3.4.2 (Eq. (3.19)) in the analysis of the effect of misbalancing.

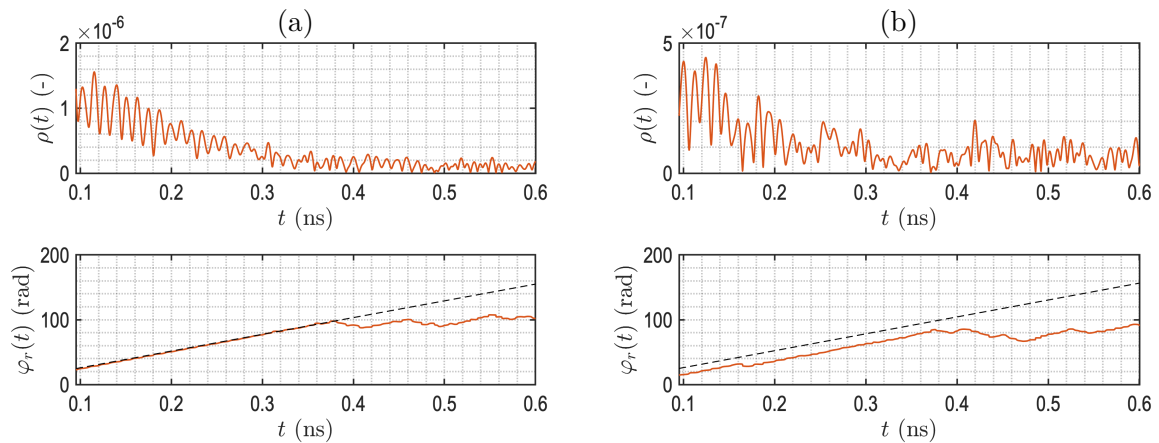


Figure 3.19 – Results of the reconstructed  $\rho(t)$  (top) and  $\varphi_r(t)$  (bottom) based on the processed signals shown in Fig. 3.18 for (a) the first set of measurements [ $\theta_i = 60^\circ$  and p-polarized light] and (b) the second set of measurements [ $\theta_i = 45^\circ$  and s-polarized light]. In (a) and (b), the dashed black lines depict the according expected temporal linear variation of  $\varphi_r(t)$  for the GaAs sample probed by 810 nm laser light, while the orange solid lines stand for the variations of  $\varphi_r(t)$  reconstructed from the experimental results.

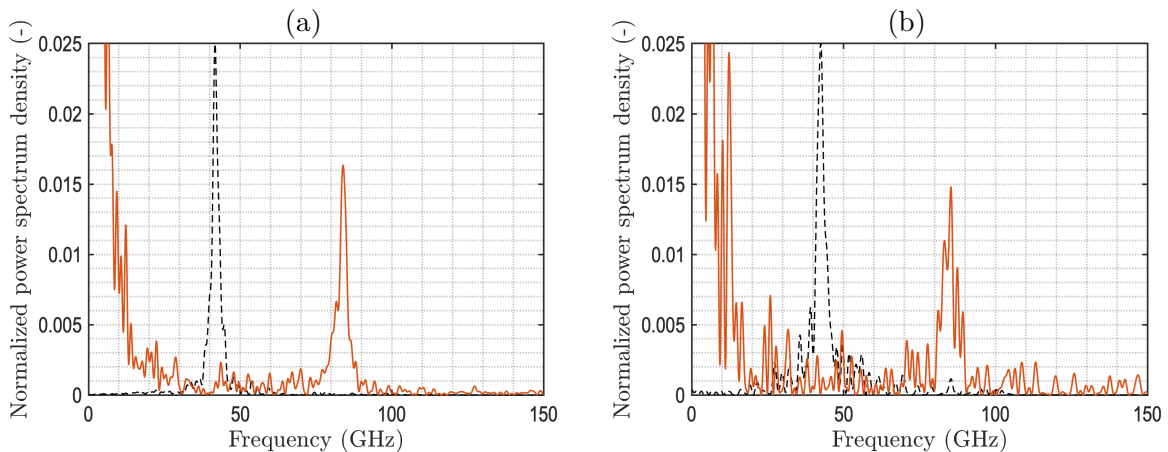


Figure 3.20 – Normalized power spectral density of the reconstructed  $\rho(t)$  (orange solid lines) compared to that of  $\tilde{s}_{0^\circ}$  (black dashed lines) for (a) the first set of measurements [ $\theta_i = 60^\circ$  and p-polarized light] and (b) the second set of measurements [ $\theta_i = 45^\circ$  and p-polarized light].

Despite the bad reconstruction of  $\rho(t)$ , a fair reconstruction of the expected linear temporal variation of  $\varphi_r(t)$  is achieved in both cases up to a limit in time where the noise level is higher than that of the signal and hence the reconstruction deviates from the expected linear trend. The NRMSE for  $t \in [0.095, 0.38]$  ns is 1.9% (1.3%) in the first case and 6.6% (7.1%) in the second case assuming  $n = 3.6381$  ( $n = 3.6769$ ). Note that the larger NRMSE in the second case is explained by the phase accident around 0.17 ns, surely related to noise, which is visible in the raw (after zooming, not shown) and filtered signals [Fig. 3.18(b)], as it leads to a systematic error for all  $t > 0.17$  ns.

### 3.7.3 Discussion

The results shown in the previous section have demonstrated the good functioning of the constructed ultrafast interferometer. The expected linear trend of  $\varphi_r(t)$  in the case of a homogeneous sample has been recovered with an acceptable deviation from the theory (bottom part in Fig. 3.19), and that in the best and worst case scenario, that is to say with good pump focusing and p-polarized light, on the one hand, and with bad pump focusing and s-polarized light, on the other hand. The reconstructed  $\rho(t)$  is however inexploitable for the reason of misbalanced between the reference and the probing electric fields. From the spectrum shown in Fig. 3.20, it is tempting to filter out the oscillation with a dedicated low pass filter. The results of such a filtering of the reconstructed  $\rho(t)$  (top part in Fig. 3.19) with a low-pass filter (IIR low-pass filter of order 6 with a passband frequency set to 60 GHz and a passband ripple at 0.2 dB) are shown in Fig. 3.21. For both cases, the trend is not exponentially decaying but oscillations probably due to measurements noise still prevents the further use of this filtered reconstructed  $\rho(t)$  for sample characterization.

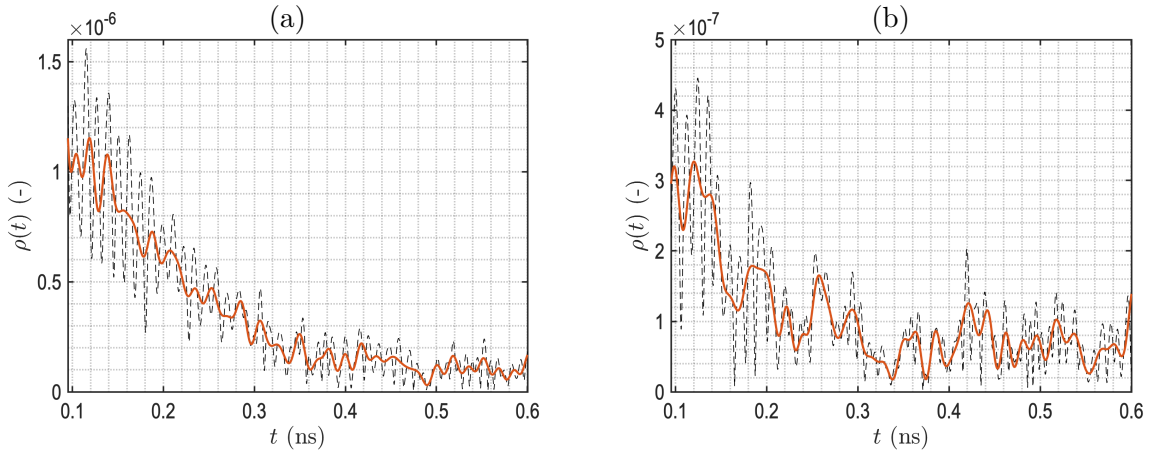


Figure 3.21 – Results of the low-pass filtering of the reconstructed  $\rho(t)$  for (a) the first set of measurements [ $\theta_i = 60^\circ$  and p-polarized light] and (b) the second set of measurements [ $\theta_i = 45^\circ$  and s-polarized light]. In (a) and (b), the dashed black lines depict the the initial  $\rho(t)$  before application of the low-pass filter.

As the reconstructed  $\varphi_r(t)$  are satisfying, it is proposed to differentiate them. Figure 3.22 shows  $\frac{1}{2\pi} \frac{\partial \varphi_r(t)}{\partial t}(t)$  as a function of time (top) and its normalized power spectrum density (bottom) for (a) the first set of measurements and (b) the second one. The numerical differentiation is done here with the simplest method possible. From the orange solid lines showing the results of such a differentiation, it is clear that, although the results is around the expected constant Brillouin frequency value, it deviates from it a lot. It is instructive to look at the spectral content of  $\frac{1}{2\pi} \frac{\partial \varphi_r(t)}{\partial t}(t)$  (bottom) where it is clear, especially in Fig. 3.22(a), that the main poisoning effect is here also the fact that the reference and probing electric field amplitudes are not equal, giving rise to this oscillating behavior at half the period of Brillouin oscillations. Filtering out this frequency by the same low-pass

filter used on  $\rho(t)$  (Fig. 3.21) allows to remove the influence of the reference and probing field misbalancing. The *absolute* RMSE in the case of the first set of experiments (best scenario of both sets) drops from 87% to 2.4% thanks to the filtering. Yet, the obtained results are not that good. The time derivative  $\frac{1}{2\pi} \frac{\partial \varphi_r(t)}{\partial t}(t)$ , expected to be constant and equal to the Brillouin frequency, is not constant but oscillates with time in a  $\pm 4$  GHz window around the Brillouin frequency, *i.e.* not with the best precision, excluding the possibility to evaluate with high precision the depth-profiling of material properties.

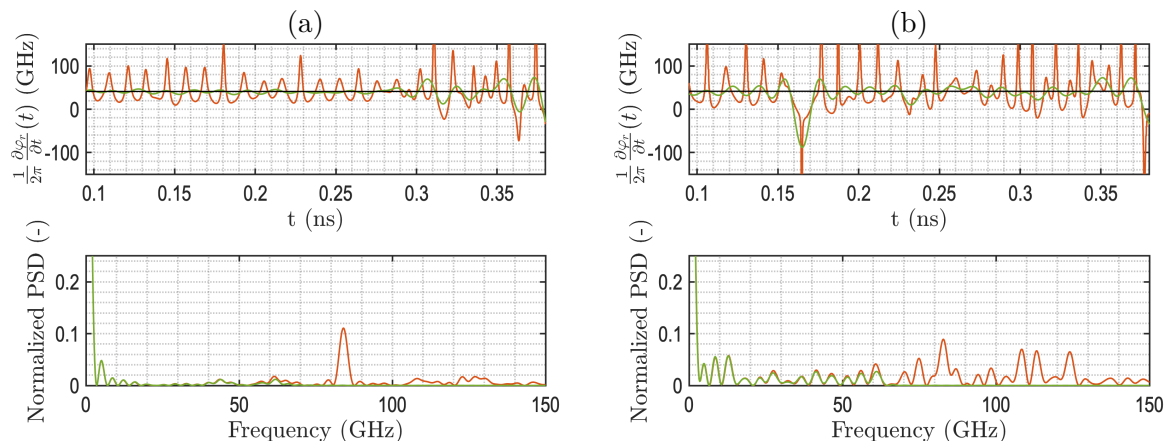


Figure 3.22 – (top) Differentiation of  $\varphi_r(t)$ ,  $\frac{1}{2\pi} \frac{\partial \varphi_r(t)}{\partial t}(t)$ , as a function of time and (bottom) its normalized power spectrum density (PSD) for (a) the first set of measurements [ $\theta_i = 60^\circ$  and p-polarized light] and (b) the second set of measurements [ $\theta_i = 45^\circ$  and s-polarized light]. In (a), the black solid horizontal lines depict the expected constant Brillouin frequency. In (a) and (b), the orange solid lines stand for the differentiation of the results shown in Fig. 3.19 (bottom) and the green solid lines depict the results of the same differentiation followed by a low-pass filtering.

Although rather pessimistic, the conclusions drawn from the first results obtained with the here-constructed ultrafast Sagnac interferometer are valuable. As expected from the theoretical analyses, the balancing of the reference and probing electric field amplitudes is demonstrated to be of utmost importance for precise depth profiling of material properties. In an inhomogeneous material, where the depth profile of material properties is unknown, this is mandatory because the above-proposed low-pass filtering to remove in a post-processing the effect of misbalancing will distort the reconstruction which will deviate from the actual distribution, of which the frequency content can potentially overlap with that of the effect of the misbalancing. Avoiding such effect of misbalancing could help in getting usable  $\rho(t)$  in order to achieve depth profiling of the photo-elastic coefficient. Last but not least, the previous comparison between the experiments done with a p-polarized or s-polarized probe light also draws attention to the importance of the choice of the probe polarization. Maximizing the part of the probe light transmitted to the bulk of the sample where it will be scattered by the propagating acoustic pulse is shown to allow larger Brillouin oscillation amplitudes in the measured signals, hence improving the

signal-to-noise ratio for the part of the signals that matters for depth profiling.

## 3.8 Chapter summary

In this chapter, a model of the probe light intensity reaching the « + » channel of the balanced photodetector has been derived and used to illustrate the effects of few factors leading to a deviation of the results from that of an ideal case where only the acoustic contribution would have been at play. We have analyzed the effects of thermal background, of sample properties variations during the measurement, and of noises, all being experimental factors, as well as the effects of a misbalancing of the reference and probing electric field amplitudes and of a misorientation of the quarter-wave plate. A signal processing procedure, aimed at reducing the influence of the previous factors, has then been proposed and described. The ultrafast Sagnac interferometer has finally been used to conduct experiments in a homogeneous sample of GaAs. These first experiments allowed to shed light onto two important aspects a user of such interferometer have to take care of, namely the achievement of the best balancing possible between the reference and probing electric field amplitudes and the choice of the probe light polarization to favor the amplitude of the signals part that matters for depth profiling: the Brillouin oscillation.

In the next chapter, it is now proposed to shortly list the future plans to improve the experimental setup and few possibilities of applications of the developed interferometer that were not tested in this PhD work, though interesting to perform.



# FUTURE PLANS AND PERSPECTIVES

## APPLICATIONS

---

This chapter is intended to give a view of the prospective applications and the conceptual solutions designed during the work with the actual configuration of the experimental setup. Each section is purposely short, but hopefully instructive enough to trigger interest for further researches exploiting the designed interferometric setup. While working with the setup, some improvement ideas were born. These concepts are presented at the beginning of the chapter. It is followed by experimental configurations that have not been tested during this PhD work but that could be of interest and hence are mentioned not to forget them. The chapter ends with a discussion on the experiments that are of certain general interest and that should be possible to conduct with the help of the here-proposed interferometric setup.

### 4.1 Possible improvements and modifications of the experimental setup

In order to ease further the use of the experimental setup or the use of the signals provided by it, few improvements and modifications are possible and now presented.

#### 4.1.1 Equipment replacement for the better precision and the space minimization

The experimental setup that was constructed during this work is relatively big, so manual work sometimes becomes complicated. While gaining more and more experience during the run of my PhD study, I had some concepts in mind that could allow to make the experimental setup much more user-friendly in ways of comfortable use. I have implemented the most important ones while re-building the interferometer to reach the configuration presented in Fig. 2.2. The pump path could also be improved compared to the current situation. Two ideas to do so are listed below for the sake of the next users of my setup.

1. The improvement of the pump positioning can be done with help of ST1XY-D/M -

XY (Thorlabs), that provides micrometer precision when performing the positioning of the first lens in 4f-system, but such upgrade will require the cage adapter as OC1-A30 from Newport.

2. Considering the experience with optical fiber, the pump light delivering system could also be planned to be based on optical fiber. The concept consists of a collimator mounted on an application-specific combination of linear translation platforms, which will deliver light to the specimen through the lens.

### 4.1.2 Optimization and automatization of the setup

Automatization of the depth-profiling measurement by the experimental setup allows to save time and simplify the process. A list below allows to find the improvements that could be introduced with the modifications that are required for.

- In order to reduce by two the amount of measurements and, at the same time, to surely reduce uncorrelated noise influence from the two subsequent measurements for  $0^\circ$  and  $90^\circ$  orientations of QWP, it is possible to add a second balanced photodetector (PD), as well as additional NPBS, QWP and POL. NPBS has to be installed before the entrance to the QWP-POL-PD system with QWP and POL being configured for getting one of the required intensities. Reflected light portion is directed onto the additional PD through the additional QWP and POL that are oriented for measuring the second intensity, required for the acoustic wave amplitude and phase extraction.
- In order to further reduce by two the amount of measurements and getting better stiffness of the setup in general, it is possible to construct an additional Sagnac interferometer with  $45^\circ$  angle of probe incidence (or any other else angle), as suggested by Matsuda [186]. To do so, the addition of a NPBS after the first POL is needed to split the light into two parts. The newborn beam has to be sent into another Sagnac interferometer, that has to be built and installed with a different probe incidence angle or else to send both reference and probing beams through the pump path for the interferometric detection at normal incidence. Both pairs of probing and reference beams have to be overlapped in space, but depending on the detection technique the time overlap could be shifted in time if the pump laser is set to have twice the repetition rate of that of the probe laser in order to avoid the unwanted interference of different probing/reference beams. Since the result of this modification is an additional probe that is measuring the same Brillouin signal but with different probe incidence angle, and if the previous step has been taken into account as well, the output of one measurement will provide sufficient data for the depth-profiling of studied material. Otherwise the experiment has to be conducted twice for the acoustic amplitude and phase extraction to be possible, and at least

twice again at two different incidence angles for splitting  $n$  and  $v_{ac}$  distribution..

- In order to get a 3D image of the sample material properties, a motorized linear translation stages allowing two dimensional scan of the sample in front of the fixed laser spots position has to be added. In that case, a great care should be taken in the alignment procedure to be sure that a movement of the sample in the plane of its free surface is not moving the pump and probe spots on the sample surface.

### 4.1.3 Use of the setup at different wavelengths

In some situations, it might be interesting to change the wavelength of the pump and/or the probe lasers. Doing so indeed can help in improving the generation and/or the detection efficiency by using photons with the required quantum of energy for efficient generation or with the probe wavelength maximizing the photo-elastic coefficient, for example. If the wavelength are slightly changed around the current situation (405 nm and 810 nm for pump and probe laser wavelengths, respectively), the current setup should still be able to work, providing some adjustments of the polarization optics. However, if the wavelengths drastically deviate from the current ones, few optical elements should be changed. Elements such as PBS, NPS and lenses are usually designed to work on a sufficiently broad range, typically 400-700 nm and 700-1100 nm, which should hence be alright even after the tuning of laser wavelengths. Polarization maintaining optical fibers can be broadband or designed for a single wavelength. In order to increase the versatility of the setup regarding laser wavelengths, the former should be chosen, although the range is usually less broad than for PBS and NPBS for example. Other optical elements such as QWP and HWP are usually designed to work at a given fixed wavelength. If the ability to use a wide range of wavelengths is aimed, zero-order mode QWP and HWP usually made of quartz should be changed by the more expansive solutions of achromatic waveplates made of crystalline quartz and magnesium fluoride or of a polymer film stack laminated between two N-BK7 glass plates.

### 4.1.4 Possibility to perform experiments with small incidence angles of the probe laser

The current experimental setup does not allow to work at small incidence angles when pump and probe are on the same side of the sample. This is due to the fact that the pump and probe objectives used for the focusing have large lateral dimensions, of the same order of their working distance and hence are touching each other on their side before reaching small incidence angles. To circumvent this limitation while keeping the ability to have good focusing (pump/probe spot size of 2-5  $\mu\text{m}$ ), it would be possible to design home-made objective systems to limit lateral footprints compared to commercial

objective lenses. For very small angles of incidence, it would also be possible to use the same focusing objective than the pump beam for focusing and collecting the probe light.

### 4.1.5 Optical differentiation

Last but not least, it could be of interest in order to avoid some limitations discussed in the previous chapter with the numerical differentiation of the phase to be able to extract the time derivative of  $\varphi_r(t)$  directly from measurements. By changing the length difference between the reference and probing beam paths in reducing it to  $\Delta t < 1$  ps, it would be possible, with both optical pulses, to probe the sample not anymore before and after the pump pulse arrival onto the sample but at two subsequent time after the pump pulse arrival time. In that case, the light intensity reaching the photodetector is not anymore sensitive only to the relative variation in the complex optical electric field reflectivity but also to its time derivative. Indeed, the probing ( $E_{1r}$ ) and reference ( $E_{2r}$ ) electric fields would be expressed in that case as:

$$E_{1r} = r'(t + \Delta t)E_1 \approx r'(t) + \Delta t \frac{\partial r'}{\partial t}(t)E_1, \quad (4.1a)$$

$$E_{2r} = r'(t)E_2, \quad (4.1b)$$

where  $\Delta t$  is the small time delay between the arrival times of both pulses at the sample surface and:

$$r'(t) = r_0 e^{i\varphi_0} \left( 1 + \rho(t) e^{i\varphi_r(t)} \right), \quad (4.2a)$$

$$\frac{\partial r'}{\partial t}(t) = r_0 e^{i\varphi_0} \left( \rho'(t) + i\rho(t) \frac{\partial \varphi_r}{\partial t}(t) \right) e^{i\varphi_r(t)}. \quad (4.2b)$$

Using Eqs. (3.10) and (3.11a)(a), (e)-(h), trigonometric identities and the assumption  $E_1 = E_2$  (equal amplitude of probing and reference electric field amplitudes), it can be shown at the first order in  $\rho(t) \ll 1 \forall t$  that the expression of the intensity reaching the « + » channel of the balanced photodetector in that case,  $I_\psi^{diff}$ , reads:

$$\begin{aligned} I_\psi^{diff} = \frac{r_0^2 E_1^2}{2} \{ & (1 + \cos 4\psi) (1 + 2\rho \cos \varphi_r) \\ & + \Delta t [(1 + \sin 4\psi - \cos 4\psi) (\rho' \cos \varphi_r - \rho \varphi_r' \sin \varphi_r + \rho \rho')] \\ & - 2 \cos 2\psi (\rho' \sin \varphi_r + \rho \varphi_r' \cos \varphi_r)] \} \end{aligned} \quad (4.3)$$

where the time dependence of  $\rho(t) \equiv \rho$  and  $\varphi_r(t) \equiv \varphi_r$  are implicit for the sake of compactness and their derivative with respect to time written as  $\rho'$  and  $\varphi_r'$ , respectively.

It therefore appears from the equation that 4 unknown functions have to be found now ( $\rho(t)$ ,  $\varphi_r(t)$  and their time derivative). Yet, from Eq. (4.3), it can be understood that

changing the QWP orientation angle  $\psi$  will only give access to 3 unrelated equations, all the other possible orientations being linear combinations of the chosen 3 orientations. Hence, to be able to solve the problem, another degree of freedom should be changed and could be the orientation of the polarizer, which allows to keep all unknown functions the same. However, it should be noted that the time variation of  $\rho(t)$  is usually (much) slower than the time variation of  $\varphi_r(t)$ . Assuming that  $\rho'(t) \ll \varphi_r'(t) \forall t$  removes one unknown from the equation and then the measurements at  $\psi = 0^\circ, 45^\circ, 90^\circ$  having the following expression:

$$I_{0^\circ}^{diff} = r_0^2 E_1^2 [(1 + 2\rho \cos \varphi_r) - \Delta t \rho \varphi_r' \cos \varphi_r], \quad (4.4a)$$

$$I_{90^\circ}^{diff} = r_0^2 E_1^2 [(1 + 2\rho \cos \varphi_r) + \Delta t \rho \varphi_r' \cos \varphi_r], \quad (4.4b)$$

$$I_{45^\circ}^{diff} = -r_0^2 E_1^2 \Delta t \rho \varphi_r' \sin \varphi_r, \quad (4.4c)$$

could be combined in order to extract the three unknown functions:

$$\frac{\partial \varphi_r}{\partial t}(t) = \frac{2}{\Delta t} \frac{I_{90^\circ}^{diff} - I_{0^\circ}^{diff}}{I_{90^\circ}^{diff} + I_{0^\circ}^{diff} - 2I_{ref}}, \quad (4.5a)$$

$$\varphi_r(t) = \mathcal{U} \left\{ \arctan \left[ -2 \frac{I_{45^\circ}^{diff}}{I_{90^\circ}^{diff} - I_{0^\circ}^{diff}} \right] \right\}, \quad (4.5b)$$

$$2r_0^2 E_1^2 \rho(t) = \sqrt{\left( I_{45^\circ}^{diff} \right)^2 + \left( \frac{I_{90^\circ}^{diff} - I_{0^\circ}^{diff}}{2} \right)^2} \frac{I_{90^\circ}^{diff} + I_{0^\circ}^{diff} - 2I_{ref}}{I_{90^\circ}^{diff} - I_{0^\circ}^{diff}}, \quad (4.5c)$$

where  $I_{ref} = r_0^2 E_1^2$ .

It is important to note that this should hence allow to extract directly the time derivative of  $\varphi_r(t)$  even from the same two subsequent measurements as before, as soon as the assumption  $\rho'(t) \ll \varphi_r'(t) \forall t$  holds true, which could avoid the issue of numerical differentiation discussed in chapter 3.

## 4.2 Two other possible configurations of the experimental setup

The design of the experimental setup with the use of optical fibers and a custom rotation mechanism allowed to achieve the required functionality. The aim of this section is to show the versatility of the experimental setup that is the result of the design choice. For the sake of simplicity, consider a case where only the pump and probing beams are involved, without the reference beam. The sample is fixed on top of the centering rod of the rotation mechanism. Thanks to this, the adjustment of the rotation stages does not affect the sample. In the following, it is also assumed that, after being focused and positioned on the sample surface, the pump beam remains fixed as well, unless otherwise

stated.

The angle of incidence of the probe beam can be changed by means of the two centered, yet independent, manual rotation stages. Rails, carrying the XYZ stages under the cage systems with optical elements (lens, half-wave plate and optical fiber collimator), are fixed to each platform. The rotation stages provides fine adjustment with 1 arc min ( $0.017^\circ$ ) resolution and the coarse adjustment range is  $360^\circ$ .

The studies, conducted as a part of this PhD, were conducted in the same manner, where the incident pump and probe as well as the reflected probe belong to the same hemisphere relative to the surface of the sample. Yet, the versatile setup provides other opportunities.

For example, while being set in reflectometric configuration, it is possible (and easy to settle) to perform measurements where the probe pulse transmitted through the sample is used to heterodyne the acoustically-scattered probe transmitted through the sample. Note that the probe can be incident, in choice, on the same or opposite sample side than the pump beam, the transmitted probe being then collected on the opposite or the same sample side than the pump beam, respectively. This configuration could be used, for example, to perform time-domain Brillouin scattering measurement in the case of very thin materials where the transmitted acoustically-scattered light could be forward scattered and/or backward scattered and later forward reflected from the front surface.

Another opportunity provided by the flexible setup is that it is fast to settle the beam probe paths so that the pump-probe experiments with pump and probe pulses incident on the opposite sides of the sample could be conducted. The advantage of this type of the arrangement is, for example, the suppression of the thermal background, depending on the thickness of the studied sample. The slow process of the heat dissipation is usually subtracted with the numerical methods in order to observe and study the laser-induced acoustic waves as we have seen in the previous chapter. Yet, good subtraction could be challenging and having the opportunity to just not measure it could be attractive because the physical absence of the thermal background allows to measure the acoustic signal directly. The method therefore simplifies signal processing and allows for a more accurate study of the nature of sound propagation in the medium.

### 4.3 Surface acoustic wave detection

Besides the use of the constructed optical instrument that has been discussed all along the last chapters, *i.e.*, the depth profiling by time-domain Brillouin scattering in inhomogeneous materials, another interesting application for this device offering an easy adjustment of the incident angle is to use it in order to detect surface acoustic waves (SAWs) by means of Brillouin scattering.

The schematic representation of the reflectometric configuration is depicted in Fig. 4.1

where an acoustic pulse is illustrated at the free surface of a sample with the probe light incident with an angle of incidence  $\theta_i$ . For the backward scattering of light by the SAW (Fig. 4.1), the possibility to vary the probe incidence angle plays a crucial role due to the momentum conservation law since, compared to the bulk waves, there will be no refraction coefficient that "stretches" the light wave vector projection on the axis that is unidirectional with the acoustic wave propagation. The SAW can also be considered as a moving Bragg mirror, that introduces a Doppler shift to the scattered light. In any case, the momentum conservation law would imply that:

$$q_{SAW} = 2k_i \sin(\theta_i), \quad (4.6)$$

where  $q_{SAW}$  is the SAW wavenumber and  $k_i \approx k_s$  are the incident (i) and scattered (s) probe light wavenumbers that are very close since the Brillouin shift is small relatively to the light frequency. The second fiber arm of the constructed device can then be advantageously used to provide a probe beam which will be incident from the right to the left and will be reflected from the surface with an angle of  $\theta_i$ . This reflected light will be collinear with the light scattered by the SAW and, hence, the heterodyning of the scattered light by the reflected light will be made possible.

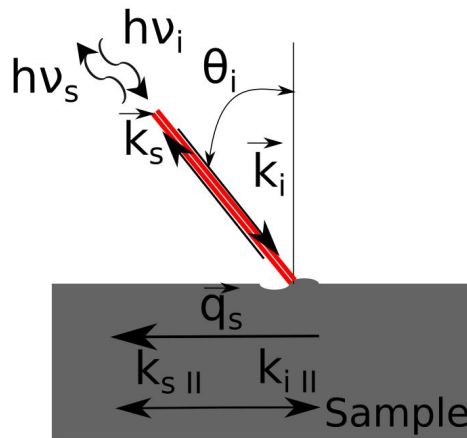


Figure 4.1 – Schematic representation of the light back-scattering by the SAW.

Future experimental steps require strengthening of the theoretical background on the SAW detection and solving of the phase-matching problem. For example, in the case of a SAW wavepacket at a central frequency of 7.4 GHz (acoustic wavelength of 405.4 nm) propagating along the surface at a phase velocity of 3 nm ps<sup>-1</sup>, with a probe light having a wavenumber of  $k_i = 7.76 \text{ rad } \mu\text{m}^{-1}$  ( $\lambda_{probe} = 810 \text{ nm}$ ), the incidence angle according to Eq. 4.6 that should allow the efficient detection of the SAW wavepackets by Brillouin scattering is  $\theta_i = 87.4^\circ$ . After the first experiments with the SAW in the GHz frequency range where Brillouin scattering could be expected, the experimentation with higher-frequency SAWs could also be conducted, but the theory of their (interferometric) detection would

need to be established.

## 4.4 Chapter summary

In this chapter, some improvement and modification ideas of the setup have been discussed in order to achieve faster measurement, to reduce noise influence, or to develop further the versatility of the interferometer. The possibility of the direct reconstruction of  $\frac{\partial \varphi_r}{\partial t}(t)$  by means of optical measurements, allowing to avoid numerical differentiation issues have also been discussed and theoretically proven that it is possible if the time variation of  $\rho(t)$  are slower than that of  $\varphi_r(t)$ . Then, two other possible configurations of the setup, not used in this work but potentially of interest have been presented. Finally a short discussion has introduced the possibility to use the interferometer in order to detect surface acoustic waves by Brillouin scattering means. All discussed points in this chapter constitutes short or mid-term perspectives for applications of the interferometer. Of course, the shortest perspective in the line of sight is the application of the interferometer to depth profiling of inhomogeneous sample, with the expectation that a better balancing of reference and probing electric field amplitudes will provide the opportunity to avoid spurious filtering of the detected signal or, worse, of the reconstructed  $\varphi_r(t)$ . The way how two measurements with the interferometer at two incidence angles should be combined/used to disentangle the depth profile of the refractive index and that of the acoustic velocity from the variation of the phase is given in Appendix D, since not used in this manuscript but of many interest for a potential future user.

# GENERAL CONCLUSION

---

Imaging and characterization of the materials spatial inhomogeneities is of extreme importance for understanding the possible limits in their functionalities, which could be reduced or enhanced relative to ideal homogeneous materials. With the continuous diminishing of the components scale in micro- and nano-electronics, as well as for the characterization of micro- and nano-crystalline materials or else animal/biological cells, the imaging techniques providing nanometers to sub-micrometers spatial resolution are required. This spatial resolution is also desirable for the evaluation of the material properties near the material surfaces and interfaces between different materials, which are never delta localized but are rather of finite width. Among the techniques potentially providing the required functionality, which are currently under the active developments, is the time-domain Brillouin scattering (TDBS), which combines ultrafast optics with the picosecond acoustics to achieve from sub-optical (sub-micrometric) to deeply sub-optical (nanometric) axial resolution (i.e., along the propagation direction of the picosecond acoustic pulse).

TDBS, which is also known as picosecond ultrasonic interferometry, is an all-optical experimental technique based on ultrafast lasers applied for generation and detection of coherent acoustic pulses on time durations of picoseconds and length scales of nanometers. In transparent materials, scattering of the probe laser beam by the coherent acoustic pulses traversing the material permits imaging of sample inhomogeneity, by evaluating the material property in the sequence of the coherent acoustic pulse positions. The transient optical reflectivity of the sample recorded by the probe beam as the acoustic nanopulse propagates in space contains information on the local acoustical, optical, and acousto-optical parameters of the material under study. The experimental method is based on a heterodyning where weak light pulses scattered by the coherent acoustic pulses interfere at the photodetector with probe light pulses of significantly higher amplitude reflected from various stationary interfaces of the sample. The TDBS technique was earlier applied for the imaging of ion-implanted and UV-cured materials, of the polycrystalline materials and vegetal/animal cells, of temperature and strain distributions inside the materials, as well as for the imaging of the coherent acoustic pulse transformation in homogeneous medium caused by its attenuation, focusing or nonlinearity.

This PhD thesis was devoted to the design, construction and experimental testing of a new TDBS instrument for the measurement of the sound velocity and optical refractive index distribution in spatially inhomogeneous transparent media with an axial resolution (along the depth) potentially controlled by the few-nanometers length of the coherent acoustic pulse and independent of probe light wavelength.

---

In chapter 1, a historical introduction on the discovery and first applications of the optoacoustic and acousto-optic effects that opened the field of research nowadays known as laser ultrasonics, the basis of the field dedicated to the study and the use of picosecond acoustics have been introduced. A discussion on the subsurface imaging and depth profiling has then followed with a particular emphasis on the use of the frequency-domain and time-domain Brillouin scattering techniques to probe transparent materials. Although the use of optical interferometry, as reviewed, has become more widespread over the years in the field of picosecond laser ultrasonics, its application to TDBS depth profiling remained untouched up to now, despite the promising theoretical expectations available.

In chapter 2, the design and the construction of the ultrafast Sagnac interferometer has been presented in details. The versatility of its use for doing reflectometric or interferometric detection has been discussed. The chosen solution for allowing easy change of the probe angle of incidence has then been described and explained in details for the most important components where the good choice matters for the good operation of the instrument. Few indications on how to install, align and adjust some key elements have also been described. Finally, the first signals obtained in reflectometric regime of detection have been shown.

In chapter 3, a model of the probe light intensity reaching the balanced photodetector has been derived and used to illustrate the effects of few factors leading to a deviation of the results from that of an ideal case where only the acoustic contribution would have been at play. The effects of thermal background, of sample properties variations during the measurement, and of noises, all being experimental factors, have been analyzed. The effects of human factors such as a misbalancing of the reference and probing electric field amplitudes and of a misorientation of the quarter-wave plate have also been discussed. Then, a signal processing procedure, aiming at reducing the influence of the previous factors, has been proposed and described. The ultrafast Sagnac interferometer has finally been used to conduct experiments in a homogeneous sample of GaAs. These first experiments allowed to shed light onto two important aspects a user of such interferometer have to take care of, namely the achievement of the best balancing possible between the reference and probing electric field amplitudes and the choice of the probe light polarization to favor the amplitude of the part of the signals that matters for depth profiling.

Finally in chapter 4, it has been discussed that the flexible construction of the instrument provides opportunity to restructure its optical scheme from monitoring of the coherent acoustic pulses propagating in the bulk of the material to those propagating/skimming along the surface. The implemented flexible design also makes easy and fast the change from the interferometric regime of measurements to a reflectometric one and can provide the opportunity to measure the time derivative of the transient optical reflectivity phase after few minor adjustments.

The first application of the ultrafast interferometry in TDBS imaging was the demon-

---

stration of a linear dependence of the transient reflectivity phase on depth in homogeneous samples, paving the way to measure the deviation from the linear law in spatially inhomogeneous ones. Easily angle-adjustable fiber ultrafast Sagnac interferometer increase the functionality and utility of the TDBS technique for imaging in all areas of science, including physics, chemistry, biology and medicine.



# Appendices

# BRILLOUIN FREQUENCY

---

Precise modeling usually serves as proof of a correctly performed experiment. With a sufficient amount of information about the sample and measurement details, a simple formula can be used to predict the Brillouin frequency.

## A.1 Momentum conservation

The energy conservation law can be written in form of energies  $E = \hbar\omega$ , with  $\hbar$  being the Planck constant and  $\omega$  the angular frequency [198, 199]. Since  $\hbar$  is common in all the terms, expression for the Stokes scattering (phonon created) takes the following simplified form with frequencies:

$$\omega_i = \omega_s + \omega_{ac}, \quad (\text{A.1})$$

where  $\omega_i = 2\pi\nu_i$  and  $\omega_s = 2\pi\nu_s$  represent the angular frequencies of the incident and scattered light, respectively, and  $\omega_{ac}$  stands for the one of the acoustic wave. Momentum conservation law in form of wave-vectors ( $\hbar\vec{k}$ ) is given by the following equation:

$$\vec{k}_{in} = \vec{k}_{sn} + \vec{k}_{ac}, \quad (\text{A.2})$$

where  $\vec{k}_{in}$ ,  $\vec{k}_{sn}$  and  $\vec{k}_{ac}$  are the wave-vectors of the incident light, scattered light and acoustic wave, respectively. Taking into account the refractive index  $n_i$  and  $n_s$  of the medium for the incident and scattered light, respectively, the norms of the light wave vectors, *i.e.*, the light wavenumbers, are  $k_{in} = n_i k_i$  and  $k_{sn} = n_s k_s$  with  $k_i = \omega_i/c_0$  and  $k_s = \omega_s/c_0$  the wavenumbers of the incident and scattered light in vacuum, respectively,  $c_0$  being the velocity of light in vacuum. Equations (A.1) and (A.2) must be satisfied for the scattering of the incident light by the acoustic wave to be efficient. The momentum conservation law [Eq. (A.2)] can be illustrated as shown in Fig. A.1.

In Fig. A.1, the angle  $\theta_{in}$  between  $\vec{k}_{ac}$  and  $\vec{k}_{in}$  in the medium can be derived from the incidence angle  $\theta_i$  of the incident light at the free surface of the medium using the Snell's law:  $\theta_{in} = \arcsin(\frac{\sin\theta_i}{n})$ . Because  $\omega_{ac} \ll \omega_i$  and  $\omega_{ac} \ll \omega_s$ , *i.e.*, the Brillouin shift is small, Eq. (A.1) allows to state that  $\omega_i \approx \omega_s$ , which yields to  $k_{in} \approx k_{sn}$ . This assumption allows to obtain the following relation between light and acoustic wavenumbers, following

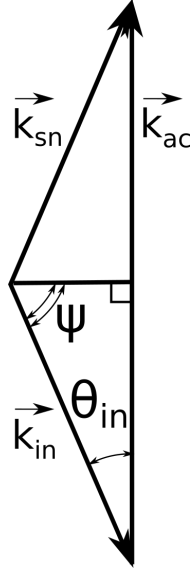


Figure A.1 – Momentum conservation triangle.

Eq. (A.2):

$$k_{ac} = 2k_{in} \cos \theta_{in} \quad (\text{A.3})$$

The wavenumbers in Eq. (A.3) are given by the expressions:

$$k_{ac} = \frac{\omega_{ac}}{v_{ac}} = \frac{2\pi f_B}{v_{ac}}, \quad (\text{A.4})$$

$$k_{in} = \frac{\omega_i}{c_0} n = \frac{2\pi n}{\lambda_0}, \quad (\text{A.5})$$

where  $f_B$  is the Brillouin frequency shift, *i.e.*, the frequency of the acoustic wave which enables the efficient scattering of the incident light,  $v_{ac}$  is the acoustic wave velocity and  $\lambda_0$  is the optical wavelength in vacuum. Combining Eqs. (A.4) and (A.5) in Eq. (A.3), the expression for the Brillouin frequency is derived:

$$f_B = \frac{2nv_{ac}}{\lambda_0} \cos \theta_{in}, \quad (\text{A.6})$$

which can also be given in terms of the angle of incidence at the free surface of the medium  $\theta_i$  as:

$$f_B = \frac{2v_{ac}}{\lambda_0} \sqrt{n^2 - \sin^2 \theta_i}. \quad (\text{A.7})$$

Note that if the light is incident from a medium with a refractive index  $n_0 > 1$ ,  $\sin \theta_{in} = \frac{n_0 \sin \theta_i}{n}$ . Hence Eq. (A.7) will read instead:

$$f_B = \frac{2v_{ac}}{\lambda_0} \sqrt{n^2 - n_0^2 \sin^2 \theta_i}, \quad (\text{A.8})$$

## A.2 Bragg's condition

It is interesting to look at another way of derivation of the Brillouin frequency expression that one can find in the literature in order to avoid a misunderstanding whether the angle dependence in Eq. (A.6) shows up as a sine or cosine function. This confusion arises when the Brillouin expression is derived from the Bragg condition. Indeed, the Brillouin scattering can also be understood as a light field incident on a periodic grating, an acoustic plane wave of periodicity  $\Lambda_{ac}$ , which diffracts the incident light. In the case of Brillouin scattering, this grating is stationary because  $c_0 \gg v_{ac}$ . The constructive interference occurs in directions having angles  $\psi_m$  with respect to the acoustic wavefront plane (in the incident plane), with integer orders  $m$  related to  $\psi_m$ ,  $\Lambda_{ac}$  and the light wavelength in the elastic medium  $\lambda$  by the Bragg condition [29]:

$$m\lambda = 2\Lambda_{ac} \sin \psi_m. \quad (\text{A.9})$$

Keeping the first order of diffraction and simplifying the notation of  $\psi_1 \equiv \psi$ , the Brillouin scattering can be schematized as a Bragg diffraction configuration [Fig. A.2].

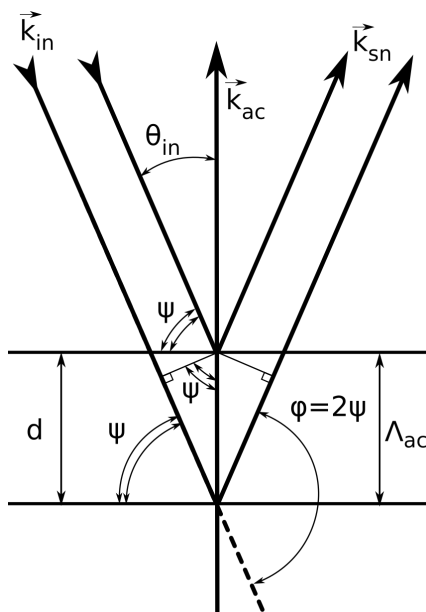


Figure A.2 – Two identical incident waves in phase scatter on two parallel surfaces separated by  $\Lambda_{ac}$  with the lower-passing wave traveling an extra path of length  $2\Lambda_{ac} \sin \psi$ .

Defining the acoustic wavelength as  $\Lambda_{ac} = v_{ac}/f_B$ , Eq. (A.9) with  $m = 1$  reads:

$$\lambda = 2 \frac{v_{ac}}{f_B} \sin \psi, \quad (\text{A.10})$$

which in turn gives:

$$f_B = \frac{2nv_{ac}}{\lambda_0} \sin \psi, \quad (\text{A.11})$$

---

where  $\lambda = \lambda_0/n$  has been substituted.

It is clear from this derivation and the scheme in Fig. A.2 that both expression of the Brillouin frequency, Eqs. (A.6) and (A.11), are equivalent and are just written with different angles. Those angles are linked by :  $\psi = \frac{\pi}{2} - \theta_{in}$ .

# JONES CALCULUS OF THE LIGHT INTENSITY REACHING THE PHOTODETECTOR

---

In a Sagnac interferometer, the probe pulse is split into two pulses reaching the sample surface at a fixed time delay, chosen to be 4 ns in our case: a reference pulse and a probing pulse. In our case, the reference pulse always reaches the sample surface before the pump pulse, while the probing pulse can reach the sample surface before or after the pump pulse, depending on the time delay, set by the delay line, between the pump and the probe pulse (before the splitting). In this appendix, the expression of the light intensity reaching the photodetector, and in which the reference and probing electric fields interfere, will be derived by Jones calculus. It will be seen from this expression that a thoughtful combination of two consecutive measurements of the intensity with a variation in the way the reference and probing electric fields are made to interfere allows to split the changes of the sample reflectance in amplitude  $\rho$  and phase  $\delta\phi$  induced by the pump pulse.

Consider the probing  $E_{1r}$  and the reference  $E_{2r}$  electric fields. Due to the construction of the Sagnac interferometer, both electric fields are orthogonally polarized (linear horizontal and linear vertical) at the output of the interferometer loop (after the polarizing beam splitter [PBS in Fig. 2.2]). Upon reflection on the non-polarizing beam splitter (NPBS in Fig. 2.2), an additional  $\pi$  phase shift is introduced since the horizontally polarized light is reversed, contrary to the vertically polarized one. From the implemented setup,  $E_{1r}$  is polarized horizontally while  $E_{2r}$  is polarized vertically after the NPBS. The total electric field after the NPBS and before the quarter-wave plate (QWP in Fig. 2.2) and the polarizer (POL<sub>2</sub> in Fig. 2.2) on the path to the « + » channel of the balanced photodetector can hence be written in a vector form as:

$$\vec{E}_{tot} = \begin{pmatrix} -E_{1r} \\ E_{2r} \end{pmatrix}. \quad (\text{B.1})$$

Using the Jones calculus, the total electric field after the QWP and POL<sub>2</sub> can be obtained, from which the intensity expression will be given.

First, let us write the Jones matrices (see p. 378 in Ref. [200]) for the QWP and

---

POL<sub>2</sub> for the case where the fast axis and the transmission axis, respectively, are oriented horizontally.

The Jones matrix for a QWP with a fast axis set horizontally is [200]

$$M_{QWP0^\circ} = e^{i\pi/4} \begin{bmatrix} 1 & 0 \\ 0 & i \end{bmatrix}, \quad (\text{B.2})$$

where a  $\frac{\pi}{2}$  retardation is introduced to the vertical component of the electromagnetic field. Note that, here, all Jones vectors and matrices employ the temporal convention  $\exp(-i\omega t)$ , explaining why the change in phase introduced to the vertical component of the electric field is a retardation and not an advance in phase. The Jones matrix for a polarizer with a transmission axis set horizontally is [200]

$$M_{POL0^\circ} = \begin{bmatrix} 1 & 0 \\ 0 & 0 \end{bmatrix}, \quad (\text{B.3})$$

where the transmission of the horizontally polarized components of the light wave is the only one allowed.

Now, to get Jones matrices for any orientation around the optical axis about an angle  $\theta$  of the optical component, the rotation matrix

$$M_{ROT}(\theta) = \begin{bmatrix} \cos \theta & \sin \theta \\ -\sin \theta & \cos \theta \end{bmatrix} \quad (\text{B.4})$$

should be used by multiplying on the left by  $M_{ROT}(-\theta)$  and on the right by  $M_{ROT}(\theta)$  so that

$$M_\theta = M_{ROT}(-\theta) M M_{ROT}(\theta), \quad (\text{B.5})$$

where  $M$  is the initial matrix and  $M_\theta$  is the matrix for the optical element rotated by the angle  $\theta$ .

Using the rotation matrix, the matrices for the QWP and POL<sub>2</sub> oriented at an arbitrary angle  $\theta$  can hence be calculated. The one for the QWP reads:

$$\begin{aligned} M_{QWP\theta} &= e^{i\pi/4} \begin{bmatrix} \cos \theta & -\sin \theta \\ \sin \theta & \cos \theta \end{bmatrix} \begin{bmatrix} 1 & 0 \\ 0 & i \end{bmatrix} \begin{bmatrix} \cos \theta & \sin \theta \\ -\sin \theta & \cos \theta \end{bmatrix} \\ &= e^{i\pi/4} \begin{bmatrix} \cos \theta & -\sin \theta \\ \sin \theta & \cos \theta \end{bmatrix} \begin{bmatrix} \cos \theta & \sin \theta \\ -i \sin \theta & i \cos \theta \end{bmatrix} \\ &= e^{i\pi/4} \begin{bmatrix} \cos^2 \theta + i \sin^2 \theta & (1-i) \sin \theta \cos \theta \\ (1-i) \sin \theta \cos \theta & \sin^2 \theta + i \cos^2 \theta \end{bmatrix}, \end{aligned} \quad (\text{B.6})$$

while the one for the polarizer is:

$$\begin{aligned}
M_{POL\theta} &= \begin{bmatrix} \cos \theta & -\sin \theta \\ \sin \theta & \cos \theta \end{bmatrix} \begin{bmatrix} 1 & 0 \\ 0 & 0 \end{bmatrix} \begin{bmatrix} \cos \theta & \sin \theta \\ -\sin \theta & \cos \theta \end{bmatrix} \\
&= \begin{bmatrix} \cos \theta & -\sin \theta \\ \sin \theta & \cos \theta \end{bmatrix} \begin{bmatrix} \cos \theta & \sin \theta \\ 0 & 0 \end{bmatrix} \\
&= \begin{bmatrix} \cos^2 \theta & \sin \theta \cos \theta \\ \sin \theta \cos \theta & \sin^2 \theta \end{bmatrix}.
\end{aligned} \tag{B.7}$$

After the reflection on NPBS, the two orthogonally polarized waves pass the combination of QWP and POL<sub>2</sub>, where the conditions for the interference are made. There are several possible ways to make them interfere:

- QWP and POL<sub>2</sub> combination, where QWP is set to 0° and 90° (two measurements have to be done) and a polarizer is oriented whether at 45° or 135°.
- QWP and POL<sub>2</sub> combination, where QWP is set to 45° and 135° while a polarizer is oriented whether at 0° and 90°.
- QWP and PBS combination, where QWP is set to 0° or 90°, while PBS sends the two parts of the splitted interfering light to the (+) and (-) sensitive areas of the differential photodetector.

In our case, the choice has been made to set the POL<sub>2</sub> at 45° and to switch the QWP angle between 0° and 90°, because it is preferable when using a thick polarizer. The total electric field after the QWP set to an arbitrary angle  $\psi$  reads:

$$\begin{aligned}
\vec{E}_{tot}^{QWP\psi} &= M_{QWP\psi} \vec{E}_{tot} \\
&= e^{i\pi/4} \begin{bmatrix} \cos^2 \psi + i \sin^2 \psi & (1-i) \sin \psi \cos \psi \\ (1-i) \sin \psi \cos \psi & \sin^2 \psi + i \cos^2 \psi \end{bmatrix} \begin{pmatrix} -E_{1r} \\ E_{2r} \end{pmatrix} \\
&= e^{i\pi/4} \begin{pmatrix} -(\cos^2 \psi + i \sin^2 \psi)E_{1r} + (1-i) \sin \psi \cos \psi E_{2r} \\ -(1-i) \sin \psi \cos \psi E_{1r} + (\sin^2 \psi + i \cos^2 \psi)E_{2r} \end{pmatrix}
\end{aligned} \tag{B.8}$$

Finally, after passing through the POL<sub>2</sub> set to 45°, the total electric field finally reads:

$$\begin{aligned}
\vec{E}_{tot}^{QWP\psi, POL45^\circ} &= M_{POL45^\circ} \vec{E}_{tot}^{QWP\psi} \\
&= \frac{e^{i\pi/4}}{2} \begin{bmatrix} 1 & 1 \\ 1 & 1 \end{bmatrix} \begin{pmatrix} -(\cos^2 \psi + i \sin^2 \psi)E_{1r} + (1-i) \sin \psi \cos \psi E_{2r} \\ -(1-i) \sin \psi \cos \psi E_{1r} + (\sin^2 \psi + i \cos^2 \psi)E_{2r} \end{pmatrix} \\
&= \frac{e^{i\pi/4}}{2} (-A_\psi E_{1r} + B_\psi E_{2r}) \begin{pmatrix} 1 \\ 1 \end{pmatrix},
\end{aligned} \tag{B.9}$$

where  $A_\psi$  and  $B_\psi$  are defined as follows:

$$A_\psi = \cos^2 \psi + i \sin^2 \psi + (1 - i) \sin \psi \cos \psi, \quad (\text{B.10})$$

$$B_\psi = \sin^2 \psi + i \cos^2 \psi + (1 - i) \sin \psi \cos \psi. \quad (\text{B.11})$$

When the QWP is set to  $\psi = 0^\circ$ , since  $A_0 = 1$  and  $B_0 = i$ , this leads to:

$$\vec{E}_{tot}^{QWP0^\circ, POL45^\circ} = \frac{e^{i\pi/4}}{\sqrt{2}} (-E_{1r} + iE_{2r}) \begin{pmatrix} 1/\sqrt{2} \\ 1/\sqrt{2} \end{pmatrix}, \quad (\text{B.12})$$

while when the QWP is set to  $\psi = 90^\circ$ , since  $A_0 = i$  and  $B_0 = 1$ , the total electric field reads:

$$\vec{E}_{tot}^{QWP90^\circ, POL45^\circ} = \frac{e^{i\pi/4}}{\sqrt{2}} (-iE_{1r} + E_{2r}) \begin{pmatrix} 1/\sqrt{2} \\ 1/\sqrt{2} \end{pmatrix}. \quad (\text{B.13})$$

Equations (B.12) and (B.13) allows to express the intensities  $I_{0^\circ}$  and  $I_{90^\circ}$  reaching the + channel of the balanced photodetector for both orientations of the QWP, which reads:

$$I_{0^\circ} = \left\| \vec{E}_{tot}^{QWP0^\circ, POL45^\circ} \right\| \left\| \vec{E}_{tot}^{QWP0^\circ, POL45^\circ} \right\|^* = \frac{1}{2} (-E_{1r} + iE_{2r}) (-E_{1r}^* - iE_{2r}^*), \quad (\text{B.14})$$

$$I_{90^\circ} = \left\| \vec{E}_{tot}^{QWP90^\circ, POL45^\circ} \right\| \left\| \vec{E}_{tot}^{QWP90^\circ, POL45^\circ} \right\|^* = \frac{1}{2} (-iE_{1r} + E_{2r}) (iE_{1r}^* + E_{2r}^*), \quad (\text{B.15})$$

where « \* » stands for the complex conjugate. Finally, the intensities are given by:

$$2I_{0^\circ} = E_{1r}E_{1r}^* + E_{2r}E_{2r}^* + i(E_{1r}E_{2r}^* - E_{1r}^*E_{2r}), \quad (\text{B.16})$$

$$2I_{90^\circ} = E_{1r}E_{1r}^* + E_{2r}E_{2r}^* - i(E_{1r}E_{2r}^* - E_{1r}^*E_{2r}). \quad (\text{B.17})$$

Consider that  $r$  is the complex amplitude-reflection coefficient (reflectance) of the sample seen by the reference pulse (field  $E_{2r}$ ) and that  $r' = r'(t)$  is the coefficient seen by the probing pulse (field  $E_{1r}$ ), where  $t$  is the delay time between the pump and the probe pulses. The reflectance seen by the reference pulse is assumed to be  $r = r_0 e^{i\varphi_0}$  and that seen by the probing pulse is assumed to be  $r' = r_0 e^{i\varphi_0} (1 + \rho e^{i\delta\phi})$ . Here,  $\rho \ll 1$  and  $\delta\phi$  account for the change in amplitude and phase of the reflectance induced by the pump pulse. Note that this expression of  $r'$  is not the same as in Ref. [13]. With the here-assumed definition of  $r$  and  $r'$ , the relative change in reflectance  $\delta r/r$  is:

$$\frac{\delta r}{r} = \frac{r' - r}{r} = \rho e^{i\delta\phi}. \quad (\text{B.18})$$

Note also that we cannot assume here that  $\delta\phi$  is small relative to 1, contrary to the described case in Ref. [13] of an absorbing material, because the sample is here assumed to be transparent and hence  $\delta\phi$  will increase with time while the acoustic pulse will

propagate. Following the definitions of  $r$  and  $r'$ , the reference and probing electric fields can be expressed as:

$$E_{1r}(t, z) = r'(t)E_1e^{i(kz-\omega t)}, \quad (\text{B.19})$$

$$E_{2r}(t, z) = rE_2e^{i(kz-\omega t)}, \quad (\text{B.20})$$

where  $E_1$  and  $E_2$  are the amplitude of both reference and probing electric fields incident on the sample surface,  $k$  is the optical wavenumber,  $z$  the coordinate defining the direction of the optical axis and  $\omega$  is the optical angular frequency.

Using Eqs. (B.19) and (B.20) in Eqs. (B.16) and (B.17) allows to derive the expressions of both intensities. Omitting the dependency of  $r'$  with  $t$ , the intensities hence are:

$$I_{0^\circ} = r'(r')^*E_1^2 + rr^*E_2^2 + iE_1E_2(r^*r' - r(r')^*), \quad (\text{B.21})$$

$$I_{90^\circ} = r'(r')^*E_1^2 + rr^*E_2^2 - iE_1E_2(r^*r' - r(r')^*). \quad (\text{B.22})$$

In the previous expressions of  $I_{0^\circ}$  and  $I_{90^\circ}$ , the following expressions can be used:

$$rr^* = r_0^2, \quad (\text{B.23})$$

$$r'(r')^* = r_0^2(1 + 2\rho \cos \delta\phi + \rho^2) \approx r_0^2(1 + 2\rho \cos \delta\phi), \quad (\text{B.24})$$

$$r(r')^* = r_0^2(1 + \rho e^{-j\delta\phi}), \quad (\text{B.25})$$

$$r^*r' = r_0^2(1 + \rho e^{+j\delta\phi}), \quad (\text{B.26})$$

which leads to:

$$I_{0^\circ} = \frac{r_0^2}{2}(E_2^2 + E_1^2 + 2E_1^2\rho \cos \delta\phi - 2E_1E_2\rho \sin \delta\phi), \quad (\text{B.27})$$

$$I_{90^\circ} = \frac{r_0^2}{2}(E_2^2 + E_1^2 + 2E_1^2\rho \cos \delta\phi + 2E_1E_2\rho \sin \delta\phi). \quad (\text{B.28})$$

The output  $s_\psi$  of the balanced photodetector can then be expressed in both cases, assuming that  $E_1 = E_2$  and that the intensity on the « - » channel is set to  $\frac{r_0^2}{2}(E_2^2 + E_1^2)$ :

$$s_0 = Sr_0^2E_1^2(\rho \cos \delta\phi - \rho \sin \delta\phi), \quad (\text{B.29})$$

$$s_{90} = Sr_0^2E_1^2(\rho \cos \delta\phi + \rho \sin \delta\phi), \quad (\text{B.30})$$

where  $S$  is the detector sensitivity in  $V/(W/m^2)$ . Hence, we finally obtain by the half sum and half difference of the previous signals:

$$\frac{s_{90} + s_0}{2} = Sr_0^2E_1^2\rho \cos \delta\phi, \quad (\text{B.31})$$

$$\frac{s_{90} - s_0}{2} = Sr_0^2E_1^2\rho \sin \delta\phi, \quad (\text{B.32})$$

---

which allows to get:

$$\rho = \frac{\sqrt{\left(\frac{s_{90} + s_0}{2}\right)^2 + \left(\frac{s_{90} - s_0}{2}\right)^2}}{Sr_0^2 E_1^2}, \quad (\text{B.33})$$

and

$$\delta\phi = \arctan\left(\frac{s_{90} - s_0}{s_{90} + s_0}\right). \quad (\text{B.34})$$

To obtain the expressions of  $\rho$  and  $\delta\phi$  in Eqs.(B.33)-(B.34), it is important to remember that we assumed  $r' = r_0 e^{j\varphi_0} (1 + \rho e^{j\delta\phi})$  where  $\rho$  and  $\delta\phi$  are linked to the reflectance variation in amplitude and phase, respectively, due to a propagating acoustic pulse in a transparent semi-half space. Unfortunately,  $r'$  is usually « poisoned » by extra terms caused by the pump laser pulse because of the temperature dependence of the reflectance and/or by the processes taking place during the short intervals of time when the strain pulse interacts with the surfaces/interfaces [17].

# LIGHT INSERTION INTO THE SINGLE-MODE POLARIZATION-MAINTAINING OPTICAL FIBER

---

To achieve the set task of depth-profiling of materials, we needed to make an experimental setup that would allow changing the angle of incidence of the probe beam without displacing the sample relative to the pump beam. To solve this technical problem, I have designed 8 possible configurations of the experimental setup. Among all the configurations created, we decided to choose the one based on a combination of optical fiber with a precise rotary mechanism for further improvement, since it is necessary to make a list for the purchase of absolutely all elements for future installation. This means that the choice of the optical fiber and of the method of introducing light into this fiber also had to be made. The procedure of the light introduction into an optical fiber is rather simple since it requires to use a focusing optical element to direct light to the core of the optical fiber. The efficient light insertion is more difficult to reach, but the entire process still can remain simple if an experienced user has all necessary equipment and sufficient amount of patience (the optimization process is very repetitive). The main two techniques of the light insertion in an optical fiber are:

1. The light-focusing optical element (lens has to be capable of focusing light in a spot of size comparable to that of the fiber core) is fixed. The optical fiber is installed on a multi-axis stage which is used for the angular and spatial positioning of the fiber in order for the focused light to enter the fiber.
2. The fiber is connected to a suitable fiber collimator. The laser beam on-lens displacement is achieved using two adjustable mirrors in front of the collimator or by using a multi-axis stage that is used for the collimator-fiber pair linear and angular displacement relatively to the laser beam.

Depending on the nature of the application, multi-mode optical fibers or single-mode fibers can be used. As maintaining the polarization of EM waves that pass through the optical fiber is essential for our work, it is therefore only possible to use a single-mode

---

optical fiber for the reason that multimode optical fibers capable of maintaining polarization are not commercially available. Work with a multi-mode fiber allows the use of a single lens since the core diameter is 50  $\mu m$  or more, while the single-mode fiber core diameter does not exceed 10  $\mu m$  hence requiring, for an efficient light insertion, the use of an objective or aspheric lenses. The option where the light is fed into the optical fiber using a remote lens or objective was rejected in favor of the option with a direct connection of the collimator to the optical fiber with a ferrule connection. The setup was planned to be in active use for a long time not in a clean room conditions, meaning that such factor as a dust has to be considered as well. A particle of dust of a similar size settled on the bare fiber core, which has a diameter of of 5  $\mu m$  in our case, or on the collimator lens, which has a clear aperture of 6 mm, will lead either to a serious or a negligible problem, respectively. Additional advantages of using a ferrule connection can also be attributed to compactness (in comparison with a multi-axis table and additional optics), fewer degrees of freedom (therefore more reliable fixation) and ease of use (if the necessary equipment listed below is at hand).

The FC/APC patching allows to avoid the retroreflection of light which is a critically important point for the protection of the laser from the light return to the cavity. FC/PC fiber patching type will not be able to prevent the laser light partial return into the cavity due to the fact that the maximum light insertion efficiency is achieved for the normal light incidence, hence the reflected laser radiation will follow the exact same optical path back, straight into the laser cavity. FC/APC connector type serves precisely to prevent light reflection in the backward direction, but this type of the fiber patching increases the complexity of the light insertion in the optical fiber compared to FC/PC. This is the price that must be paid for such benefits as laser protection and the protection from the artifacts, that may arise if the reflected light would have also reached the photodetector.

Beam walk method is the main tool for the light-to-fiber coupling and for the subsequent augmentation of the light insertion efficiency. A step-by-step guide is given in the subsection 2.4.1, but it is often better to have a comprehensive video guide. The one made by researchers from the University of South Florida [201] gives a demonstration of a technique of the light-to-fiber initial coupling with the help of another fiber that is already coupled to a laser.

To achieve the maximum of the light energy that goes into the fiber, multiple cycles of the optimization must be conducted. To make this optimization process easier, it is recommended to choose a mirror holders with paying attention to the following details (or a multi-axis stage):

1. The adjustment screws with a small thread pitch (TPI value above 100) will allow the alignment procedure to be conducted smoothly. Adjustment screws with low TPI value may lead to the situation where the best point/angle at current iteration is missed due to the low sensitivity and, if not missed, it may be hard to align to

---

this position by jumping over it.

2. A lock screw is a critically important detail that will protect already aligned optical elements from an accidental touch as soon as the lock screw is locked.

# DEPTH-PROFILING WITH TWO INCIDENCE ANGLES

---

Two separate measurements of the Brillouin frequency with two different angles of incidence of the probe beam allow to disentangle the variations with depth of the speed of sound  $v_{ac}$  and refractive index  $n$  from the variation with depth of the Brillouin frequency. Consider a probe beam of wavelength  $\lambda_0$  incident on a surface between some transparent medium of refractive index  $n_0$  and the material under study at incidence angles  $\theta_{i_1}$  and  $\theta_{i_2}$ . The light is inelastically scattered by an acoustic wave traveling with the speed  $v_{ac}$ . Resulting frequencies of the Brillouin oscillations,  $f_{B_1}$  or  $f_{B_2}$  depending on the incidence angle, can be written as [Eq. (A.8)]:

$$f_{B_1} = \frac{2v_{ac}\sqrt{n^2 - n_0^2 \sin^2 \theta_{i_1}}}{\lambda_0}, \quad (\text{D.1a})$$

$$f_{B_2} = \frac{2v_{ac}\sqrt{n^2 - n_0^2 \sin^2 \theta_{i_2}}}{\lambda_0}. \quad (\text{D.1b})$$

In the equations above, the only unknown members are  $v_{ac}$  and  $n$ . The following equations gives the details of the calculations allowing to derive these two parameters from the two values of the Brillouin frequency for two different incidence angles of the probing beam.

First, Eqs. (D.1) are squared:

$$f_{B_1}^2 = \frac{4v_{ac}^2(n^2 - n_0^2 \sin^2 \theta_{i_1})}{\lambda^2}, \quad (\text{D.2a})$$

$$f_{B_2}^2 = \frac{4v_{ac}^2(n^2 - n_0^2 \sin^2 \theta_{i_2})}{\lambda^2}. \quad (\text{D.2b})$$

To obtain the expression of  $n$ , it is then sufficient to divide Eq. (D.2a) by Eq. (D.2b), which leads to:

$$\frac{f_{B_1}^2}{f_{B_2}^2} = \frac{n^2 - n_0^2 \sin^2 \theta_{i_1}}{n^2 - n_0^2 \sin^2 \theta_{i_2}}. \quad (\text{D.3})$$

---

The expression of  $n$  follows:

$$n = n_0 \sqrt{\frac{f_{B_1}^2 \sin^2 \theta_{i_2} - f_{B_2}^2 \sin^2 \theta_{i_1}}{f_{B_1}^2 - f_{B_2}^2}}. \quad (\text{D.4})$$

To obtain the expression of  $v_{ac}$ , it can be first seen from Eqs. (D.2a) and (D.2b) that the following equation holds:

$$f_{B_1}^2 + \frac{4v_{ac}^2}{\lambda^2} n_0^2 \sin^2 \theta_{i_1} = f_{B_2}^2 + \frac{4v_{ac}^2}{\lambda^2} n_0^2 \sin^2 \theta_{i_2}, \quad (\text{D.5})$$

which easily leads to the expression of  $v_{ac}$  as follows:

$$v_{ac} = \frac{\lambda}{2n_0} \sqrt{\frac{f_{B_1}^2 - f_{B_2}^2}{\sin^2 \theta_{i_2} - \sin^2 \theta_{i_1}}}. \quad (\text{D.6})$$

The expressions obtained for refractive index and sound velocity can be used to study the variation of these parameters within a volume of inhomogeneous sample using, for example, a short-time Fourier transform with a window size of few Brillouin oscillation periods which will allow, with some spatial resolution depending on oscillation wavelength and signal quality, to obtain data on how these parameters vary based on the numerical frequencies value obtained from the Fourier transform.

# BIBLIOGRAPHY

---

- [1] P. Ruello and V. E. Gusev, « *Physical mechanisms of coherent acoustic phonons generation by ultrafast laser action* », **Ultrasonics**, vol. 56, pp. 21–35, (2015), DOI: 10.1016/j.ultras.2014.06.004 [[Crossref](#)].
- [2] A. G. Bell, « *On the production and reproduction of sound by light* », **Am. Jour. Sci.**, 3rd ser., vol. 20, no. 118, pp. 305–324, (1880), DOI: 10.2475/ajs.s3-20.118.305 [[Crossref](#)].
- [3] A. G. Bell, « *Upon the production of sound by radiant energy* », **Philosophical Magazine**, 5th ser., vol. 11, no. 71, pp. 510–528, (1881), DOI: 10.1080/14786448108627053 [[Crossref](#)].
- [4] T. Maiman, « *Stimulated Optical Radiation in Ruby* », **Nature**, vol. 187, no. 4736, pp. 493–494, (1960), DOI: 10.1038/187493a0 [[Crossref](#)].
- [5] C. Thomsen, J. Strait, Z. Vardeny, H. J. Maris, J. Tauc, and J. J. Hause, « *Coherent phonon generation and detection by picosecond light pulse* », **Phys. Rev. Lett.**, vol. 53, no. 10, pp. 989–992, (1984), DOI: 10.1103/PhysRevLett.53.989 [[Crossref](#)].
- [6] O. B. Wright and T. Hyoguchi, « *Ultrafast vibration and laser acoustics in thin transparent films* », **Opt. Lett.**, vol. 16, no. 19, pp. 1529–1531, (1991), DOI: 10.1364/OL.16.001529 [[Crossref](#)].
- [7] J. E. Rothenberg, « *Observation of the transient expansion of heated surfaces by picosecond photothermal deflection spectroscopy* », **Opt. Lett.**, vol. 13, no. 9, pp. 713–715, (1988), DOI: 10.1364/OL.13.000713 [[Crossref](#)].
- [8] O. B. Wright and K. Kawashima, « *Coherent phonon detection from ultrafast surface vibrations* », **Phys. Rev. Lett.**, vol. 69, no. 11, pp. 1668–1671, (1992), DOI: 10.1103/PhysRevLett.69.1668 [[Crossref](#)].
- [9] N. Chigarev, C. Rossignol, and B. Audoin, « *Surface displacement measured by beam distortion detection technique: application to picosecond ultrasonics* », **Rev. Sci. Instrum.**, vol. 77, no. 11, 114901, (2006), DOI: 10.1063/1.2372739 [[Crossref](#)].
- [10] J. Higuët, T. Valier-Brasier, T. Dehoux, and B. Audoin, « *Beam distortion detection and deflectometry measurements of gigahertz surface acoustic waves* », **Rev. Sci. Instrum.**, vol. 82, no. 11, 114905, (2011), DOI: 10.1063/1.3660193 [[Crossref](#)].
- [11] B. Perrin, B. Bonello, J. C. Jeannet, and E. Romatet, « *Interferometric detection of hypersound waves in modulated structures* », **Prog. Nat. Sci.**, vol. 6 (supplement to), S444–S448, (1996), [[Crossref](#)].

- 
- [12] B. Perrin, C. Rossignol, B. Bonello, and J.-C. Jeannet, « *Interferometric detection in picosecond ultrasonics* », **Physica B Condens. Matter**, vol. 263–264, pp. 571–573, (1999), DOI: 10.1016/S0921-4526(98)01479-3 [Crossref].
- [13] D. H. Hurley and O. B. Wright, « *Detection of ultrafast phenomena by use of a modified Sagnac interferometer* », **Opt. Lett.**, vol. 24, no. 18, pp. 1305–1307, (1999), DOI: 10.1364/OL.24.001305 [Crossref].
- [14] W. Volksen, R. D. Miller, and G. Dubois, « *Low Dielectric Constant Materials* », **Chemical Reviews**, vol. 110, no. 1, pp. 56–110, (2010), DOI: 10.1021/cr9002819 [Crossref].
- [15] C. Mechri, P. Ruello, J.-M. Breteau, M. R. Baklanov, P. Verdonck, and V. Gusev, « *Depth-profiling of elastic inhomogeneities in transparent nanoporous low- $\kappa$  materials by picosecond ultrasonic interferometry* », **Appl. Phys. Lett.**, vol. 95, no. 9, 091907, (2009), DOI: 10.1063/1.3220063 [Crossref].
- [16] A. M. Lomonosov *et al.*, « *Nanoscale noncontact subsurface investigations of mechanical and optical properties of nanoporous low- $\kappa$  material thin films* », **ACS Nano**, vol. 6, no. 2, pp. 1410–1415, (2012), DOI: 10.1021/nm204210u [Crossref].
- [17] V. Gusev, A. M. Lomonosov, P. Ruello, A. Ayouch, and G. Vaudel, « *Depth-profiling of elastic and optical inhomogeneities in transparent materials by picosecond ultrasonic interferometry: Theory* », **J. Appl. Phys.**, vol. 110, no. 12, 124908, (2011), DOI: 10.1063/1.3665646 [Crossref].
- [18] V. E. Gusev and A. A. Karabutov, « *Laser Optoacoustics* », trans. by K. Hendzel. AIP Press, (1993), ISBN: 1-56396-036-2, ResearchGate, [Online]. **Available at:** <https://www.researchgate.net/publication/234495004>.
- [19] A. Rosencwaig and A. Gersho, « *Theory of the photoacoustic effect with solids* », **J. Appl. Phys.**, vol. 47, no. 1, pp. 64–69, (1976), DOI: 10.1063/1.322296 [Crossref].
- [20] A. Rosencwaig, « *Thermal-wave imaging* », **Science**, vol. 218, no. 4569, pp. 223–228, (1982), DOI: 10.1126/science.218.4569.223 [Crossref].
- [21] J. J. Berzelius, « *Letter from Mr. Berzelius to Mr. Berthollet on two new metals* », **Ann. Chim. Phys.**, vol. 7, pp. 199–206, (1818), Google Books (Fr.), [Online]. **Available at:** <https://books.google.fr/books?id=jBIAAAAAMAAJ>.
- [22] W. Smith, « *The action of light on selenium* », **J. Soc. Telegraph Eng.**, vol. 2, no. 4, pp. 31–33, (1873), DOI: 10.1049/jste-1.1873.0023 [Crossref].
- [23] J. Tyndall, « *Action of an intermittent beam of radiant heat upon gaseous matter* », **Proc. R. Soc. London**, vol. 31, no. 206–211, pp. 307–317, (1881), DOI: 10.1098/rspl.1880.0037 [Crossref].

- 
- [24] W. Röntgen, « *On tones produced by the intermittent irradiation of a gas* », **Philos. Mag.**, 5th ser., vol. 11, no. 68, pp. 308–311, (1881), DOI: 10.1080/14786448108627021 [Crossref].
- [25] L. Brillouin, « *Diffusion de la lumière et des rayons X par un corps transparent homogène* », **Ann. Phys.**, vol. 9, no. 17, pp. 88–122, (1922), DOI: 10.1051/anphys/192209170088 [Crossref].
- [26] L. Mandelstam, « *Light scattering by inhomogeneous media* », **ZH. Rus. Fiz.-Khim. Ova ((J. Russ. Phys. Chem. Soc.))**, vol. 58, pp. 381–386, (1926), Scientific Heritage of Russia (Rus.), [Online]. **Available at:** <http://books.e-heritage.ru/book/10073903>.
- [27] E. Gross, « *Change of Wavelength of Light due to Elastic Heat Waves at Scattering in Liquids* », **Nature**, vol. 126, no. 3171, pp. 201–202, (1930), DOI: 10.1038/126201a0 [Crossref].
- [28] P. Debye and F. W. Sears, « *Light scattering by inhomogeneous media* », **Proc. Natl. Acad. Sci.**, vol. 18, no. 6, pp. 409–414, (1932), DOI: 10.1073/pnas.18.6.409 [Crossref].
- [29] W. H. Bragg and W. L. Bragg, « *The Reflection of X-rays by Crystals* », **Proc. R. Soc. London**, vol. 88, no. 605, pp. 428–438, (1913), DOI: 10.1098/rspa.1913.0040 [Crossref].
- [30] A. Einstein, « *On the quantum theory of radiation* », trans. by A. Engel. (1997), vol. 6, pp. 220–233, Princeton University Press, [Online]. **Available at:** <https://einsteinpapers.press.princeton.edu/vol6-trans/232>.
- [31] J. Gordon, H. Zeiger, and C. Townes, « *The Maser—New Type of Microwave Amplifier, Frequency Standard, and Spectrometer* », **Phys. Rev.**, vol. 99, no. 4, pp. 1264–1274, (1955), DOI: 10.1103/PhysRev.99.1264 [Crossref].
- [32] S. A. Akhmanov and V. E. Gusev, « *Laser excitation of ultrashort acoustic pulses: new possibilities in solid-state spectroscopy, diagnostics of fast processes, and nonlinear acoustics* », **Sov. Phys. Uspekhi**, vol. 35, no. 3, pp. 153–191, (1992), DOI: 10.1070/pu1992v035n03abeh002221 [Crossref].
- [33] M. Kouyate, T. Pezeril, D. Mounier, and V. Gusev, « *Generation of inhomogeneous plane shear acoustic modes by laser-induced thermoelastic gratings at the interface of transparent and opaque solid* », **J. Appl. Phys.**, vol. 110, no. 12, 123526, (2011), DOI: 10.1063/1.3662921 [Crossref].
- [34] S. J. Davies, C. Edwards, G. S. Taylor, and S. B. Palmer, « *Laser-generated ultrasound: its properties, mechanisms and multifarious applications* », **J. Phys. D: Appl. Phys.**, vol. 29, no. 3, pp. 329–348, (1993), DOI: 10.1088/0022-3727/26/3/001 [Crossref].

- 
- [35] D. A. Hutchins, « *Ultrasonic Generation by Pulsed Lasers* » (Physical Acoustics). Academic Press, (1988), vol. 18, pp. 21–123, ISBN: 978-0-124-77918-1, DOI: 10.1016/B978-0-12-477918-1.50008-4 [\[Crossref\]](#).
- [36] J.-P. Monchalin, « *Laser-Ultrasonics: From the Laboratory to Industry* », **AIP Conference Proceedings**, vol. 700, no. 1, pp. 3–31, (2004), DOI: 10.1063/1.1711602 [\[Crossref\]](#).
- [37] B. Dong, « *Laser-generated ultrasound: its properties, mechanisms and multifarious applications* », **IEEE Trans. Biomed. Eng.**, vol. 64, no. 1, pp. 4–15, (2017), DOI: 10.1109/TBME.2016.2605451 [\[Crossref\]](#).
- [38] M. Inguscio and L. Fallani, « *Atomic Physics: Precise Measurements and Ultracold Matter* », 1st ed. Oxford University Press, (2013), ISBN: 9780198525844, DOI: 10.1093/acprof:oso/9780198525844.001.0001 [\[Crossref\]](#).
- [39] C. B. Scruby, R. J. Dewhurst, D. A. Hutchins, and S. B. Palmer, « *Quantitative studies of thermally generated elastic waves in laser irradiated metals* », **J. Appl. Phys.**, vol. 51, no. 12, pp. 6210–6216, (1980), DOI: 10.1063/1.327601 [\[Crossref\]](#).
- [40] C. Thomsen, H. T. Grahn, H. J. Maris, and J. Tauc, « *Surface generation and detection of phonons by picosecond light pulse* », **Phys. Rev. B**, vol. 34, no. 6, pp. 4129–4138, (1986), DOI: 10.1103/PhysRevB.34.4129 [\[Crossref\]](#).
- [41] H. T. Graham, H. J. Maris, and J. Tauc, « *Picosecond ultrasonics* », **IEEE J. Quantum Electron.**, vol. 25, no. 12, pp. 2562–2569, (1989), DOI: 10.1109/3.40643 [\[Crossref\]](#).
- [42] H. N. Lin, R. J. Stoner, H. J. Maris, and J. Tauc, « *Phonon attenuation and velocity measurements in transparent materials by picosecond acoustic interferometry* », **J. Appl. Phys.**, vol. 69, no. 7, (1991), DOI: 10.1063/1.348958 [\[Crossref\]](#).
- [43] G. Tas and H. J. Maris, « *Electron diffusion in metals studied by picosecond ultrasonics* », **Phys. Rev. B**, vol. 49, no. 21, pp. 15 046–15 054, (1994), DOI: 10.1103/PhysRevB.49.15046 [\[Crossref\]](#).
- [44] O. Matsuda, O. B. Wright, D. H. Hurley, V. Gusev, and K. Shimizu, « *Coherent shear phonon generation and detection with picosecond laser acoustics* », **Phys. Rev. B**, vol. 77, no. 22, 224110, (2008), DOI: 10.1103/PhysRevB.77.224110 [\[Crossref\]](#).
- [45] S. Raetz, T. Dehoux, and B. Audoin, « *Effect of laser beam incidence angle on the thermoelastic generation in semi-transparent material* », **J. Acoust. Soc. Am.**, vol. 130, no. 6, pp. 3691–3697, (2011), DOI: 10.1121/1.3658384 [\[Crossref\]](#).

- 
- [46] G. Vaudel, T. Pezeril, A. Lomonosov, M. Lejman, P. Ruello, and V. Gusev, « *Laser generation of hypersound by a terahertz photo-Dember electric field in a piezoelectric GaAs semiconductor* », **Phys. Rev. B**, vol. 90, no. 1, 014302, (2014), DOI: 10.1103/PhysRevB.90.014302 [Crossref].
- [47] C. B. Scruby and L. E. Drain, « *Laser Ultrasonics* ». Routledge, (1990), ISBN: 9780203749098, DOI: 10.1201/9780203749098 [Crossref].
- [48] O. Matsuda, M. C. Larciprete, R. Li Voti, and O. B. Wright, « *Fundamentals of picosecond laser ultrasonics* », **Ultrasonics**, vol. 56, pp. 3–20, (2015), DOI: 10.1016/j.ultras.2014.06.005 [Crossref].
- [49] J.-P. Monchalain, « *Optical detection of ultrasound* », **IEEE Trans Ultrason. Ferroelectr. Freq. Control**, vol. 33, no. 5, pp. 485–499, (1986), DOI: 10.1109/T-UFFC.1986.26860 [Crossref].
- [50] F. Brech and L. Cross, « *Optical microemission stimulated by a ruby maser* », **Appl. Spectrosc.**, vol. 16, no. 2, p. 59, (1962), DOI: 10.1177/000370286201600204 [Crossref].
- [51] J. A. Schuch and F. Brech, « *Spectrochemical analysis, U.S. Patent 3,680,959 filed 25 February 1963, and issued 1 August 1972, United States Patent and Trademark Office* », USPTO, [Online]. **Available at:** <https://pdfpiw.uspto.gov/.piw?Docid=US3680959>.
- [52] R. M. White, « *An Elastic Wave Method for the Measurement of Pulse-Power Density* », **IRE Trans. Instr.**, vol. I-11, no. 3/4, pp. 294–298, (1962), DOI: 10.1109/IRE-I.1962.5006648 [Crossref].
- [53] R. M. White, « *Elastic Wave Generation by Electron Bombardment or Electromagnetic Wave Absorption* », **J. Appl. Phys.**, vol. 34, no. 7, pp. 2123–2124, (1963), DOI: 10.1063/1.1729762 [Crossref].
- [54] R. M. White, « *Generation of Elastic Waves by Transient Surface Heating* », **J. Appl. Phys.**, vol. 34, no. 12, pp. 3559–3567, (1963), DOI: 10.1063/1.1729258 [Crossref].
- [55] G. A. Askar'yan, A. M. Prokhorov, G. F. Chanturiya, and G. P. Shipulo, « *The effects of a laser beam in liquids* », trans. by L. M. Matarrese, **J. Exptl. Theoret. Phys. (U.S.S.R.)**, vol. 17, no. 6, pp. 1463–1465, (1963), Archives of the JETP, [Online]. **Available at:** [http://www.jetp.ac.ru/cgi-bin/dn/e\\_017\\_06\\_1463.pdf](http://www.jetp.ac.ru/cgi-bin/dn/e_017_06_1463.pdf).
- [56] F. Bentouhami *et al.*, « *LUCIE - A flexible and powerful Laser Ultrasonic system for inspection of large CFRP components* », **2nd International Symposium on Laser Ultrasonics, Talence (France)**, (2010), ResearchGate, [Online]. **Available at:** <https://www.researchgate.net/publication/236208610>.

- 
- [57] V. E. Gusev and P. Ruello, « *Advances in applications of time-domain brillouin scattering for nanoscale imaging* », **Appl. Phys. Rev.**, vol. 5, no. 3, p. 031101, (2018), DOI: 10.1063/1.5017241 [[Crossref](#)].
- [58] R. W. Hellwarth, « *Theory of the Pulsation of Fluorescent Light From Ruby* », **Phys. Rev. Lett.**, vol. 6, no. 1, pp. 9–12, (1961), DOI: 10.1103/PhysRevLett.6.9 [[Crossref](#)].
- [59] F. J. McClung and R. W. Hellwarth, « *Giant Optical Pulsations from Ruby* », **J. Appl. Phys.**, vol. 33, no. 3, pp. 828–829, (1962), DOI: 10.1063/1.1777174 [[Crossref](#)].
- [60] W. E. Lamb, « *Theory of an Optical Maser* », **Phys. Rev.**, vol. 134, no. 6A, A1429–A1450, (1964), DOI: 10.1103/PhysRev.134.A1429 [[Crossref](#)].
- [61] L. E. Hargrove, R. L. Fork, and M. A. Pollack, « *Locking of He–Ne laser modes induced by synchronous intracavity modulation* », **Appl. Phys. Lett.**, vol. 5, no. 1, pp. 4–5, (1964), DOI: 10.1063/1.1754025 [[Crossref](#)].
- [62] E. P. Ippen, C. V. Shank, and A. Dienes, « *Passive mode locking of the CW dye laser* », **Appl. Phys. Lett.**, vol. 21, no. 8, pp. 348–350, (1972), DOI: 10.1063/1.1654406 [[Crossref](#)].
- [63] C. V. Shank and E. P. Ippen, « *Subpicosecond kilowatt pulses from a mode-locked CW dye laser* », **Appl. Phys. Lett.**, vol. 24, no. 8, pp. 373–375, (1974), DOI: 10.1063/1.1655222 [[Crossref](#)].
- [64] R. L. Fork, B. I. Greene, and C. V. Shank, « *Generation of optical pulses shorter than 0.1 psec by colliding pulse mode locking* », **Appl. Phys. Lett.**, vol. 38, no. 9, pp. 671–672, (1981), DOI: 10.1063/1.92500 [[Crossref](#)].
- [65] P. F. Moulton, « *Ti-doped sapphire: tunable solid-state laser* », **Opt. News**, vol. 8, no. 6, p. 9, (1982), DOI: 10.1364/ON.8.6.000009 [[Crossref](#)].
- [66] P. F. Moulton, « *Spectroscopic and laser characteristics of Ti:Al<sub>2</sub>O<sub>3</sub>* »,
- [67] R. Ell *et al.*, « *Generation of 5-fs pulses and octave-spanning spectra directly from a ti:sapphire laser* », **Opt. Lett.**, vol. 26, no. 6, pp. 373–375, (2001), DOI: 10.1364/ol.26.000373 [[Crossref](#)].
- [68] K. A. Nelson and M. D. Fayer, « *Laser induced phonons: A probe of intermolecular interactions in molecular solids* », **J. Chem. Phys.**, vol. 72, no. 9, pp. 5202–5218, (1980), DOI: 10.1063/1.439756 [[Crossref](#)].
- [69] H. J. Eichler, P. Günter, and D. W. Pohl, « *Laser-Induced Dynamic Gratings* » (Optical Sciences). Springer, Berlin, Heidelberg, (1986), ISBN: 978-3-662-15197-6, DOI: 10.1007/978-3-540-39662-8 [[Crossref](#)].

- 
- [70] S. Volz *et al.*, « *Nanophononics: state of the art and perspectives* », **Eur. Phys. J. B**, vol. 89, 15, (2016), DOI: 10.1140/epjb/e2015-60727-7 [Crossref].
- [71] H. Ogi, N. Nakamura, and M. Hirao, « *Picosecond ultrasound spectroscopy for studying elastic modulus of thin films: a review* », **Nondestr. Test. Eval.**, vol. 26, no. 3-4, pp. 267–280, (2011), DOI: 10.1080/10589759.2011.569027 [Crossref].
- [72] P.-A. Mante *et al.*, « *Thz acoustic phonon spectroscopy and nanoscopy by using piezoelectric semiconductor heterostructures* », **Ultrasonics**, vol. 56, pp. 52–65, (2015), DOI: 10.1016/j.ultras.2014.09.020 [Crossref].
- [73] F. Violla and N. D. Fatti, « *Time-domain investigations of coherent phonons in van der waals thin films* », **Nanomaterials**, vol. 10, no. 12, p. 2543, (2020), DOI: 10.3390/nano10122543 [Crossref].
- [74] A. Amziane, L. Belliard, F. Decremps, and B. Perrin, « *Ultrafast acoustic resonance spectroscopy of gold nanostructures : Towards a generation of tunable transverse waves* », **Phys. Rev. B**, vol. 83, no. 1, 014102, (2011), DOI: 10.1103/PhysRevB.83.014102 [Crossref].
- [75] R. Fuentes-Domínguez, F. Pérez-cota, S. Naznin, R. J. Smith, and M. Clark, « *Super-resolution imaging using nano-bells* », **Sci. Rep.**, vol. 8, 16373, (2018), DOI: 10.1038/s41598-018-34744-6 [Crossref].
- [76] R. Fuentes-Domínguez *et al.*, « *Nano ultrasonic measurements of nanoparticles* », **AIP Conf. Proc.**, vol. 2102, no. 1, 020027, (2019), DOI: 10.1063/1.5099731 [Crossref].
- [77] R. Fuentes-Domínguez, S. Naznin, L. Marques, R. J. Smith, M. Clark, and F. Pérez-cota, « *Characterising the size and shape of metallic nano-structures by their acoustic vibrations* », **Nanoscale**, vol. 12, pp. 14 230–14 236, (2020), DOI: 10.1039/d0nr03410j [Crossref].
- [78] Y. Guillet, B. Audoin, M. Ferrié, and S. Ravaine, « *All-optical ultrafast spectroscopy of a single nanoparticle-substrate contact* », **Phys. Rev. B**, vol. 86, no. 3, p. 035 456, (2012), DOI: 10.1103/PhysRevB.86.035456 [Crossref].
- [79] R. Delalande, L. Burr, E. Charron, M. Jouini, M. E. Toimil-Molares, and L. Belliard, « *Vibrational response of au-ag alloy and porous au single nanowires probed by ultrafast pump-probe spectroscopy* », **Appl. Phys. Lett.**, vol. 115, no. 8, p. 083 103, (2019), DOI: 10.1063/1.5108772 [Crossref].
- [80] T. Devaux *et al.*, « *Giant extraordinary transmission of acoustic waves through a nanowire* », **Sci. Adv.**, vol. 6, no. 10, eaay8507, (2020), DOI: 10.1126/sciadv.aay8507 [Crossref].

- 
- [81] A. Huynh, B. Perrin, B. Jusserand, and A. Lemaître, « *Terahertz coherent acoustic experiments with semiconductor superlattices* », **Appl. Phys. Lett.**, vol. 99, no. 19, 191908, (2011), DOI: 10.1063/1.3658458 [[Crossref](#)].
- [82] A. A. Maznev *et al.*, « *Propagation of THz acoustic wave packets in GaN at room temperature* », **Appl. Phys. Lett.**, vol. 112, no. 6, 061903, (2018), DOI: 10.1063/1.5008852 [[Crossref](#)].
- [83] S. Ge *et al.*, « *Coherent longitudinal acoustic phonon approaching thz frequency in multilayer molybdenum disulphide* », **Sci. Rep.**, vol. 4, 5722, (2014), DOI: 10.1038/srep05722 [[Crossref](#)].
- [84] N. Lanzillotti-Kimura, A. Fainstein, and B. Jusserand, « *Towards ghz–thz cavity optomechanics in dbr-based semiconductor resonators* », **Ultrasonics**, vol. 56, pp. 80–89, (2015), DOI: 10.1016/j.ultras.2014.05.017 [[Crossref](#)].
- [85] J. V. Jäger *et al.*, « *Resonant driving of magnetization precession in a ferromagnetic layer by coherent monochromatic phonons* », **Phys. Rev. B**, vol. 92, no. 2, p. 020404, (2015), DOI: 10.1103/PhysRevB.92.020404 [[Crossref](#)].
- [86] A. V. Akimov, C. L. Poyser, and A. J. Kent, « *Review of microwave electrophonics in semiconductor nanostructures* », **Semicond. Sci. Technol.**, vol. 32, no. 5, p. 053003, (2017), DOI: 10.1088/1361-6641/aa52de [[Crossref](#)].
- [87] N. Chigarev, P. Zinin, L. C. Ming, G. Amulele, A. Bulou, and V. Gusev, « *Laser generation and detection of longitudinal and shear acoustic waves in a diamond anvil cell* », **Appl. Phys. Lett.**, vol. 93, no. 18, pp. 10–13, (2008), DOI: 10.1063/1.3013587 [[Crossref](#)].
- [88] N. Chigarev *et al.*, « *Analysis of ultrasonic echoes induced by pulsed laser action on an iron film in a diamond anvil cell* », **High Press. Res.**, vol. 30, no. 1, pp. 78–82, (2010), DOI: 10.1080/08957950903549519 [[Crossref](#)].
- [89] E. Edmund *et al.*, « *Picosecond acoustics technique to measure the sound velocities of Fe-Si alloys and Si single-crystals at high pressure* », **Minerals**, vol. 10, no. 3, 214, (2020), DOI: 10.3390/min10030214 [[Crossref](#)].
- [90] F. Decremps *et al.*, « *Picosecond acoustics method for measuring the thermodynamical properties of solids and liquids at high pressure and high temperature* », **Ultrasonics**, vol. 56, pp. 129–140, (2015), DOI: 10.1016/j.ultras.2014.04.011 [[Crossref](#)].
- [91] F. Pérez-Cota *et al.*, « *Picosecond ultrasonics for elasticity-based imaging and characterization of biological cells* », **J. Appl. Phys.**, vol. 128, no. 16, 160902, (2020), DOI: 10.1063/5.0023744 [[Crossref](#)].
- [92] T. Dehoux *et al.*, « *All-optical broadband ultrasonography of single cells* », **Sci. Rep.**, vol. 5, no. 1, p. 8650, (2015), DOI: 10.1038/srep08650 [[Crossref](#)].

- 
- [93] S. La Cavera, F. Pérez-Cota, R. J. Smith, and M. Clark, « *Phonon imaging in 3d with a fibre probe* », **Light: Science & Applications**, vol. 10, no. 1, p. 91, (2021), DOI: 10.1038/s41377-021-00532-7 [[Crossref](#)].
- [94] A. G. Every, « *Measurement of the near-surface elastic properties of solids and thin supported films* », **Meas. Sci. Technol.**, vol. 13, no. 5, R21–R39, (2002), DOI: 10.1088/0957-0233/13/5/201 [[Crossref](#)].
- [95] B. Saleh, Ed., « *Overview* » (Introduction to Subsurface Imaging). Cambridge University Press, (2012), pp. 1–20, DOI: 10.1017/cbo9780511732577.003 [[Crossref](#)].
- [96] M. Holt, R. Harder, R. Winarski, and V. Rose, « *Nanoscale hard x-ray microscopy methods for materials studies* », **Annu. Rev. Mater. Res.**, vol. 43, no. 1, pp. 183–211, (2013), DOI: 10.1146/annurev-matsci-071312-121654 [[Crossref](#)].
- [97] M Soliman, Y Ding, and L Tetard, « *Nanoscale subsurface imaging* », **J. Phys.: Condens. Matter**, vol. 29, no. 17, p. 173 001, (2017), DOI: 10.1088/1361-648x/aa5b4a [[Crossref](#)].
- [98] B. Bhushan, « *Springer Handbook of Nanotechnology* » (Springer Handbooks), 4th ed. Springer Berlin, Heidelberg, (2017), ISBN: 978-3-662-54355-9, DOI: 10.1007/978-3-662-54357-3 [[Crossref](#)].
- [99] O. Kolosov and K. Yamanaka, « *Nonlinear detection of ultrasonic vibrations in an atomic force microscope* », **Jpn. J. Appl. Phys.**, vol. 32, no. 8A, pp. L1095–L1098, (1993), DOI: 10.1143/JJAP.32.L1095 [[Crossref](#)].
- [100] R. E. Geer, O. V. Kolosov, G. A. D. Briggs, and G. S. Shekhawat, « *Nanometer-scale mechanical imaging of aluminum damascene interconnect structures in a low-dielectric-constant polymer* », **J. Appl. Phys.**, vol. 91, no. 7, pp. 4549–4555, (2002), DOI: 10.1063/1.1447330 [[Crossref](#)].
- [101] R. García and R. Pérez, « *Dynamic atomic force microscopy methods* », **Surf. Sci. Rep.**, vol. 47, no. 6, pp. 197–301, (2002), DOI: 10.1016/s0167-5729(02)00077-8 [[Crossref](#)].
- [102] N. F. Martinez, S. Patil, J. R. Lozano, and R. García, « *Enhanced compositional sensitivity in atomic force microscopy by the excitation of the first two flexural modes* », **Appl. Phys. Lett.**, vol. 89, no. 15, 153115, (2006), DOI: 10.1063/1.2360894 [[Crossref](#)].
- [103] L. Tetard, A. Passian, and T. Thundat, « *New modes for subsurface atomic force microscopy through nanomechanical coupling* », **Nature Nanotech.**, vol. 5, no. 2, pp. 105–109, (2010), DOI: 10.1038/nnano.2009.454 [[Crossref](#)].

- 
- [104] G. S. Shekhawat and V. P. Dravid, « *Nanoscale imaging of buried structures via scanning near-field ultrasound holography* », **Science**, vol. 310, no. 5745, pp. 89–92, (2005), DOI: 10.1126/science.1117694 [Crossref].
- [105] A. C. Diebold, « *Subsurface imaging with scanning ultrasound holography* », **Science**, vol. 310, no. 5745, pp. 61–62, (2005), DOI: 10.1126/science.1119259 [Crossref].
- [106] T. Taubner, F. eilmann, and R. Hillenbrand, « *Nanoscale-resolved subsurface imaging by scattering-type near-field optical microscopy* », **Opt. Express**, vol. 13, no. 22, pp. 8893–8899, (2005), DOI: 10.1364/OPEX.13.008893 [Crossref].
- [107] S. Perrin *et al.*, « *Microsphere-assisted phase-shifting profilometry* », **Appl. Opt.**, vol. 56, no. 25, pp. 7249–7255, (2017), DOI: 10.1364/AO.56.007249 [Crossref].
- [108] K. J. Koski and J. L. Yarger, « *Brillouin imaging* », **Appl. Phys. Lett.**, vol. 87, no. 6, p. 061 903, (2005), DOI: 10.1063/1.1999857 [Crossref].
- [109] G. Scarcelli *et al.*, « *Noncontact three-dimensional mapping of intracellular hydro-mechanical properties by brillouin microscopy* », **Nat. Methods**, vol. 12, no. 12, pp. 1132–1134, (2015), DOI: 10.1038/nmeth.3616 [Crossref].
- [110] G. Scarcelli and S. H. Yun, « *Confocal brillouin microscopy for three-dimensional mechanical imaging* », **Nat. Photonics**, vol. 2, no. 1, pp. 39–43, (2008), DOI: 10.1038/nphoton.2007.250 [Crossref].
- [111] F. Palombo and D. Fioretto, « *Brillouin Light Scattering: Applications in Biomedical Sciences* », **Chem. Rev.**, vol. 119, no. 13, pp. 7833–7847, (2019), DOI: 10.1021/acs.chemrev.9b00019 [Crossref].
- [112] R. Prevedel, A. Diz-Muñoz, G. Ruocco, and G. Antonacci, « *Brillouin microscopy: an emerging tool for mechanobiology* », **Nat. Methods**, vol. 16, no. 10, pp. 969–977, (2019), DOI: 10.1038/s41592-019-0543-3 [Crossref].
- [113] P. Wijesinghe, B. F. Kennedy, and D. D. Sampson, « *Optical elastography on the microscale* ». Elsevier, (2020), pp. 185–229, ISBN: 9780128096611, DOI: 10.1016/b978-0-12-809661-1.00009-1 [Crossref].
- [114] M. Bailey *et al.*, « *Viscoelastic properties of biopolymer hydrogels determined by Brillouin spectroscopy: A probe of tissue micromechanics* », **Sci. Adv.**, vol. 6, no. 44, eabc1937, (2020), DOI: 10.1126/sciadv.abc1937 [Crossref].
- [115] G. Antonacci *et al.*, « *Recent progress and current opinions in brillouin microscopy for life science applications* », **Biophys. Rev.**, vol. 12, no. 3, pp. 615–624, (2020), DOI: 10.1007/s12551-020-00701-9 [Crossref].

- 
- [116] J.-H. Lee, J. P. Singer, and E. L. Thomas, « *Micro-/nanostructured mechanical metamaterials* », **Adv. Mater.**, vol. 24, no. 36, pp. 4782–4810, (2012), DOI: 10.1002/adma.201201644 [Crossref].
- [117] F. Kargar and A. A. Balandin, « *Advances in brillouin–mandelstam light-scattering spectroscopy* », **Nat. Photonics**, vol. 15, no. 10, pp. 720–731, (2021), DOI: 10.1038/s41566-021-00836-5 [Crossref].
- [118] G. Antonacci, V. de Turrís, A. Rosa, and G. Ruocco, « *Background-deflection brillouin microscopy reveals altered biomechanics of intracellular stress granules by *als protein fus** », **Commun. Biol.**, vol. 1, no. 1, p. 139, (2018), DOI: 10.1038/s42003-018-0148-x [Crossref].
- [119] S. Speziale, H. Marquardt, and T. S. Duffy, « *Brillouin Scattering and its Application in Geosciences* », **Rev. Mineral. Geochem.**, vol. 78, no. 1, pp. 543–603, (2014), DOI: 10.1515/9781614517863.543 [Crossref].
- [120] S. M. Nikitin *et al.*, « *Revealing sub-mkm and mkm-scale textures in H<sub>2</sub>O ice at megabar pressures by time-domain Brillouin scattering* », **Sci. Rep.**, vol. 5, 9352, (2015), DOI: 10.1038/srep09352 [Crossref].
- [121] M. Kuriakose *et al.*, « *Picosecond laser ultrasonics for imaging of transparent polycrystalline materials compressed to megabar pressures* », **Ultrasonics**, vol. 69, pp. 259–267, (2016), DOI: 10.1016/j.ultras.2016.03.007 [Crossref].
- [122] M. Kuriakose *et al.*, « *Longitudinal sound velocities, elastic anisotropy, and phase transition of high-pressure cubic h<sub>2</sub>o ice to 82 gpa* », **Phys. Rev. B**, vol. 96, no. 13, p. 134122, (2017), DOI: 10.1103/PhysRevB.96.134122 [Crossref].
- [123] S. Raetz *et al.*, « *Elastic anisotropy and single-crystal moduli of solid argon up to 64 GPa from time-domain Brillouin scattering* », **Phys. Rev. B**, vol. 99, no. 22, 224102, (2019), DOI: 10.1103/PhysRevB.99.224102 [Crossref].
- [124] M. Kuriakose *et al.*, « *In situ imaging of the dynamics of photo-induced structural phase transition at high pressures by picosecond acoustic interferometry* », **New J. Phys.**, vol. 19, no. 5, p. 053026, (2017), DOI: 10.1088/1367-2630/aa6b3d [Crossref].
- [125] S. Sandeep *et al.*, « *3d characterization of individual grains of coexisting high-pressure h<sub>2</sub>o ice phases by time-domain brillouin scattering* », **J. Appl. Phys.**, vol. 130, no. 5, p. 053104, (2021), DOI: 10.1063/5.0056814 [Crossref].
- [126] M. Khafizov *et al.*, « *Subsurface imaging of grain microstructure using picosecond ultrasonics* », **Acta Mater.**, vol. 112, pp. 209–215, (2016), DOI: 10.1016/j.actamat.2016.04.003 [Crossref].

- 
- [127] Y. Wang *et al.*, « *Nondestructive characterization of polycrystalline 3d microstructure with time-domain brillouin scattering* », **Scr. Mater.**, vol. 166, pp. 34–38, (2019), DOI: 10.1016/j.scriptamat.2019.02.037 [Crossref].
- [128] Y. Wang *et al.*, « *Imaging grain microstructure in a model ceramic energy material with optically generated coherent acoustic phonons* », **Nat. Commun.**, vol. 11, no. 1, p. 1597, (2020), DOI: 10.1038/s41467-020-15360-3 [Crossref].
- [129] T. Thréard *et al.*, « *Photoacoustic 3-d imaging of polycrystalline microstructure improved with transverse acoustic waves* », **Photoacoustics**, vol. 23, p. 100286, (2021), DOI: 10.1016/j.pacs.2021.100286 [Crossref].
- [130] S. Danworaphong *et al.*, « *Three-dimensional imaging of biological cells with picosecond ultrasonics* », **Appl. Phys. Lett.**, vol. 106, no. 16, 163701, (2015), DOI: 10.1063/1.4918275 [Crossref].
- [131] F. Pérez-Cota, R. J. Smith, E. Moradi, L. Marques, K. F. Webb, and M. Clark, « *Thin-film optoacoustic transducers for subcellular Brillouin oscillation imaging of individual biological cells* », **Appl. Opt.**, vol. 54, no. 28, pp. 8388–8398, (2015), DOI: 10.1364/ao.54.008388 [Crossref].
- [132] F. Pérez-Cota, R. J. Smith, H. M. Elsheikha, and M. Clark, « *New insights into the mechanical properties of Acanthamoeba castellanii cysts as revealed by phonon microscopy* », **Biomed. Opt. Express**, vol. 10, no. 5, pp. 2399–2408, (2019), DOI: 10.1364/boe.10.002399 [Crossref].
- [133] R. Côte and A. Devos, « *Refractive index, sound velocity and thickness of thin transparent films from multiple angles picosecond ultrasonics* », **Rev. Sci. Instrum.**, vol. 76, no. 5, 053906, (2005), DOI: 10.1063/1.1900645 [Crossref].
- [134] A. Steigerwald *et al.*, « *Semiconductor point defect concentration profiles measured using coherent acoustic phonon waves* », **Appl. Phys. Lett.**, vol. 94, no. 11, 111910, (2009), DOI: 10.1063/1.3099341 [Crossref].
- [135] A. Steigerwald, A. B. Hmelo, K. Varga, L. C. Feldman, and N. Tolk, « *Determination of optical damage cross-sections and volumes surrounding ion bombardment tracks in GaAs using coherent acoustic phonon spectroscopy* », **J. Appl. Phys.**, vol. 112, no. 1, 013514, (2012), DOI: 10.1063/1.4732072 [Crossref].
- [136] J. Chandezon, J.-M. Rampnoux, S. Dilhaire, B. Audoin, and Y. Guillet, « *In-line femtosecond common-path interferometer in reflection mode* », **Opt. Express**, vol. 23, no. 21, pp. 27011–27019, (2015), DOI: 10.1364/OE.23.027011 [Crossref].
- [137] B. P. Abbott *et al.*, « *Observation of Gravitational Waves from a Binary Black Hole Merger* », **Phys. Rev. Lett.**, vol. 116, no. 6, 061102, (2016), DOI: 10.1103/PhysRevLett.116.061102 [Crossref].

- 
- [138] A. A. Michelson and E. W. Morley, « *On the relative motion of the Earth and the luminiferous ether* », **Am. J. Sci.**, vol. 34, no. 203, pp. 333–345, (1887), DOI: 10.2475/ajs.s3-34.203.333 [Crossref].
- [139] E. Tokunaga, T. Kobayashi, and A. Terasaki, « *Frequency-domain interferometer for femtosecond time-resolved phase spectroscopy* », **Opt. Lett.**, vol. 17, no. 16, pp. 1131–1133, (1992), DOI: 10.1364/ol.17.001131 [Crossref].
- [140] J. P. Geindre *et al.*, « *Frequency-domain interferometer for measuring the phase and amplitude of a femtosecond pulse probing a laser-produced plasma* », **Opt. Lett.**, vol. 19, no. 23, pp. 1997–1999, (1994), DOI: 10.1364/OL.19.001997 [Crossref].
- [141] C.-H. Cheng, « *Asymmetrical interleaver structure based on the modified Michelson interferometer* », **Opt. Eng.**, vol. 44, no. 11, 115003, (2005), DOI: 10.1117/1.2126586 [Crossref].
- [142] Y.-c. Shen and P. Hess, « *Real-time detection of laser-induced transient gratings and surface acoustic wave pulses with a michelson interferometer* », **J. Appl. Phys.**, vol. 82, no. 10, pp. 4758–4762, (1997), DOI: 10.1063/1.366332 [Crossref].
- [143] C. Rossignol, J. M. Rampnoux, M. Perton, B. Audoin, and S. Dilhaire, « *Generation and detection of shear acoustic waves in metal submicrometric films with ultrashort laser pulses* », **Phys. Rev. Lett.**, vol. 94, no. 16, p. 166 106, (2005), DOI: 10.1103/PhysRevLett.94.166106 [Crossref].
- [144] C. J. Fiedler and J. W. Wagner, « *Interferometric detection of high frequency pulses of ultrasound in thin coatings* », in D. O. Thompson and D. E. Chimenti, Eds. Boston, MA: Springer US, 1997, pp. 1579–1584, DOI: 10.1007/978-1-4615-5947-4\_206 [Crossref].
- [145] C. J. K. Richardson, M. J. Ehrlich, and J. W. Wagner, « *Interferometric detection of ultrafast thermoelastic transients in thin films: theory with supporting experiment* », **J. Opt. Soc. Am. B**, vol. 16, no. 6, pp. 1007–1015, (1999), DOI: 10.1364/JOSAB.16.001007 [Crossref].
- [146] D. Grassani, M. Galliani, and D. Bajoni, « *Active stabilization of a Michelson interferometer at an arbitrary phase with subnanometer resolution* », **Opt. Lett.**, vol. 39, no. 8, pp. 2530–2533, (2014), DOI: 10.1364/OL.39.002530 [Crossref].
- [147] C. Fabry and A. Perot, « *On a new form of interferometer* », **Astrophys. J.**, vol. 13, pp. 265–273, (1901), DOI: 10.1086/140817 [Crossref].
- [148] J. P. Waclawek, C. Kristament, H. Moser, and B. Lendl, « *Balanced-detection interferometric cavity-assisted photothermal spectroscopy* », **Opt. Express**, vol. 27, no. 9, pp. 12 183–12 195, (2019), DOI: 10.1364/oe.27.012183 [Crossref].

- 
- [149] D. Pinto *et al.*, « *Parts-per-billion detection of carbon monoxide: A comparison between quartz-enhanced photoacoustic and photothermal spectroscopy* », **Photoacoustics**, vol. 22, 100244, (2021), DOI: 10.1016/j.pacs.2021.100244 [[Crossref](#)].
- [150] R. Y. Chiao, C. H. Townes, and B. P. Stoicheff, « *Stimulated Brillouin Scattering and Coherent Generation of Intense Hypersonic Waves* », **Phys. Rev. Lett.**, vol. 12, no. 21, pp. 592–595, (1964), DOI: 10.1103/physrevlett.12.592 [[Crossref](#)].
- [151] R. Mock, B. Hillebrands, and R. Sandercock, « *Construction and performance of a Brillouin scattering set-up using a triple-pass tandem Fabry-Perot interferometer* », **J. Phys. E.**, vol. 20, no. 6, pp. 656–659, (1987), DOI: 10.1088/0022-3735/20/6/017 [[Crossref](#)].
- [152] A. Maznev, K. A. Nelson, and T. Yagi, « *Surface phonon spectroscopy with frequency-domain impulsive stimulated light scattering* », **Solid State Commun.**, vol. 100, no. 12, pp. 807–811, (1996), DOI: 10.1016/S0038-1098(96)00540-6 [[Crossref](#)].
- [153] A. Nadeau, F. Martin, A. Blouin, F. Nadeau, M. Choquet, and M. Lord, « *Application of laser-ultrasonics to the non-contact, pulse echo measurement of the thickness of micron thin metallic coatings* », **AIP Conf. Proc.**, vol. 894, no. 1, pp. 225–232, (2007), DOI: 10.1063/1.2717977 [[Crossref](#)].
- [154] F. Yang, T. J. Grimsley, and H. J. Maris, « *Enhancement of picosecond ultrasonic signals through the use of an optical cavity* », **J. Phys.: Conf. Ser.**, vol. 92, p. 012023, (2007), DOI: 10.1088/1742-6596/92/1/012023 [[Crossref](#)].
- [155] Y. Li, Q. Miao, A. V. Nurmikko, and H. J. Maris, « *Picosecond ultrasonic measurements using an optical cavity* », **J. Appl. Phys.**, vol. 105, no. 8, p. 083516, (2009), DOI: 10.1063/1.3095470 [[Crossref](#)].
- [156] K. Ishikawa *et al.*, « *Interferometric imaging of acoustical phenomena using high-speed polarization camera and 4-step parallel phase-shifting technique* », **Selected Papers from the 31st International Congress on High-Speed Imaging and Photonics**, vol. 10328, pp. 93–99, (2017), DOI: 10.1117/12.2269940 [[Crossref](#)].
- [157] N. S. Patel, K. L. Hall, and K. A. Rauschenbach, « *Interferometric all-optical switches for ultrafast signal processing* », **Appl. Opt.**, vol. 37, no. 14, pp. 2831–2842, (1998), DOI: 10.1364/AO.37.002831 [[Crossref](#)].
- [158] M. A. van Dijk, M. Lippitz, and M. Orrit, « *Detection of acoustic oscillations of single gold nanospheres by time-resolved interferometry* », **Phys. Rev. Lett.**, vol. 95, no. 26, p. 267406, (2005), DOI: 10.1103/PhysRevLett.95.267406 [[Crossref](#)].

- 
- [159] M. A. van Dijk, M. Lippitz, D. Stolwijk, and M. Orrit, « *A common-path interferometer for time-resolved and shot-noise-limited detection of single nanoparticles* », **Opt. Express**, vol. 15, no. 5, pp. 2273–2287, (2007), DOI: 10.1364/OE.15.002273 [Crossref].
- [160] L. Liu, Y. Guillet, and B. Audoin, « *Common-path conoscopic interferometry for enhanced picosecond ultrasound detection* », **J. Appl. Phys.**, vol. 123, no. 17, p. 173 103, (2018), DOI: 10.1063/1.5016279 [Crossref].
- [161] X. Jia, A. Boumiz, and G. Quentin, « *Laser interferometric detection of ultrasonic waves propagating inside a transparent solid* », **Appl. Phys. Lett.**, vol. 63, no. 16, pp. 2192–2194, (1993), DOI: 10.1063/1.110550 [Crossref].
- [162] R. H. J. Kop and R. Sprik, « *Phase-sensitive interferometry with ultrashort optical pulses* », **Rev. Sci. Instrum.**, vol. 66, no. 12, pp. 5459–5463, (1995), DOI: 10.1063/1.1146069 [Crossref].
- [163] C. Rossignol and B. Perrin, « *Interferometric detection in picosecond ultrasonics for nondestructive testing of submicrometric opaque multilayered samples: tin/alcu/tin/ti/si* », **IEEE Trans. Ultrason. Ferroelectr. Freq. Control.**, vol. 52, no. 8, pp. 1354–1359, (2005), DOI: 10.1109/TUFFC.2005.1509794 [Crossref].
- [164] C. Rossignol, B. Perrin, and S. Laborde, « *Nondestructive evaluation of micrometric diamond films with an interferometric picosecond ultrasonics technique* », **J. Appl. Phys.**, vol. 95, no. 8, pp. 4157–4162, (2004), DOI: 10.1063/1.1687049 [Crossref].
- [165] M. C. Gabriel, N. A. Whitaker, C. W. Dirk, M. G. Kuzyk, and M. Thakur, « *Measurement of ultrafast optical nonlinearities using a modified sagnac interferometer* », **Opt. Lett.**, vol. 16, no. 17, pp. 1334–1336, (1991), DOI: 10.1364/OL.16.001334 [Crossref].
- [166] M. Nikoonahad, S. Lee, and H. Wang, « *Picosecond photoacoustics using common-path interferometry* », **Appl. Phys. Lett.**, vol. 76, no. 4, pp. 514–516, (2000), DOI: 10.1063/1.125805 [Crossref].
- [167] D. H. Hurley, O. B. Wright, O. Matsuda, V. E. Gusev, and O. V. Kolosov, « *Laser picosecond acoustics in isotropic and anisotropic materials* », **Ultrasonics**, vol. 38, no. 1, pp. 470–474, (2000), DOI: 10.1016/S0041-624X(99)00035-9 [Crossref].
- [168] Y. Sugawara *et al.*, « *Watching ripples on crystals* », **Phys. Rev. Lett.**, vol. 88, no. 18, p. 185 504, (2002), DOI: 10.1103/PhysRevLett.88.185504 [Crossref].
- [169] Y. Sugawara, O. B. Wright, and O. Matsuda, « *Real-time imaging of surface acoustic waves in thin films and microstructures on opaque substrates (invited)* », **Rev. Sci. Instrum.**, vol. 74, no. 1, pp. 519–522, (2003), DOI: 10.1063/1.1520323 [Crossref].

- 
- [170] T. Tachizaki, T. Muroya, O. Matsuda, Y. Sugawara, D. H. Hurley, and O. B. Wright, « *Scanning ultrafast Sagnac interferometry for imaging two-dimensional surface wave propagation* », **Rev. Sci. Instrum.**, vol. 77, no. 4, 043713, (2006), DOI: 10.1063/1.2194518 [[Crossref](#)].
- [171] P. A. Fomichov, A. K. Kromine, S. Krisbuaswamy, and J. D. Achenbach, « *Sagnac-type fiber-optic array sensor for detection of bulk ultrasonic waves* », **IEEE Trans. Ultrason. Ferroelectr. Freq. Control**, vol. 47, no. 3, pp. 584–590, (2000), DOI: 10.1109/58.842045 [[Crossref](#)].
- [172] T. S. Jang, S. S. Lee, I. B. Kwon, W. J. Lee, and J. J. Lee, « *Noncontact detection of ultrasonic waves using fiber optic sagnac interferometer* », **IEEE Trans. Ultrason. Ferroelectr. Freq. Control**, vol. 49, no. 6, pp. 767–775, (2002), DOI: 10.1109/TUFFC.2002.1009334 [[Crossref](#)].
- [173] G. Wild and S. Hinckley, « *Acousto-ultrasonic optical fiber sensors: Overview and state-of-the-art* », **IEEE Sens. J.**, vol. 8, no. 7, pp. 1184–1193, (2008), DOI: 10.1109/JSEN.2008.926894 [[Crossref](#)].
- [174] K. Iniewski, Ed., « *Smart Sensors for Industrial Applications* ». CRC Press, (2013), ISBN: 978-1-4665-6811-2, DOI: 10.1201/b14875 [[Crossref](#)].
- [175] K. Y. Hashimoto *et al.*, « *A fast scanning laser probe based on Sagnac interferometer for RF surface and bulk acoustic wave devices* », in **IEEE MTT-S International Microwave Symposium Digest**, (2008), pp. 851–854, DOI: 10.1109/MWSYM.2008.4632966 [[Crossref](#)].
- [176] K. Y. Hashimoto *et al.*, « *A laser probe based on a Sagnac interferometer with fast mechanical scan for RF surface and bulk acoustic wave devices* », **IEEE Trans. Ultrason. Ferroelectr. Freq. Control**, vol. 58, no. 1, pp. 187–193, (2011), DOI: 10.1109/TUFFC.2011.1785 [[Crossref](#)].
- [177] E. Péronne and B. Perrin, « *Generation and detection of acoustic solitons in crystalline slabs by laser ultrasonics* », **Ultrasonics**, vol. 44, pp. 1203–1207, (2006), DOI: 10.1016/j.ultras.2006.05.072 [[Crossref](#)].
- [178] J.-Y. Duquesne and B. Perrin, « *Ultrasonic attenuation in a quasicrystal studied by picosecond acoustics as a function of temperature and frequency* », **Phys. Rev. B**, vol. 68, no. 13, p. 134 205, (2003), DOI: 10.1103/PhysRevB.68.134205 [[Crossref](#)].
- [179] C. Klieber *et al.*, « *Narrow-band acoustic attenuation measurements in vitreous silica at frequencies between 20 and 400 ghz* », **Appl. Phys. Lett.**, vol. 98, no. 21, p. 211 908, (2011), DOI: 10.1063/1.3595275 [[Crossref](#)].

- 
- [180] M. F. Pascual-Winter, A. Fainstein, B. Jusserand, B. Perrin, and A. Lemaître, « *Spectral responses of phonon optical generation and detection in superlattices* », **Phys. Rev. B**, vol. 85, no. 23, p. 235 443, (2012), DOI: 10.1103/PhysRevB.85.235443 [Crossref].
- [181] A. Devos, S. Sadtler, P.-A. Mante, A. Le Louarn, and P. Emery, « *Pushing the limits of acoustics at the nanoscale using femtosecond transient interferometry* », **Appl. Phys. Lett.**, vol. 105, no. 23, p. 231 905, (2014), DOI: 10.1063/1.4903875 [Crossref].
- [182] A. Y. Klokov, V. S. Krivobok, A. I. Sharkov, V. A. Tsvetkov, V. P. Martovitskii, and A. V. Novikov, « *Acoustic properties of strained *sig/si* layers in the sub-terahertz frequency range* », **J. Appl. Phys.**, vol. 127, no. 15, p. 154 304, (2020), DOI: 10.1063/1.5129847 [Crossref].
- [183] N. L. Abdala *et al.*, « *Mesoporous Thin Films for Acoustic Devices in the Gigahertz Range* », **J. Phys. Chem. C**, vol. 12431, pp. 17 165–17 171, (2020), DOI: 10.1021/acs.jpcc.0c05464 [Crossref].
- [184] O. Matsuda and O. B. Wright, « *Laser picosecond acoustics with oblique probe light incidence* », **Rev. Sci. Instrum.**, vol. 74, no. 1, pp. 895–897, (2003), DOI: 10.1063/1.1519679 [Crossref].
- [185] O. Matsuda, T. Tachizaki, T. Fukui, J. J. Baumberg, and O. B. Wright, « *Acoustic phonon generation and detection in *gaas/al<sub>0.3</sub>ga<sub>0.7</sub>as* quantum wells with picosecond laser pulses* », **Phys. Rev. B**, vol. 71, no. 11, p. 115 330, (2005), DOI: 10.1103/PhysRevB.71.115330 [Crossref].
- [186] O. Matsuda *et al.*, « *Ultrafast ellipsometric interferometry for direct detection of coherent phonon strain pulse profiles* », **J. Opt. Soc. Am. B**, vol. 30, no. 7, pp. 1911–1920, (2013), DOI: 10.1364/JOSAB.30.001911 [Crossref].
- [187] D. F. J. Arago and A. J. Fresnel, « *On the action of rays of polarized light upon each other* », **Ann. Chim. Phys.**, vol. 2, pp. 288–305, (1819), library Galicia (Fr.), [Online]. **Available at:** <https://gallica.bnf.fr/ark:/12148/bpt6k6570892b>.
- [188] R. Barakat, « *Analytic proofs of the Arago-Fresnel laws for the interference of polarized light* », **J. Opt. Soc. Am. A**, vol. 10, no. 1, pp. 180–185, (1993), DOI: 10.1364/JOSAA.10.000180 [Crossref].
- [189] R. Hanau, « *Interference of Linearly Polarized Light with Perpendicular Polarizations* », **Am. J. Phys.**, vol. 31, no. 4, pp. 303–304, (1963), DOI: 10.1119/1.1969459 [Crossref].
- [190] P. de Groot, « *Fiber-coupled Laser Diode Mount for Interferometry* », **Appl. Opt.**, vol. 32, no. 34, pp. 7122–7123, (1993), DOI: 10.1364/AO.32.007122 [Crossref].

- 
- [191] G. E. Jellison, « *Optical functions of GaAs, GaP, and Ge determined by two-channel polarization modulation ellipsometry* », **Opt. Mater.**, vol. 1, no. 3, pp. 151–160, (1992), DOI: 10.1016/0925-3467(92)90022-F [Crossref].
- [192] O. Madelung, U. Rössler, and M. Schulz, Eds., « *Semiconductors. Group IV Elements, IV-IV and III-V Compounds. Part a - Lattice Properties* ». Springer-Verlag Berlin Heidelberg, (2001), DOI: 10.1007/b60136 [Crossref].
- [193] T. Dehoux and B. Audoin, « *Non-invasive optoacoustic probing of the density and stiffness of single biological cells* », **J. Appl. Phys.**, vol. 112, no. 12, p. 124 702, (2012), DOI: 10.1063/1.4769294 [Crossref].
- [194] F. Van Breugel, J. N. Kutz, and B. W. Brunton, « *Numerical differentiation of noisy data: a unifying multi-objective optimization framework* », **IEEE Access**, vol. 8, pp. 196 865–196 877, (2020), DOI: 10.1109/ACCESS.2020.3034077 [Crossref].
- [195] A. G. Every and A. K. McCurdy, « Table 7. cubic system. binary compounds », in *Landolt-Börnstein - Group III Condensed Matter 29A (Second and Higher Order Elastic Constants)*, D. F. Nelson, Ed., DOI: 10.1007/10046537\_14 [Crossref], Springer Materials, 1992.
- [196] K. Papatryfonos *et al.*, « *Refractive indices of mbe-grown  $al_{x}ga_{1-x}as$  ternary alloys in the transparent wavelength region* », **AIP Advances**, vol. 11, no. 2, p. 025 327, (2021), DOI: 10.1063/5.0039631 [Crossref].
- [197] A. D. Rakić and M. L. Majewski, « *Modeling the optical dielectric function of gaas and alas: extension of adachi’s model* », **J. Appl. Phys.**, vol. 80, no. 10, pp. 5909–5914, (1996), DOI: 10.1063/1.363586 [Crossref].
- [198] M. Damzen, V. I. Vlad, V. Babin, and A. Mocofanescu, « *Stimulated Brillouin Scattering: Fundamentals and Applications* » (Optics and Optoelectronics), 1st ed. IOP Publishing, Bristol, (2003), ISBN: 9780429145513, DOI: 10.1201/9781420033465 [Crossref].
- [199] J. F. Reintjes, « *Nonlinear Optical Processes* » (Encyclopedia of Physical Science and Technology), 3rd ed. Academic Press, (2003), pp. 537–581, ISBN: 9780122274107, DOI: 10.1016/b0-12-227410-5/00485-3 [Crossref].
- [200] E. Hecht, « *Optics* » (Pearson education). Addison-Wesley, (2002), ISBN: 9780321188786. [Online]. **Available at:** <https://books.google.fr/books?id=T3ofAQAAMAAJ>.
- [201] B. Petrak and M. Peiris. « *Coupling a LASER into a single mode fiber* ». University of South Florida - Solid State Quantum Optics Laboratory, Youtube. ((**Jul. 24, 2012**)), [Online]. **Available at:** <https://youtu.be/kQvhbJbDGOM> (visited on 12/11/2018).



**Titre :** Application de l'interférométrie optique ultrarapide au profilage opto-acousto-optique en profondeur des matériaux

**Mot clés :** Ultrasons laser, acoustique picoseconde, diffusion Brillouin dans le domaine temporel, interférométrie ultrarapide, imagerie et caractérisation non destructive nanométrique.

**Résumé :** L'imagerie et la caractérisation des inhomogénéités spatiales des matériaux à l'échelle micro ou nanométrique sont d'une extrême importance pour comprendre les limites de leurs fonctionnalités. Dans la diffusion Brillouin dans le domaine temporel (TDBS), la réflectivité optique transitoire de l'échantillon enregistrée par un faisceau sonde alors qu'une nano-impulsion acoustique se propage dans l'espace contient des informations sur les paramètres acoustiques, optiques et acousto-optiques locaux du matériau sondé. Cette thèse a été consacrée à la conception, la construction et au test d'un nouvel instrument TDBS pour le profilage en profondeur de milieux transparents avec une résolution axiale potentiellement contrôlée par la longueur de quelques nanomètres de l'impulsion acoustique, indépendamment de la longueur d'onde

de la lumière sonde. L'instrument comprend un interféromètre de Sagnac ultrarapide à fibre facilement ajustable en angle, qui permet de mesurer la phase de la réflectivité optique transitoire, contenant les informations sur l'indice de réfraction local et la vitesse du son, à des angles d'incidence multiples de la lumière sonde, avec un contrôle précis et continu. La première application de l'interférométrie ultrarapide à l'imagerie TDBS a été la démonstration d'une variation linéaire de la phase de la réflectivité transitoire en fonction de la profondeur dans un échantillon homogène, ouvrant la voie à des applications pour des matériaux inhomogènes. Cet interféromètre accroît la fonctionnalité et l'utilité de la technique TDBS pour l'imagerie dans tous les domaines scientifiques, notamment la physique, la chimie, la biologie et la médecine.

**Title:** Application of ultrafast optical interferometry for opto-acousto-optical depth-profiling of materials

**Keywords:** Laser ultrasonics, picosecond acoustics, time-domain Brillouin scattering, ultrafast interferometry, nanoscale imaging and non-destructive characterization.

**Abstract:** Imaging and characterization of material spatial inhomogeneities at the micro- to nanoscale is of extreme importance for understanding the limits in their functionalities. In time-domain Brillouin scattering (TDBS), the transient optical reflectivity of the sample recorded by a probe beam as an acoustic nanopulse propagates in space holds information on the local acoustical, optical, and acousto-optical parameters of the probed material. This PhD thesis was devoted to the design, construction and testing of a new TDBS instrument for the depth profiling of transparent media with an axial resolution potentially controlled by the few-nanometers length of the acoustic pulse, independent of probe light

wavelength. The instrument includes an easily angle-adjustable fiber ultrafast Sagnac interferometer, which provides opportunity for measuring the phase of the transient optical reflectivity, containing the information on the local refractive index and sound velocity, at multiple incidence angles of probe light, with precise and continuous control. The first application of the ultrafast interferometry in TDBS imaging was the demonstration of a linear variation of the transient reflectivity phase on depth in a homogeneous sample, opening for inhomogeneous material applications. This interferometer increases the functionality and utility of TDBS for imaging in all areas of science, including physics, chemistry, biology and medicine.